Measured and Modeled Time and Angle Dispersion Characteristics of the 1.8 GHz Peer-to-Peer Radio Channel

Neal Patwari

Thesis submitted to the Faculty of the
Virginia Polytechnic Institute and State University
in partial fulfillment of the requirements for the degree of

Master of Science
in
Electrical Engineering

Theodore S. Rappaport, Chair
Gary S. Brown
Ahmad Safaai-Jazi

April 29, 1999
Blacksburg, Virginia

Keywords: Radio Wave Propagation Channel, Measurement,
Modeling, 2 GHz, Peer-to-Peer, Low Antenna

Measured and Modeled Time and Angle Dispersion Characteristics of the 1.8 GHz Peer-to-Peer Radio Channel

Neal Patwari

(ABSTRACT)

In an extensive outdoor propagation study, low antenna heights of 1.7 m are used at both the transmitter and the receiver to measure over 3500 wideband power-delay profiles (PDPs) of the channel for a peer-to-peer communications system. Rural and urban areas are studied in 22 different transmitter-receiver links. The results are used to characterize the narrowband path loss, mean delay, root-mean-square (RMS) delay spread, and timing jitter of the peer-to-peer wideband channel. Small-scale fading characteristics are measured in detail by measuring and analyzing 160 PDPs within each local area. This thesis shows the measurement setup for the calculation of fading rate variance and angular spread and reports the first known attempt to calculate angular spread from track power measurements. New analysis presented in this thesis shows the effect of measurement error in the calculation of angular spread. The expected characteristics of angular spread are derived using two different angle-of-arrival (AOA) models from the literature. Measurement results show initial validation of Durgin's angular spread theory. A new measurement-based algorithm for simulating wideband fading processes is developed and implemented. This simulation technique shows promise in the simulation of high-bit rate peer-to-peer radio communication systems.

Acknowledgments

I owe a great debt of gratitude and thanks to Michael D'Aria, Raymond Lovestead, Christopher Wajciechowski, and Christopher Westcott for their efforts in the measurement campaign. Without their help, measurement data could not have been taken. I also thank Gregory D. Durgin and Hao Xu for their helpful advice and guidance throughout the measurement campaign. I would also like to credit Dr. Robert J. Boyle and my advisor, Dr. Theodore S. Rappaport, for their management of the ITT project, their advice and review of this work.

I give thanks for the love and support of my family, my brother Parth and my mom and dad, Arti and Ken Patwari.

This material is based upon work supported under a National Science Foundation Graduate Research Fellowship. I am truly grateful for their support. They require a disclaimer that says that any opinions, findings, conclusions or recommendations expressed in this publication are those of the author and do not necessarily reflect the views of the National Science Foundation.

Contents

List of Figures

List of Tables

Chapter 1

Introduction

The measurement campaign reported in this thesis was started due to the joint interests of ITT and Virginia Tech. ITT is involved in the design and development of the Handheld Mobile Terminal (HMT), a new tactical mobile transceiver being developed for the U.S. Army. It is part of their plan to equip field personnel with mobile "walkie-talkies" capable of providing them with high-bit rate data services. These services will include voice, video, battlefield maps, and locations of other troops and equipment. The HMT will be in the hands of its user, and thus it will operate with a typical height of 1.7 m. The term *peer-to-peer* means that terminals communicate directly with one another. Thus the radio wave propagation occurs from a low antenna to another low antenna. In between these low antennas, it is expected that low-lying scatterers in the environment, such as brush, tree leaves and branches, people, automobiles, and buildings, all result in a multipath channel that is severely time and angle dispersive. That is, multipath components of the received signal will arrive at the receiver with various time delays and from various angles.

Both time and angle dispersion are impediments to receiver design. However, the combination of low antenna heights and wide 10 MHz RF bandwidth of the HMT, has not been characterized fully by the research community. Measurements in this channel are essential for several reasons:

- Wideband measurements are necessary to determine the channel's time dispersion.
- Fading measurements are needed to simulate the performance of adaptive equalizers that can be used if the time dispersion is too strong.
- The angular dispersion of the channel is necessary to determine the effectiveness of spatial diversity techniques.

- The fading statistics will determine the effectiveness of error correction coding used on a link.

For all of these reasons, this study of the low antenna to low antenna channel is of interest to ITT in support of their HMT project. They are interested in very wide bandwidth channel propagation characteristics at a carrier of 1.8 GHz. Accurate channel characterization requires propagation measurements in a variety of possible battlefield environments, urban and rural. As the measurement results will show, the HMT requires the use of an equalizer since its wide bandwidth of operation exceeds the coherence bandwidth of the channel. Thus there is a need for a measurement-based channel model to simulate the performance of an adaptive equalizer. This thesis presents the measurement results and a measurement-based channel model for radio simulation.

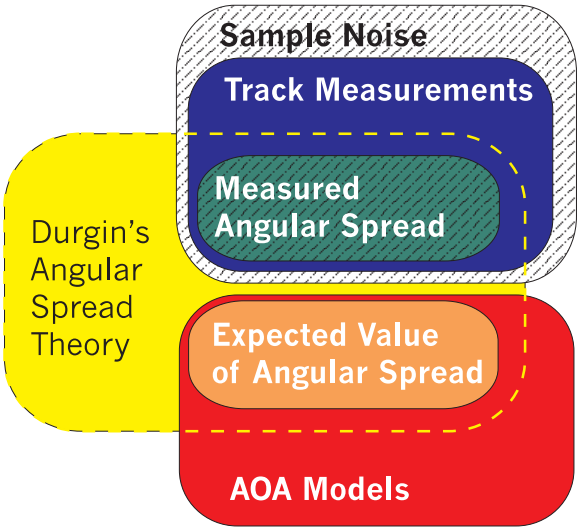

Figure 1.1: Track measurements are corrupted by noise and error leading to angular spread errors. The angular spread theory can be applied to AOA models to predict the expected behavior of the angular spread. The measured and theoretical angular spreads can then be compared.

An equally important purpose of the measurements is to validate new theory relating the fading rate variance and the angular spread of arriving power in a local area [5, 6]. The calculation of angular spread using track power measurements has never previously been reported in the literature. This thesis must attempt to verify the assumptions of the angular spread theory. In addition it must report the methods of the measurement of angular spread and the analytical tools needed to evaluate the results. The analytical tools are based on reported angle-of-arrival models and will help validate the results in the absence of previous measurements to use as a comparison. Fig. (1.1) shows the parallel process used to compare measurements with theory.

1.1 Previous Research

Although the 1.8 GHz carrier frequency has been the center of a variety of research for PCS carriers, the emphasis has been on cellular and microcellular applications. Although microcellular research advertises its antennas as 'low', these antennas are at minimum 3.2 m from the ground [7], and more typically in the 5 - 20 m range [4, 8, 9, 10, 11, 12]. Since researchers have found that microcellular propagation characteristics depend heavily on antenna height and local environment [13], it would be misleading to extrapolate microcellular measurements to the peer-to-peer case. In addition, these PCS-focused measurements are intended for a narrower bandwidth, 1.25 MHz for CDMA systems, compared to the HMT's 10 MHz bandwidth. Many did not measure wideband characteristics [7, 8, 9, 10].

Recent wideband measurements have simultaneously determined the time-delay-of-arrival (TDOA) and the angle-of-arrival (AOA) of multipath components at a receiver [14, 15, 2]. These researchers measured complex channel impulse responses at several positions in a grid or an array and used synthetic-aperture antenna techniques, ESPRIT, or Fourier analysis to solve for the angles-of-arrival of the multipath components. Angular spread could be calculated from these results. However none of these measurements studied the peer-to-peer channel – environments were specifically chosen with low clutter and high antennas [15].

1.1.1 Measurement System Comparison

In comparison with these previously reported measurements, the measurement system used in this thesis measures wideband PDPs, similar to those used previously at MPRG [16, 4]. However, it does not measure complex channel impulse responses like the systems of [14, 15, 2]. Since the MPRG sliding correlator measurement system does not measure the phase of the incoming signal, it can only be used to measure signal envelope or power. The advantage with this measurement system is low complexity – the transmitter and receiver require half as many PN signal generators and correlators. And as shown by Durgin in [5, 6], angular characteristics can still be determined. Like the measurements in [14, 15, 2], this determination requires wideband measurements at several points in a local area.

1.2 Outcomes

Over 3500 measured PDPs were captured and processed to present the results reported here. These measured power delay profiles are taken from rural and urban areas on the Virginia Tech campus. Twenty-two receiver locations and 8 different transmitter locations allowed the measurement of various channel characteristics. The measurements tested a wide range of path lengths, from 40 m to 1300 m. This wide variety of wideband measurement data has been directly used by designers of the HMT in their simulations.

This measurement data has helped develop new wideband channel simulation methods. Using the more accurate simulation models presented in this report, the measurement data can be used to simulate the complex channel impulse response for a terminal in motion. The measurement-based channel model presented in this report is very useful in the design of rake receivers and adaptive equalizers for wideband peer-to-peer radios.

The measured data can also be used to evaluate and improve ray-tracing propagation prediction results. Ray tracing can provide deterministic propagation prediction for actual locations without measurements [17] [18]. The angular spread information calculated here will provide a new parameter for comparison between measurements and predictions. Validation of the angular characteristics of ray-tracing predictions will be necessary if ray-tracing is to be used in simulations of systems employing smart antennas, position location technologies, or spatial division multiple access (SDMA) schemes.

From the funding generated by these measurements, a new automated linear and rotary positioning system has been purchased to allow new positioning accuracy and speed in channel measurements. It allows simultaneous spatial and temporal channel measurements by precise computer-controlled positioning that minimizes the effect of channel transients and human-induced positioning error. It also allows the operator to remove himself from the channel during measurements so that his presence can not inadvertently affect the channel. In the future, this system will be used in AOA measurements that will directly verify the new analytical relationships between angle-of-arrival and fading rate.

The techniques developed in this thesis combined with the automated positioning system will allow large scale AOA measurements. Such information will have a significant impact in the effective design and evaluation of position location technologies, smart antennas, and SDMA systems.

1.3 Overview of Measurement Plan

For this thesis, we define a *measurement site* as an area on campus where we will fix a common transmitter location for measurement of orthogonal tracks of 160 PDPs at each of 2-4 different receiver locations. Each different local area in which the receiver is placed is a different distance from the transmitter at a measurement site and is referred to in this plan as a *receiver location*. Each receiver location is identified by a unique number, and the PDPs captured there are all within a local area, not larger than a 20λ by 20λ square. Receiver locations are chosen in areas with different street widths, terrain, land usage, and scatterer density in order to represent a wide range of propagation environments. They are also chosen to represent a wide range of separation distances over several orders of magnitude to help characterize large-scale path loss characteristics. Eight sites are measured (that is, there are 8 different transmitter locations), and there are a grand total of 22 receiver locations. We refer to these receiver locations unambiguously by a number from 1 to 22. Table 1.1 shows what the eight sites are and which receiver locations were measured at each site. The transmitter-receiver separation distances, link details, and measurement results are given for each receiver location in Table 6.1.

Table 1.1: Table of Measurement Sites and their Receiver Locations

Environment	Site Name	Receiver Location Numbers
Urban	Old Turner St.	1, 2, 3, 4
Rural	Southgate Dr.	5, 6, 7
Rural	Beef Cattle Farm	8, 9, 10
Rural	Forest	11, 12
Urban	Hutcheson Hall	13, 14, 15
Rural	Golf Course / Cage	16, 17
Urban	Derring Hall	18, 19
Urban	Drillfield	20, 21, 22

At each receiver location, two orthogonal tracks are measured in a local area. The tracks are either in an L-shape as shown in Fig. (2.8) or in a plus-shape. Each measurement track is 20λ (3.33 m) long with a PDP measurement done every $\frac{\lambda}{4}$ (4.17 cm). Twenty wavelengths represents enough channel data to simulate a 147 ms data burst for a receiver moving at 50 mph, the maximum speed anticipated for use of the HMT. Thus, at minimum, the channel for the HMT can be simulated through a complete frame of data. For lower vehicle speeds or for pedestrian usage, the same

channel data can be used to simulate multiple frames of data.

1.4 Organization of the Report

This thesis is organized to allow the reader to understand the time and angle dispersion characteristics of the measured peer-to-peer channel. Analyses of the measurement system (Chapter 2), AOA models (Chapter 3), and angular spread measurement techniques and error (Chapter 4) are presented first. Next, the descriptions of all 22 measured links are presented by showing maps, pictures, and a detailed textual description of each transmitter and receiver location and the area in between (Chapter 5). After that, the measurement results are presented. The results (Chapter 6) deal both with wideband characteristics and with angular spread characteristics. Finally, the measurement-based channel model resulting from the measurements is presented (Chapter 7). The results and outcomes of this thesis are then summarized (Chapter 8).

Chapter 2

Sliding Correlator Measurement System

The sliding correlator measurement system is a wideband RF channel-sounding system. In an analogy to sound wave propagation, the measurement system measures the echoes in the received signal caused by radio wave propagation in the surrounding environment. It measures echoes by calculating the correlation of the received signal with the transmitted signal. A problem with measuring radio wave echoes is that they arrive so closely in time that it is necessary for the measurement system to uses a sliding correlation technique that effectively *slows down* time. This chapter introduces both the operation of the correlator and the sliding mechanism. Understanding of the correlation properties of the pseudo-noise (PN) sequence used by the measurement system are essential to understand the measurement outputs reported in this report. In order to effectively introduce pseudo-noise signal correlation properties, this chapter first presents the correlation properties of noise signals. Example measurement systems are presented to show how the mathematics is realized in common digital and RF hardware. The block diagrams of these example systems are very similar to the block diagram of the measurement system. Indeed, the measurement system block diagram will seem familiar when introduced in the later sections of this chapter. The transmitter and receiver of the measurement system are both detailed. This chapter also describes the antennas and the linear track used for the measurements. Measurements with the sliding correlator measurement system require calibration and time-averaging, and these operations are described at the end of this chapter.

2.1 Mathematical Analysis

In this section, we develop the mathematical basis for channel sounding using a sliding correlator measurement system. We first consider a white Gaussian noise signal. Its simple autocorrelation properties make it a good introduction to the basics of channel sounding. Then we analyze the autocorrelation properties of the pseudo-noise signal and show its frequency characteristics. The effects of sliding correlation are also discussed.

2.1.1 Correlation Properties of Noise

Consider the correlation properties of white Gaussian noise. The autocorrelation function $R_n(\tau)$ of white Gaussian noise is a weighted impulse function,

$$R_n(\tau) = E[n(t)n*(t-\tau)] = N_0\delta(\tau) \tag{2.1}$$

where N_0 is the noise power spectral density.

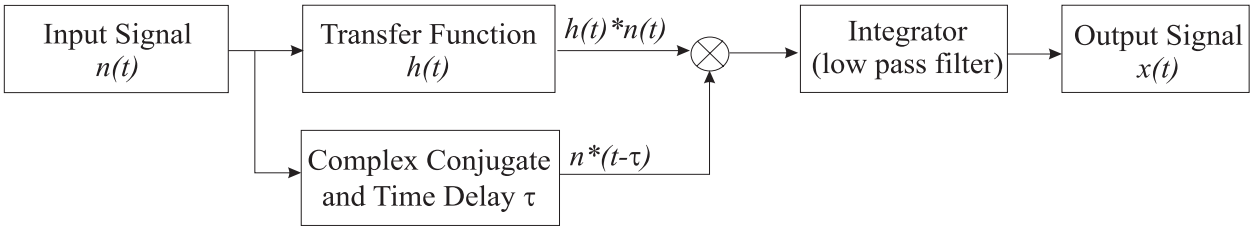

Figure 2.1: A measurement system used to measure the unit impulse response of a filter

To see the usefulness of this autocorrelation property, consider the measurement system shown in Fig. 2.1. A noise function, $n(t)$, is passed through a filter, $h(t)$. The filter output is a convolution given by

$$y(t) = \int_{-\infty}^{\infty} h(\beta)n(t-\beta)d\beta. \tag{2.2}$$

The combination of the multiplier and the integrator effectively calculates the cross-correlation of the filtered signal and the time-delayed input signal. Recall that the definition of cross-correlation is given by

$$R_{g_1 g_2}(t_1, t_2) = E\left[g_1(t_1)g_2^*(t_2)\right]. \tag{2.3}$$

Thus the output signal $x(\tau)$ is given by

$$\begin{aligned} x(\tau) &= E\left[\int_{-\infty}^{\infty} h(\beta)n(t-\beta)d\beta\, n^*(t-\tau)\right] \\ x(\tau) &= \int_{-\infty}^{\infty} h(\beta)E[n(t-\beta)n^*(t-\tau)]d\beta. \end{aligned} \tag{2.4}$$

Note that the definition of the autocorrelation of a signal is given by

$$R_g(\tau) = E\left[g(t)g^*(t-\tau)\right]. \tag{2.5}$$

The left side of this equation is the same form as the expected value term in Eq. (2.4). We can replace it with the autocorrelation function of noise, $R_n(\tau)$.

$$\begin{aligned} x(\tau) &= \int_{-\infty}^{\infty} h(\beta)N_0\delta(\tau-\beta)d\beta \\ x(\tau) &= N_0 h(\tau) \end{aligned} \tag{2.6}$$

Thus using the measurement system shown in Fig. (2.1), we can exactly measure the impulse response of the filter $h(\tau)$ at all times τ. The difficulty with this system is that it requires perfect knowledge of the signal $n(t)$. In a real channel measurement situation, the input signal needs to be known at both the transmitter and receiver. This is impossible with an infinite bandwidth noise signal. Therefore we use a reasonable substitute, a pseudo-noise signal.

2.1.2 Correlation Properties of Pseudo-Noise

The PN signal used in the sliding correlator is a wideband digital signal. It is made up of a seemingly random binary sequence often referred to as a spreading code. Let $p(t)$ represent the pseudo-noise signal.

The PN signal has properties similar to noise. Like the autocorrelation function of noise, the autocorrelation function of the PN signal, $R_p(\tau)$, peaks at $\tau = 0$. $R_p(\tau)$ exhibits a very narrow triangular pulse at $\tau = 0$ similar to the impulse function in $R_n(\tau)$ at $\tau = 0$. However, $R_p(\tau)$ is unlike $R_n(\tau)$ since $R_p(\tau)$ is a periodic signal. $R_p(\tau)$ has a period $T_b = NT_c$, where N is the sequence length and T_c is the chip period. The autocorrelation function for the ideal PN signal is given by

$$R_p(\tau) = \begin{cases} 1 - \frac{1+1/N}{T_c}\theta & 0 \le \theta < T_c \\ -1/N & T_c \le \theta < T_b - T_c \\ 1 + \frac{1+1/N}{T_c}(\theta - T_b) & T_b - T_c \le \theta < T_b \end{cases} \tag{2.7}$$

where $\theta = \tau \bmod T_b$. This autocorrelation function is plotted in Fig. 2.2.

The power spectral density of the PN signal is the Fourier transform of the autocorrelation function. Since $R_p(\tau)$ is a periodic signal, its Fourier Transform is the sum of impulse functions [19],

$$\begin{aligned} S_p(f) &= \mathcal{F}\left\{R_p(\tau)\right\} \\ S_p(f) &= \left[\sum_{n=-\infty}^{\infty}(N+1)\frac{sin^2(\pi n/N)}{(\pi n)^2}\delta(f-\frac{n}{T_b})\right] - \frac{\delta(f)}{N} \end{aligned} \tag{2.8}$$

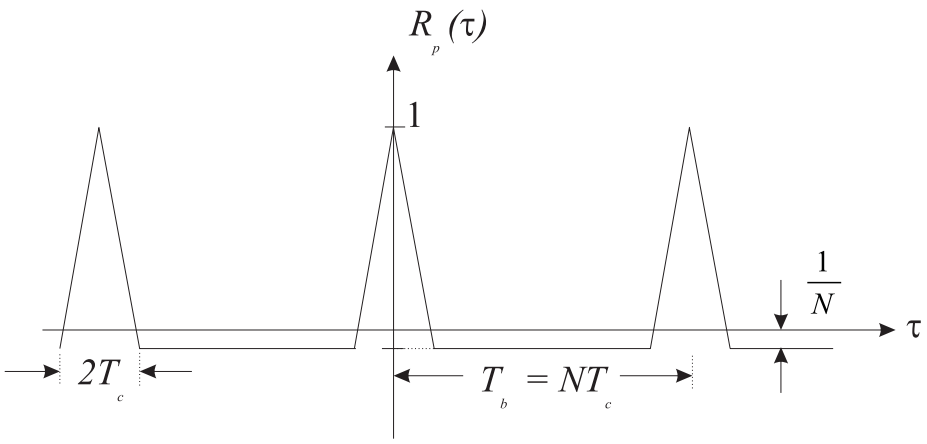

Figure 2.2: The autocorrelation function for the ideal PN signal is a periodic signal.

The envelope of $S_p(f)$ is proportional to the $sin^2(\pi T_c f)/(\pi T_c f)^2$ function, which has zeros at integer multiples of $1/T_c$ (except at zero). Thus the null-to-null bandwidth of the power-spectral density of the PN signal is $2/T_c$. In these measurements, the PN signal is clocked at $T_c = 10$ ns for a null-to-null bandwidth of 200 MHz.

Now consider again the measurement system in Fig. (2.1). Replace $n(t)$, the white Gaussian noise signal, with $p(t)$, the pseudo-noise signal. Note that the pseudo-noise signal used in these measurements was purely real. Therefore the complex conjugation was not performed. The output of the system, $x(t)$, is still the cross-correlation of the input signal with a time-delayed version of the input signal, $p(t-\tau)$, as given by:

$$\begin{aligned} x(\tau) &= E[\int_{-\infty}^{\infty} h(\beta)p(t-\beta)d\beta p(t-\tau)] \\ &= \int_{-\infty}^{\infty} h(\beta)E[p(t-\beta)p^*(t-\tau)]d\beta \\ &= \int_{-\infty}^{\infty} h(\beta)R_p(\tau-\beta)d\beta \end{aligned} \tag{2.9}$$

So far we have considered a general filter $h(t)$. Now consider the discrete multipath channel impulse response model given by

$$h(t) = \sum_{i=1}^{K} \alpha_i e^{j\phi_i}\delta(t-\tau_i) \tag{2.10}$$

where K is the number of multipath. The amplitude, phase, and time delay of the ith multipath are given by α_i, ϕ_i, and τ_i, respectively [20].

Using Eq. (2.10) as the filter for Eq. (2.9), the output of the measurement system is given by

$$x(\tau) = \sum_{i=1}^{K} \alpha_i e^{j\phi_i} R_p(\tau - \tau_i). \tag{2.11}$$

We call $|x(\tau)|^2$ the PDP of the channel. Eq. (2.11) shows that the PDP is the squared magnitude of a phasor sum of K autocorrelation functions. If we neglect the small $(-1/N)$ correlation in-between the peaks (see Fig. 2.2) then $|x(\tau)|^2$ only has overlapping correlation peaks when multipath delays, τ_i, are closer than $2T_c$ to each other.

Furthermore, when multipath components do overlap, they are the phasor sum of triangular correlation peaks. Fig. (2.3) shows the result of the sum of two identical-amplitude differing-phase correlation peaks caused by multipath components with time delays separated by only T_c. It is apparent that the unambiguous multipath component resolution of the measurement system is $2T_c$. It is possible for two multipath components to be distinguished at $\Delta\tau$ less than $2T_c$, however, it becomes less probable with decreasing time-delay separation. It also becomes improbable if one of the multipath components has a much stronger amplitude than the other.

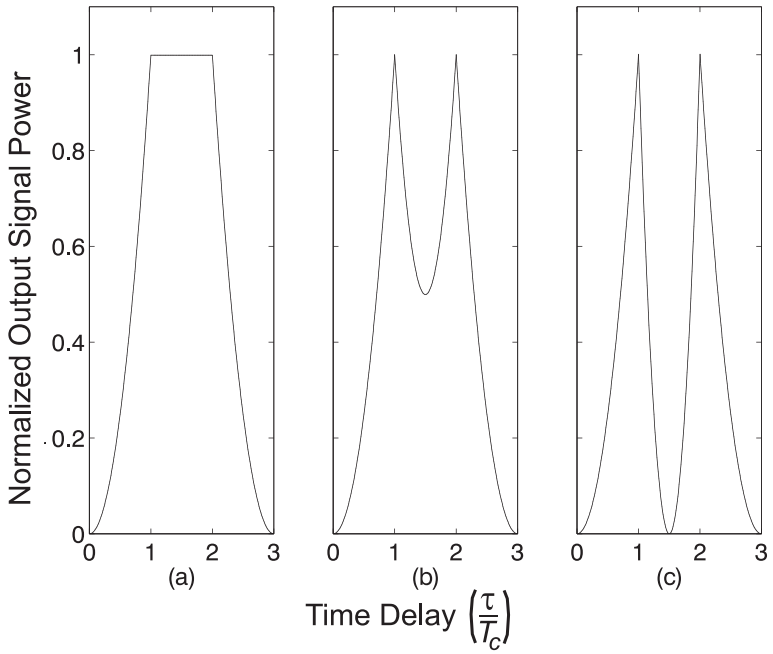

Figure 2.3: Two multipath separated by T_c may or may not be resolvable depending on their phases ϕ_i. Here the magnitude sum of two equal-amplitude $R_p(\tau - \tau_i)$ with $\tau_2 - \tau_1 = T_c$ are shown with (a) $\phi_2 - \phi_1 = 0$, (b) $\phi_2 - \phi_1 = 90^o$, (c) $\phi_2 - \phi_1 = 180^o$. The x-axis has units of τ/T_c.

2.1.3 Sliding Correlation

In the past two sections, our measurement system tested the filter's impulse response only at a particular time delay, τ. To measure the complete impulse response of the filter we must vary τ from time zero until the end of the impulse response. In a sliding correlator measurement system, the *sliding* of τ is realized by using slightly different clock rates at the two PN signal generators.

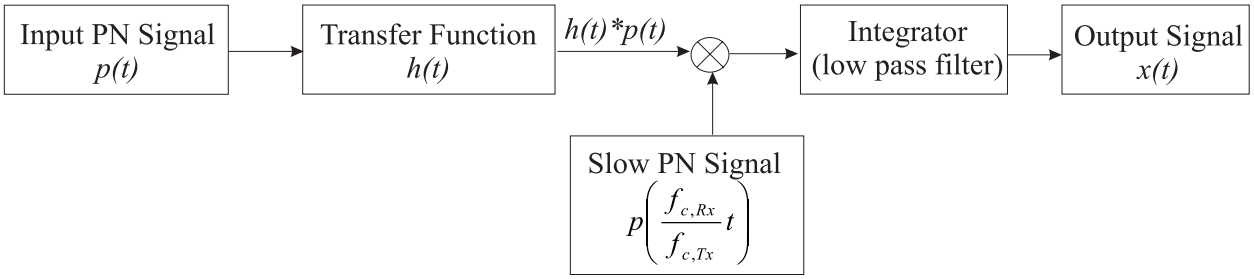

Figure 2.4: A measurement system used to measure the unit impulse response of a filter on a sliding scale using PN signals clocked at different rates

To see how sliding correlation works, the measurement system in Fig. (2.1) has been modified to Fig. (2.4). Call the transmitter clock rate at f_c, so that $T_c = 1/f_c$ and $T_b = NT_c$. The receiver clock rate, $f_{c,Rx}$, has been slowed so that

$$f_s = f_c - f_{c,Rx} \tag{2.12}$$

where the difference in the clock rates, f_s (called the *slip rate*), is much slower than either transmitter or receiver clock rates. The period of the receiver PN signal is stretched out in time compared to the transmitter PN signal. Therefore the receiver PN sequence can be represented as

$$p\left(\frac{f_c - f_s}{f_c}t\right). \tag{2.13}$$

The output of the measurement system in Fig. (2.4) is now given by

$$\begin{aligned} x(t) &= E\left[\int_{-\infty}^{\infty} h(\beta)p(t-\beta)d\beta\, p(\frac{f_c - f_s}{f_c}t)\right] \\ x(t) &= \int_{-\infty}^{\infty} h(\beta)E\left[p(t-\beta)p(t-\frac{f_s}{f_c}t)\right]d\beta \end{aligned} \tag{2.14}$$

The expected value term in Eq. (2.14) is very similar to the form of the definition of the auto-correlation function in Eq. (2.5) except that the term $\frac{f_s}{f_c}t$ is not a constant. The output of the measurement system becomes:

$$x(t) = \int h(\beta)R_p(\frac{f_s}{f_c}t - \beta)d\beta$$

$$x(t) = \int \sum_{i=1}^{K} \alpha_i e^{j\phi_i} \delta(\beta - \tau_i) R_p(\frac{f_s}{f_c}t - \beta) d\beta$$

$$x(t) = \sum_{i=1}^{K} \alpha_i e^{j\phi_i} R_p(\frac{f_s}{f_c}t - \tau_i) \quad (2.15)$$

The most significant result of sliding correlation is that the output of our measurement system, $x()$, is now a function of time. Without sliding correlation, the output was only a function of τ. We would have had to physically adjust the value, τ, of the delay in the measurement system, in order to see more of $x(\tau)$. Now, with sliding correlation, the passage of time alters the delay for us.

The alteration of the time delay is slowed because of the factor $\frac{f_s}{f_c}$. This fraction is usually very small, in fact, in the sliding correlator measurement system used in this project, $\frac{f_s}{f_c} = 10^{-4}$. We use a PN signal with $N = 2047$, and during the period of the PN signal, $T_b = NT_c$, the $\frac{f_s}{f_c}t$ has only changed by one-fifth of T_c. It takes a relatively long time to complete a sweep across the period of R_p. Thus we must assume that the channel is static during the sweep time.

For more intuitive understanding of this, note that the multipath peaks will appear when the term inside $R_p()$ is zero. That is, when

$$t = \frac{f_c}{f_s}\tau_i = \gamma\tau_i \quad (2.16)$$

where γ is the factor by which we have slowed the time scale, $\frac{f_c}{f_s}$. In these measurements, $\gamma = 10^4$. The end result is that we can watch the arrival of multipath components orders of magnitude slower than they actually arrive. We assume that the channel is static for a period of γT_b. In our measurement system that period is $(10^4)(2047)(1/100MHz) = 0.20$ s.

The measurement system shown in Fig. (2.4) shows the concepts of sliding correlation in a baseband example. The MPRG measurement system applies these concepts at an carrier frequency of 1.8 GHz [16, 21]. The operation of this measurement system, including transmitter and receiver block diagrams, antenna pattern and positioning, and system calibration are discussed in the following sections.

2.2 Transmitter Setup

The transmitter block diagram is shown in Fig. (2.5).

One of the most difficult problems of the sliding correlator concept is the maintenance of accurate clock frequencies at both the transmitter and the receiver. The MPRG measurement system solves

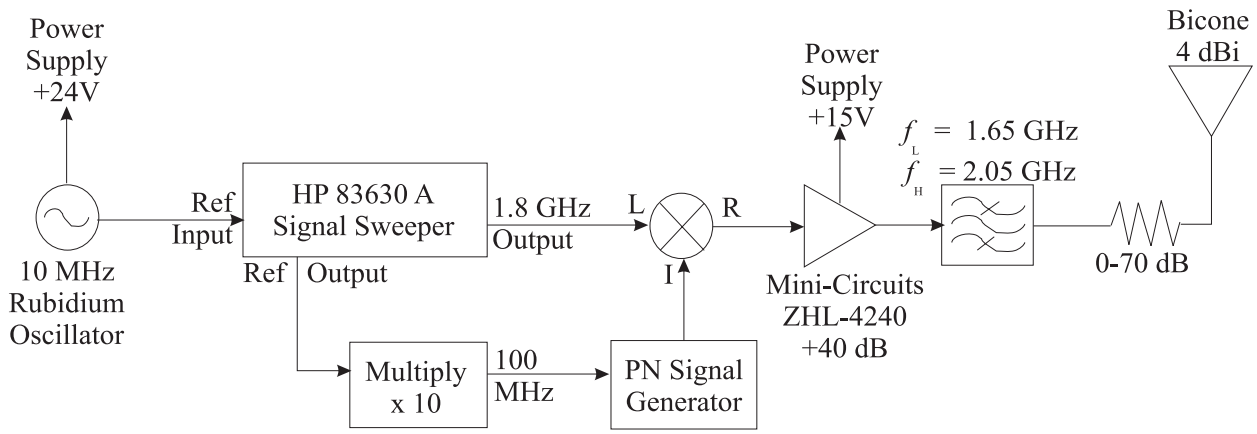

Figure 2.5: Block diagram of the transmitter for a center frequency of 1.8 GHz

this problem by keeping a very accurate time base through use of 10 MHz Rubidium frequency standards [16]. The output of the Rubidium oscillator provides a reference to the 1.8 GHz local oscillator. It is also multiplied by 10 to generate a 100 MHz clock frequency for the PN signal generator. The PN signal is a maximal length sequence generated using an 11-element shift register. Accordingly, the length of the sequence is $N = 2047$.

The HP 83630A Signal Sweeper is used to produce a 1.8 GHz CW signal which serves as the local oscillator (L.O.). This L.O., together with a Mini-Circuits ZEM-4300 mixer, serves to upconvert the PN signal to the desired carrier frequency. The RF signal is amplified by a Mini-Circuits ZHL-4240 power amplifier. The output level of the amplifier may be controlled by a step attenuator with a range of 0-70 dB in 10 dB increments. Except for calibration and close transmitter-receiver links, this attenuator is set to 0 dB. The output is then bandlimited by a custom Lark filter to a 3-dB bandwidth of 400 MHz. The transmission and reflection characteristics of this filter are shown in Fig. (2.6)

The transmitter power (EIRP) is 1 W when the attenuator is set to 0 dB.

2.3 Antennas

The transmitter and receiver both use a biconical antenna. The bicones are advantageous for their wide bandwidth and their uniform radiation pattern in the azimuth plane. They have an antenna gain of 4 dB with respect to an isotropic antenna. In the vertical plane, the radiation pattern has its maximum gain along the azimuth and a 3-dB beamwidth of 30^o. An idealized drawing of the

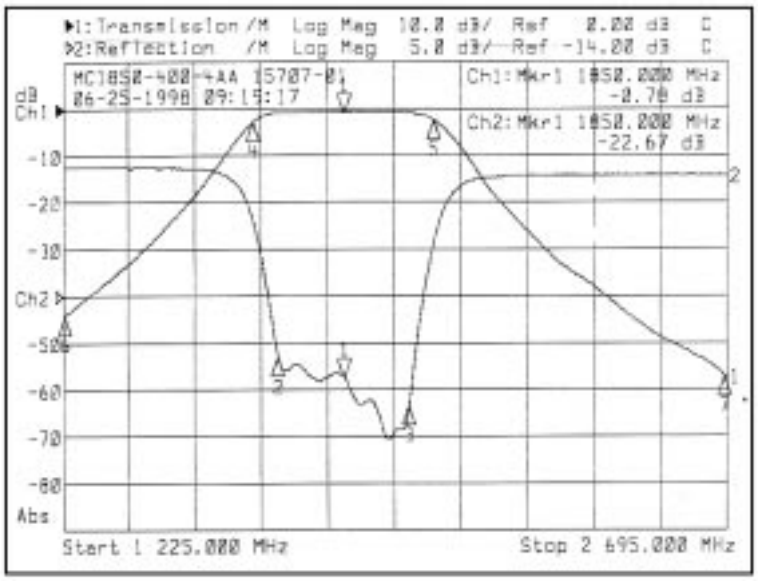

Figure 2.6: Transmission and reflection characteristics of the RF passband filter

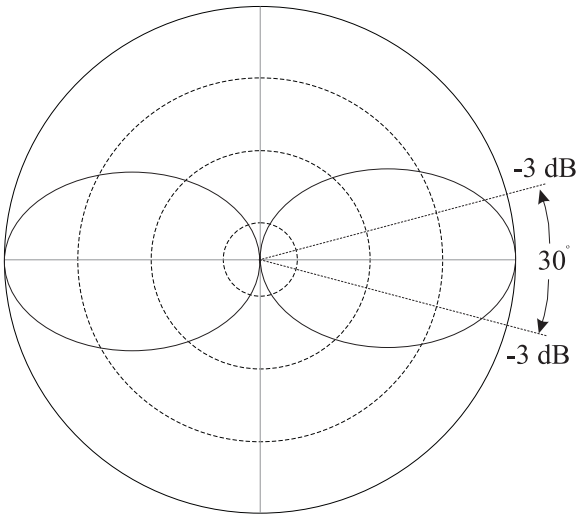

Figure 2.7: The vertical-cut radiation pattern of the bicone antenna

vertical cut radiation pattern is shown in Fig. (2.7. In our measurements, we can assume that we do not receive power at an angle higher than 10^o in elevation or lower than -5^o in elevation. This assumption is valid for the transmitter-receiver links measured for this project, as described in the sections below. This assumption allows us to use the link budget equation to make a good engineering estimate of the path loss, as will be discussed in Section 6.

2.3.1 Antenna Positioning

The antennas are placed to correspond to the normal operational height for the HMT. The HMT is a portable device that will be used at the head level of a user either on foot or in a vehicle. The device communicates with other HMT units at approximately the same height via a peer-to-peer random access network. Thus both the receiving and transmitting antenna heights in our measurement campaign are kept at about 1.7 m above the ground.

The receiving antenna is mounted on top of the measurement cart on a wooden table. The antenna rests in a $10\lambda = 4/3$ m linear track, as seen in Appendix E in Fig. (E.3.3). Marks $\lambda/4 = 1/24$ m apart identify the 40 positions where the antenna can be placed. Since a 20λ set of measurements is required, two adjacent placements of the cart are necessary. Thus to measure two orthogonal 20λ tracks, we position the cart 4 times. The tracks either make an L-shape as shown in Fig. (2.8) or a plus-shape and are all within a local-area. The need for the measurement of orthogonal tracks is described in Section 4.1.

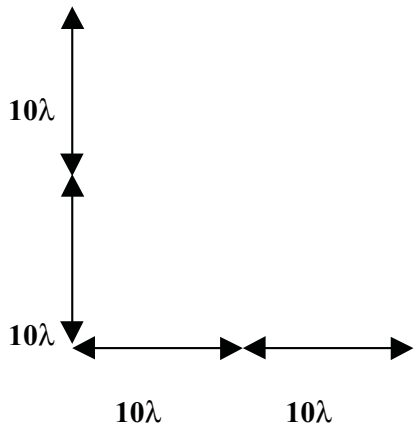

Figure 2.8: Orthogonal 20λ track measurements are conducted in four sets of 10λ measurements.

The transmitting antenna is placed on a tripod and kept at 1.7 m. The tripod allows more flexibility

in positioning than the cart, since the antenna can be easily kept precisely horizontal using the level and the angle adjustments on the tripod. The level of the receiving antenna depends on the leveling of the cart. This is accomplished by choosing relatively flat places to conduct track measurements, even in hilly terrain.

2.4 Receiver

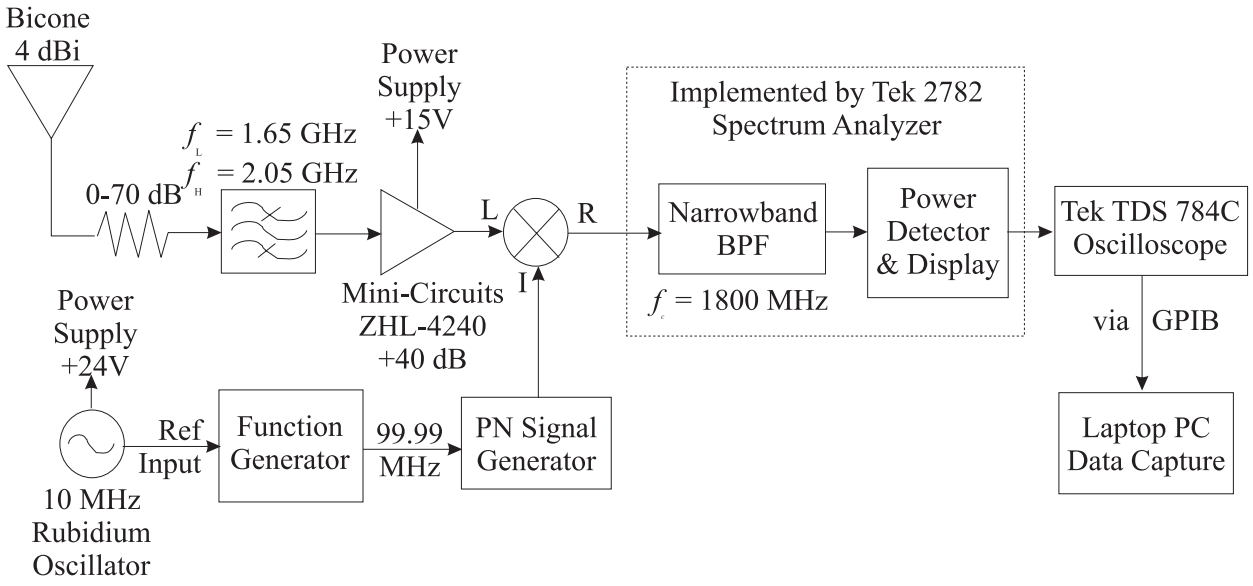

Figure 2.9: Block diagram of the receiver for a center frequency of 1.8 GHz

The receiver, whose block diagram is depicted in Fig. (2.9), performs the sliding correlation operation at RF. The received signal is filtered and then amplified. The reconditioned signal is then mixed with a replica of the transmitted PN signal via a Mini-Circuits ZEM-4300 mixer. However, this receiver PN signal generator uses a clock of 99.99 MHz. This results in a slip frequency, $f_s = 10$ kHz. The time scale factor is $\gamma = \frac{f_c}{f_s} = 10^4$. When the received signal and the receiver PN signal are mixed, the resulting signal has a much narrower bandwidth. Note that this narrowband signal is still at 1.8 GHz. The bandwidth of the sliding correlation signal is 20 kHz. The spectrum analyzer is set to zero-span at 1.8 GHz. It has several narrowband settings, and we use the smallest-bandwidth filter above 20 kHz, a 30 kHz filter. The spectrum analyzer then downconverts the sliding correlation signal for display on the screen. This is not a good means for display or for PC capture, however, for several reasons. The spectrum analyzer display does not have a trigger mechanism or a time scale control. Also, the waveform on the spectrum analyzer has not

been digitized or averaged with previous waveforms. For these purposes, we transfer the spectrum analyzer voltage output to a digital oscilloscope. The scope triggers on the first arriving multipath component, digitizes the signal, and averages several waveforms together before transferring the data to the PC.

Note that the scope has measured voltage. Calibration data is used to convert this voltage into a dB received power value (see Section 2.5).

2.4.1 Data Transfer and Storage

The averaged PDPs are captured from the Tektronix 784 Oscilloscope to a laptop PC using a National Instruments PC-Card GPIB interface card. A data transfer program called *tdslog* was downloaded from the Tektronix web site, *www.tek.com\support*. The C++ source code was edited for the specific needs of this campaign. Specifically, the data capture program pauses while the antenna is advanced to the next position and then standardizes the filenames of each captured waveform for ease of post-processing.

The PDPs are saved in Tektronix *.isf* format, which saves each fixed-point sample in one byte. With overhead added, our 5000-sample PDP takes up about 6 kB. Each day we recorded about 500 power delay profiles for a total storage requirement of about 3 MB. The data was backed to Zip disk and downloaded to mainframes for post-processing. The quantization is uniform across the range of the received voltages. Typically this translates into a quantization step of $\Delta P = 0.5$ dB.

2.5 Calibration

The sliding correlator measurement system requires frequent calibration. As discussed in Section 2.4, the receiver measures the voltage on an oscilloscope. This voltage is proportional to the correlation between the received signal and the locally generated PN signal. In order to translate this voltage into a dB path loss value, a calibration profile is required.

The calibration is done by disconnecting the transmitter and receiver at their antennas. They are then connected back-to-back with a step attenuator. This additional attenuator has a 1-dB step size and ranges from 0-11 dB. Combined with the 0-70 dB step attenuators in the transmitter and receiver, we have an attenuation range of 0-151 dB with a 1-dB step size.

Setting several different attenuation levels using the step attenuators, we record the corresponding waveforms on the oscilloscope. The maximum scope voltage should be directly proportional to the dB attenuation. We record 40 pairs of calibration data, maximum scope voltage and dB attenuator setting, and calculate the linear relationship using a least squared-error fit. Thus we can translate between scope voltage, V and dB attenuator setting $A(V)$,

$$A(V) = \alpha V + \beta. \tag{2.17}$$

The path loss is not simply this dB attenuator setting. This is because we disconnected the antennas during calibration. Each antenna has an antenna gain associated with it. Thus the path loss between transmitter and receiver can be calculated from the voltage on the scope and the gains of the two antennas.

$$PL_{dB} = A(V) + G_{Tx} + G_{Rx}. \tag{2.18}$$

As discussed in Section 2.3, we can assume that the received power arrives very close to the azimuth, so that $G_{Tx} = G_{Rx} = 4dB$. Thus, $PL_{dB} = A(V) + 8dB$.

A sample calibration profile is shown in Fig. (2.10). This is the calibration profile taken when measuring the forest site, which is described in Chapter 5.

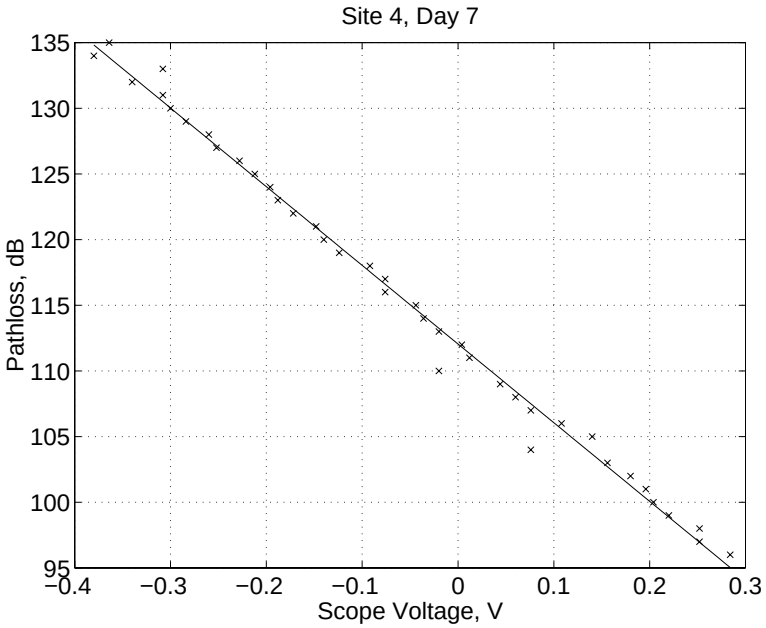

Figure 2.10: A sample calibration profile. Measured data is shown as x's, and the calculated path loss formula is shown as a solid line.

The calibration may be sensitive to temperature. In the course of the operation of the measurement

equipment, we expect that its temperature will rise due to its own power and to direct sunlight. Measurements are typically done on sunny days with temperatures between 30^o and 35^o C. To adjust for the change in response to temperature, we allow the measurement equipment to be set up in the sun and powered on for a half hour before beginning the calibration and measurements. On several occasions, calibration is also done at the end of the day to verify the initial calibration. In all cases, the starting calibration is very close to the ending calibration – calculated path loss values calculated from both calibrations are at most 0.5 dB apart from each other. This gives us confidence that the calibration parameters were relatively constant throughout each day.

2.6 Time-Averaging and Transient Effects

It has been shown that received amplitudes of multipath vary in time even with a stationary transmitter and receiver. These small multipath amplitude variations are due to channel transients such as wind, pedestrians, and automobiles. The multipath amplitude of a stationary receiver over time has been characterized by log-normal or Rician distributions [22]. For high K-values of a Rician distribution, we can sometimes approximate the distribution as log-normal. In order to reduce the time effects, we used the waveform averaging feature of our digital oscilloscope. Since the voltage on the scope is proportional to the dB received power, the scope is effectively doing a dB average of the waveforms. For a log-normally distributed variable with variance σ^2 dB, the resulting average of N values has a variance of σ^2/N dB.

The assumption of independent, identically distributed multipath amplitudes is a best-case scenario – in a real channel, the transient effects are worse. Moving pedestrians and cars not only obstruct multipath components, they create new ones. If you watch the PDP of a channel as a car drives through, you often can see the multipath component caused by its scattering. If the car is traveling transverse to the LOS (line between transmitter and receiver), then the component appears at a large time delay. This time delay decreases as the car approaches the LOS, and then increases again as the car drives away.

Averaging is our attempt to remove these channel transients from our measurement environment. It is true they are part of the channel within which the communications device must operate. However, our measurement system cannot measure them quickly enough with its update period of about 0.2 s. The system averages 10 waveforms, for a total of two seconds. A quickly-moving vehicle would travel through the channel within the time for one measurement. The multipath it caused in one PDP would not appear at all in subsequent PDPs. Thus transient multipaths were

a distraction to the track measurements.

Averaging reduces their effect. As discussed above, the multipath from a moving car would appear at a different time delay in subsequent waveforms. Since 10 waveforms are log-averaged, the effect of the transient multipath is significantly reduced.

2.7 Conclusion

This section has shown the ability of the sliding correlator measurement system to measure impulse response characteristics of the peer-to-peer channel. The limitations of the PDP are that it does not measure phase – only the signal envelope can be determined from its output. In addition, its limited bandwidth causes multipath that arrive close together in time to be grouped together. Another limitation of the measurements is the accuracy of the system. We attempt to measure channel PDPs in a dynamic environment, which adds error to the measurements. These limitations, the finite bandwidth and the measurement error, will be major topics of discussion in this thesis.

Chapter 3

AOA Models and Angular Spread

Before presenting the results of this measurement campaign, it would be useful to have some analytical tools to evaluate wideband angular spread measurements. We would like to know the expected relationship of angular spread and time delay. This chapter will provide analytical tools useful for that purpose.

As discussed in Section 2.1.2, all multipath that arrive closer in time than $2T_c$ (the resolution of our measurement system) phasor-sum in the PDP. In this thesis, the angular spread is calculated (from measurements) for each power peak in the PDP. When we calculate the angular spread for all of the multipath that arrive *at the same time delay* τ, we refer to the multipath that arrive at close time delays such that they cannot be distinguished by the measurement system.

3.1 Definition of Angular Spread

The definition of angular spread was given by Durgin in [5, 6]. The basis for the theory is that the angular spread can be calculated when the AOA of the received power, $p(\theta)$, is known. The angular spread is defined as

$$\Lambda^2 = 1 - \frac{|F_1|^2}{|F_0|^2} \tag{3.1}$$

where F_n are the Fourier coefficients of $p(\theta)$ given by

$$F_n = \int_{-\pi}^{\pi} p(\theta) e^{jn\theta} d\theta. \tag{3.2}$$

The angular spread is always between 0 and 1. An angular spread of 1 indicates that arriving power

is not biased in a particular direction, while an angular spread of 0 indicates that all power arrives from one direction.

As will be discussed in detail in Section 4.1, the importance of this definition of angular spread is that Λ^2 is directly proportional to the fading rate variance of a receiver moving in an arbitrary direction. As the angular spread is discussed in this section, keep in mind that the discussion is also applicable to the fading rate variance if the angular spread is multiplied by a scale factor.

3.2 GBSBEM Angle-of-Arrival Model

The choice of an angle-of-arrival (AOA) model for a channel is determined by both the heights of the antennas and the type of environment between the transmitter and receiver [23]. Because of the low antenna heights at both ends of the link, the peer-to-peer channel requires a unique model.

The peer-to-peer channel is particularly suited to Liberti's Geometrically-Based Single-Bounce Elliptical Model (GBSBEM) in which each multipath is assumed to have scattered exactly once during its trip from the transmitter to the receiver [24]. The scatterer responsible for a multipath at a particular time delay is uniformly distributed along an ellipse that has the transmitter and receiver as foci, as illustrated in Fig. (3.1). At a time delay of τ and transmitter-receiver separation distance d, this elliptical perimeter for the scatterers is the locus of all points which result in a total path length of $d + c\tau$, where c is the speed of light in a vacuum. The model was originally proposed for microcellular systems in which the base station antenna is lower than the heights of the buildings. This is a good model for the peer-to-peer channel since the scatterers are just as likely to be near the transmitter as they are likely to be near the receiver.

In reality, multipath may undergo several reflections, diffractions, and scatterings before arriving at the receiver. However, these propagation mechanisms usually involve significant losses. An argument for the single-bounce model is that multipath that undergo several scatterings are less likely to have detectable received power levels. The validity of the assumption is further discussed in Sections 3.3 and 6.3.4.

As shown in Fig. (3.1), this model results in non-uniform AOA at the receiver. The angular distribution of arriving power is given by [24]:

$$f_L(\phi|r(\tau)) = \frac{(r^2(\tau)-1)^{1.5}(r^2(\tau)+1-2r(\tau)\cos\phi)}{\pi(2r^2(\tau)-1)(r(\tau)-\cos\phi)^3} \tag{3.3}$$

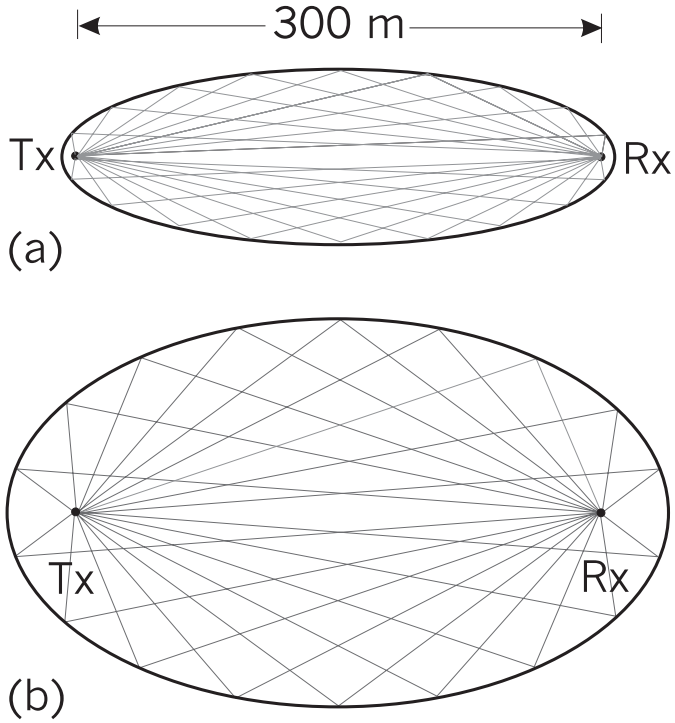

Figure 3.1: This figure shows the GBSBEM model for a separation distance of 300m. Represented are time delays of (a) 50 ns and (b) 260 ns. Several possible multipath are shown in gray. As the time delay increases, the ellipse becomes more circular, the multipath are more likely to arrive from a variety of angles, and the mean angular spread increases.

where ϕ is the angle of arrival variable and

$$r(\tau) = \frac{d + c\tau}{d} \tag{3.4}$$

is the ratio of the path length of the multipath ray to the path length of the LOS ray. As a result of Eq. (3.4), $r(\tau) \geq 1.0$.

3.3 Uniform Angle-of-Arrival Model

The GBSBEM assumption of a single scatter may fail under certain conditions. For example, from Fig. (3.1) we see that in the GBSBEM model, as the time delay increases, the location of scatterers moves away from the transmitter and receiver. But in fact, regardless of time delay, multipath that arrive at the receiver are also likely to interact with the operator of the receiver and the scatterers near him (automobile, nearby pedestrians and foliage, etc.). The scatterers near the transmitter are are also likely to cause additional multipath reflections and scatterings. As shown in Fig. (3.2), these scatters near the receiver can cause significant changes in the AOA characteristic. Essentially, the scattering near the receiver shown in Fig. (3.2) makes the AOA more uniform than can be described solely by the GBSBEM.

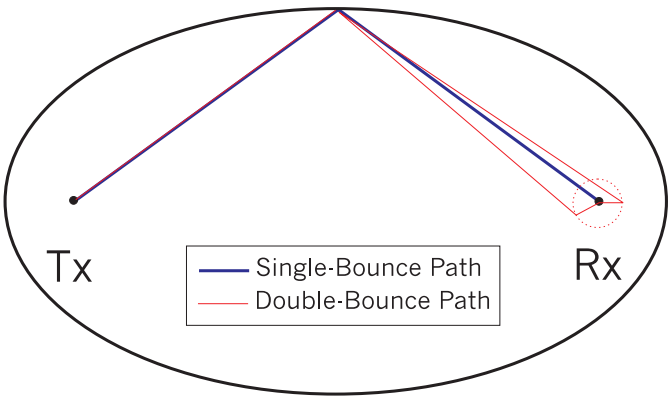

Figure 3.2: Shown is a single-bounce path from the GBSBEM model with the addition of double-bounce paths due to scatterers very close to the receiver. These multipath are likely to from angles not described well by the GBSBEM.

A model that may account for these multiple scatterings is the Uniform AOA Model, first proposed by Clarke [25]. This model simply says that at all time delays, the AOA of multipath are uniformly distributed along $[0, 2\pi)$. The Uniform AOA Model makes no assumptions about the number of

scatterings multipath undergo between the transmitter and receiver. The angular distribution of arriving power is given by:

$$f_U(\phi|r(\tau)) = \frac{1}{2\pi} \tag{3.5}$$

which is constant with $r(\tau)$ but the notation is kept the same as the GBSBEM distribution given in Eq. (3.3) for consistency.

3.4 Calculating the Expected Value of the Angular Spread

We cannot simply calculate the expected angular spread from a PDF like those given in Eq. (3.3) and Eq. (3.5). Recall that the angular spread is defined in Eq. (3.1) for the actual received power as a function of angle, while Eqs. 3.3 and 3.5 define the PDF describing the random variable of the AOA of each multipath. The arrival of waves may be described by a PDF, but the received power as a function of angle shows the angles-of-arrival and powers of the multipath that actually arrive. For example, if we receive only one multipath at time delay τ, even if its angle-of-arrival is described by the PDF in Eq. (3.3), the angular spread will be zero.

As we receive two or more multipath at time delay τ, the angular spread will be a function of the multipath angles-of-arrival. Using a model for the AOA, like the GBSBEM or Uniform AOA model, we can make statements about the expected value of the angular spread. As the number of waves n arriving with time delay τ increase, the expected value of the angular spread will go higher. As the number of multipath becomes very high, the mean angular spread, $E[\Lambda^2]$, will approach its maximum. Basically, in the limiting case as $n \to \infty$, the arriving power, $p(\theta)$, arrives from approximately all directions in the proportions given by the AOA PDF, $f(\phi|r(\tau))$. In this limiting case, $p(\theta) \propto f(\phi|r(\tau))$. Since the constant of proportionality will cancel out due to the definition of angular spread given in Eq. (3.1), the $E[\Lambda^2]$ as $n \to \infty$ can be found simply by calculating the Λ^2 for the PDF $f(\phi|r(\tau))$. The expected value, referred to mathematically as $E[\Lambda^2 \mid n \to \infty, r(\tau)]$, is also called the *maximum mean angular spread*.

3.4.1 GBSBEM Maximum Mean Angular Spread

The calculation of Λ^2 of $f(\phi|r(\tau))$ for the GBSBEM model is based on Eq. (3.1) and was first derived by Greg Durgin and I. The 0^{th} coefficient, $|F_0| = 1$, by the properties of the PDF. The first

Fourier coefficient is given by the expression

$$|F_1| = \left| \int_{\phi=-\pi}^{\pi} \frac{(r^2-1)^{1.5}(r^2+1-2r\cos\phi)}{\pi(2r^2-1)(r-\cos\phi)^3}(\cos\phi + j\sin\phi)d\phi \right| \tag{3.6}$$

which can be simplified by realizing that the PDF is even about ϕ and when multiplied by the $\sin\phi$ term will be odd and integrate to zero. The remaining integral can be split into two integrals,

$$|F_1| = \frac{(r^2-1)^{1.5}}{\pi(2r^2-1)} \left[\int_{\phi=-\pi}^{\pi} \frac{(r^2+1)\cos\phi}{(r-\cos\phi)^3} d\phi - \int_{\phi=-\pi}^{\pi} \frac{2r\cos\phi^2}{(r-\cos\phi)^3} d\phi \right] \tag{3.7}$$

which can both be solved with the aid of integral tables. The first and second integrals are given in [26] as Eq. (2.554.1) and Eq. (3.645), respectively. After much simplification, we have the result that

$$|F_1| = \frac{r}{2r^2-1}. \tag{3.8}$$

The Fourier coefficients are used in Eq. (3.1) to get the final result:

$$E[\Lambda^2 \mid n \to \infty, r(\tau)] = \frac{(4r^2-1)(r^2-1)}{(2r^2-1)^2}. \tag{3.9}$$

This maximum mean angular spread for the GBSBEM model is plotted in Fig. (3.3) as a function of $r(\tau)$. The angular spread increases with increasing $r(\tau)$ (or correspondingly, increasing τ). The increase in angular spread is shown graphically in Fig. (3.1 (a) and (b)). Part (a) of the figure shows a narrow ellipse. Its time delay corresponds to an $r(\tau)$ value of 1.05 and thus should have a maximum mean $\Lambda^2 = 0.24$. The ellipse in part (b) represents a higher time delay that corresponds to an $r(\tau)$ of 1.26. It appears more circular, and the figure shows that the arriving multipath are more evenly distributed between 0 and 2π. The maximum mean Λ^2 in this case is 0.67.

3.4.2 Uniform AOA Model Maximum Mean Angular Spread

Because the $f(\phi)$ is uniform across all angles, the first Fourier coefficient,

$$|F_1| = \left| \int_{\phi=-\pi}^{\pi} \frac{1}{2\pi}(\cos\phi + j\sin\phi)d\phi \right| \tag{3.10}$$

is equal to zero. From Eq. (3.1), $\Lambda^2 = 1$, and

$$E[\Lambda^2 \mid n \to \infty, r(\tau)] = 1. \tag{3.11}$$

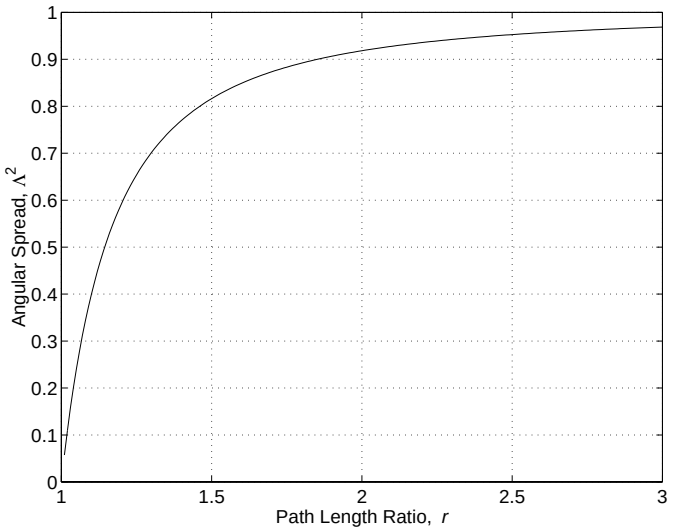

Figure 3.3: Plotted is the maximum mean angular spread, $E[\Lambda^2 \mid n \to \infty, r(\tau)]$, which shows the expected value of Λ^2 as the number of multipath arriving at the time delay τ goes very high.

3.5 Effect of Number of Multipath on Angular Spread

But what is the relationship between the number of multipath received at a given time delay, n, and the expected value of the angular spread? This question can be answered mathematically in several steps. These steps are:

1. Create the n-dimensional PDF for the angles-of-arrival of the n multipath received at time delay τ.
2. Formulate the angular spread assuming n equal-power multipath components and known angles-of-arrival.
3. Find the expected value of the expression for angular spread by integrating it across the n-dimensional PDF.

These steps are taken in the following sections.

3.5.1 Creating the n-Dimensional PDF

The n multipath angles-of-arrival, ϕ_1 through ϕ_n, are assumed to be independent of one another. They are all random variables with distribution described by Eq. (3.3). Since the ϕ_i are i.i.d., the

n-dimensional PDF of $f(\phi_1, \phi_2, ..., \phi_n | r(\tau))$ is simply the product of the individual distributions,

$$f(\phi_1, \phi_2, ..., \phi_n | r(\tau)) = \prod_{i=1}^{n} f(\phi_i | r(\tau)) \tag{3.12}$$

where ϕ_i is the AOA of the ith multipath component.

3.5.2 Finding the Expression for the Angular Spread

We can find the expression for the angular spread given n and the n values of the angles-of-arrival, ϕ_i. We assume that each multipath has the same received power, P, and thus the angular distribution of power is given by

$$p(\theta) = \sum_{i=1}^{n} P\delta(\theta - \phi_i). \tag{3.13}$$

The magnitude of the 0^{th} Fourier coefficient of $p(\theta)$ is simply the sum of the powers, $|F_0| = nP$. The magnitude of the first Fourier coefficient of this distribution is

$$|F_1| = \left| \sum_{i=1}^{n} P e^{j\phi_i} \right| \tag{3.14}$$

$$|F_1| = P \left[\left(\sum_{i=1}^{n} \cos\phi_i \right)^2 + \left(\sum_{i=1}^{n} \sin\phi_i \right)^2 \right]^{1/2} \tag{3.15}$$

$$|F_1| = P \left[\sum_{i=1}^{n} \sum_{k=1}^{n} \cos(\phi_i - \phi_k) \right]^{1/2}. \tag{3.16}$$

Then the angular spread can be calculated:

$$\Lambda^2(\phi_1, \phi_2, \ldots, \phi_n) = 1 - \frac{1}{n^2} \sum_{k=1}^{n} \sum_{l=1}^{n} \cos(\phi_k - \phi_l). \tag{3.17}$$

3.5.3 Solving the Expected Value

Finally we find the solution to

$$E\left[\Lambda^2(\phi_1, \phi_2, \ldots, \phi_n)\right] \tag{3.18}$$

which involves n integrations:

$$E[\Lambda^2 \mid n, r(\tau)] = \int_{-\pi}^{\pi} \int_{-\pi}^{\pi} \cdots \int_{-\pi}^{\pi} \Lambda^2(\phi_1, \phi_2, \ldots, \phi_n) f(\phi_1, \phi_2, ..., \phi_n | r(\tau)) d\phi_1 d\phi_2 \ldots d\phi_n. \tag{3.19}$$

Plugging in with Eqs. (3.12) and (3.17, we see that

$$E[\Lambda^2 \mid n, r(\tau)] = \int_{-\pi}^{\pi}\int_{-\pi}^{\pi}\cdots\int_{-\pi}^{\pi}\left[1 - \frac{1}{n^2}\sum_{k=1}^{n}\sum_{l=1}^{n}\cos(\phi_k - \phi_l)\right]\prod_{i=1}^{n} f(\phi_i|r(\tau))d\phi_1 d\phi_2 \ldots d\phi_n. \quad (3.20)$$

The constant 1 term will multiply the n-dimensional PDF and its integration, due to the definition of the PDF, will be 1.0. The remaining terms, $\cos(\phi_k - \phi_l)$ are equal to 1.0 when $k = l$. For these n cases, the integral will again result in 1.0 due to the definition of the PDF. When $k \neq l$, the terms $\cos(\phi_k - \phi_l)$ can be expanded to the form, $\cos\phi_k \cos\phi_l + \sin\phi_k \sin\phi_l$. The integral signs can be brought inside the summation signs and we have that

$$E[\Lambda^2 \mid n, r(\tau)] = 1 - \frac{1}{n} - \frac{1}{n^2}\sum_{k=1}^{n}\sum_{l=1,\ l\neq k}^{n}\int_{-\pi}^{\pi}\int_{-\pi}^{\pi}\cdots\int_{-\pi}^{\pi}[\cos\phi_k\cos\phi_l + \sin\phi_k\sin\phi_l] \quad (3.21)$$
$$\prod_{i=1}^{n} f(\phi_i|r(\tau))d\phi_1 d\phi_2 \ldots d\phi_n.$$

It is apparent that the n-dimensional integration can be separated into a product of n 1-dimensional integrations. Except for the integrals across ϕ_k and ϕ_l, the integrals will just be $\int_{-\pi}^{\pi} f(\phi_i|r(\tau))d\phi_i = 1.0$. We can rewrite Eq. (3.21) as

$$E[\Lambda^2 \mid n, r(\tau)] = 1 - \frac{1}{n} - \frac{1}{n^2}\sum_{k=1}^{n}\sum_{l=1,\ l\neq k}^{n}\left[\int_{-\pi}^{\pi} f(\phi_k|r)\cos\phi_k d\phi_k \int_{-\pi}^{\pi} f(\phi_l|r)\cos\phi_l d\phi_l\right. \quad (3.22)$$
$$\left. + \int_{-\pi}^{\pi} f(\phi_k|r)\sin\phi_k d\phi_k \int_{-\pi}^{\pi} f(\phi_l|r)\sin\phi_l d\phi_l\right].$$

Since $f(\phi|r(\tau))$ is an even function of ϕ (in both the Uniform AOA model and the GBSBEM), multiplication by $\sin\phi$ results in an odd function, for which integration across $[-\pi, \pi)$ gives a result of zero. The remaining two terms, $\int_{-\pi}^{\pi} f(\phi|r(\tau))\cos\phi d\phi$ are both equal to $|F_1|$, the first Fourier coefficient of the angular distribution. Thus Eq. (3.22) simplifies to

$$E[\Lambda^2 \mid n, r(\tau)] = 1 - \frac{1}{n} - \frac{n(n-1)}{n^2}|F_1|^2 \quad (3.23)$$

$$E[\Lambda^2 \mid n, r(\tau)] = \left(1 - \frac{1}{n}\right)(1 - |F_1|^2) \quad (3.24)$$

Since $|F_0|^2 = 1$ for a PDF, we can see from Eq. (3.1) that $\Lambda^2 = 1 - |F_1|^2$, where Λ^2 is calculated from the PDF. The angular spread calculated on a PDF, as we discussed in Section 3.4, is equal to the expected value of Λ^2 as n approaches ∞. Thus the expression

$$E[\Lambda^2 \mid n, r(\tau)] = \left(1 - \frac{1}{n}\right) E[\Lambda^2 \mid n \to \infty, r(\tau)] \quad (3.25)$$

gives the result for the mean angular spread as a function of n. Eq. (3.25) is a very general result - it is applicable to *any* PDF.

3.5.4 GBSBEM Mean Angular Spread

When Eq. (3.9) is applied to Eq. (3.25), we have the result,

$$E[\Lambda^2 \mid n, r(\tau)] = \left(1 - \frac{1}{n}\right) \frac{(4r^2 - 1)(r^2 - 1)}{(2r^2 - 1)^2} \tag{3.26}$$

which is the final result for the mean angular spread in the GBSBEM angle-of-arrival model. This result is plotted in Fig. (3.4) as a function of n and $r(\tau)$.

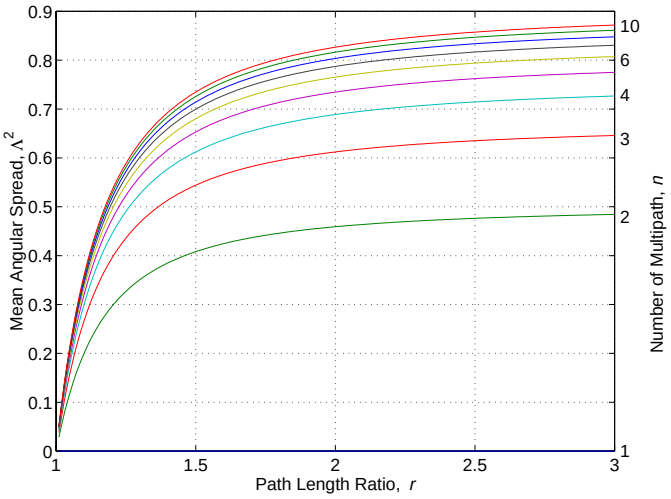

Figure 3.4: Plotted is the mean angular spread, $E[\Lambda^2 \mid n, r(\tau)]$ for the GBSBEM Model. Several values of n are plotted, and the value of n for each curve is given on the right-most side of the graph. As time delay increases or as the number of multipath increases, the mean angular spread also increases.

3.5.5 Uniform AOA Model Mean Angular Spread

When Eq. (3.11) is applied to Eq. (3.25), we have the mean angular spread for the Uniform AOA model,

$$E[\Lambda^2 \mid n] = 1 - \frac{1}{n}. \tag{3.27}$$

Note that the expression shows no dependence on $r(\tau)$. The plot of Eq. (3.27) is given in Fig. (3.5).

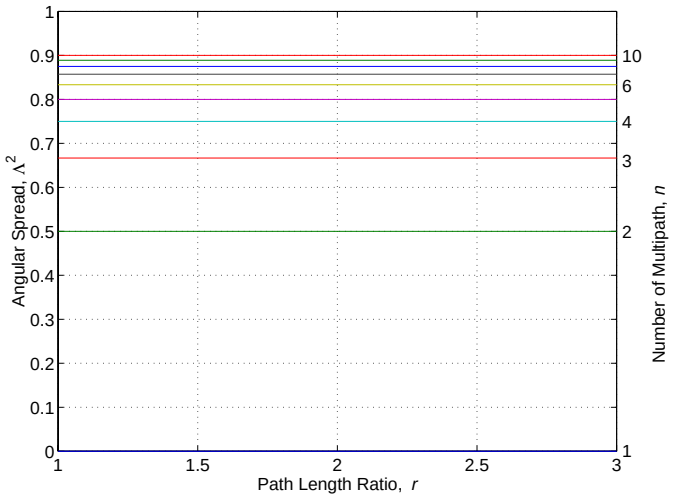

Figure 3.5: Plotted is the mean angular spread, $E[\Lambda^2 \,|\, n, r(\tau)]$ for the Uniform AOA model. Several values of n are plotted, and the value of n for each curve is given on the right-hand side of the graph. The mean is not a function of time delay. As the number of multipath increases, the mean angular spread also increases.

3.6 Applying a Model for n

Figs. (3.4) and (3.5) both show the mean angular as a function of n and $r(\tau)$. But what if n is a function of $r(\tau)$? Numerous measurements have indicated that this is the case. In this section, a few notable measurement results are mentioned, and their application to Eqs. (3.26) and (3.27) are shown.

Fig. (3.6) reproduces a figure from Turin [1] which shows the probability of at least one multipath occupying each 100 ns time-bin (the resolution of his measurement system) in his measured PDPs. Although this does not directly indicate *how many* multipath arrive in a time bin, it shows that many more multipath are likely to arrive within a single time-bin at lower time delays in his measured PDPs.

Turin also discussed the conjecture that the arrival times of the multipath form a Poisson sequence. In such a model, time delays relative to the LOS are i.i.d. random variables taking values in $(0, \infty)$. The probability of a multipath component arriving in the infinitesimal interval $(\tau, \tau + d\tau)$ is $p(\tau)d\tau$, where $p(\tau)$ is called the mean arrival rate at time delay τ. Turin noted two tendencies [1]:

1. Multipath components with low time delays relative to the LOS tend to arrive in *clusters* (not well described by Poisson statistics), and

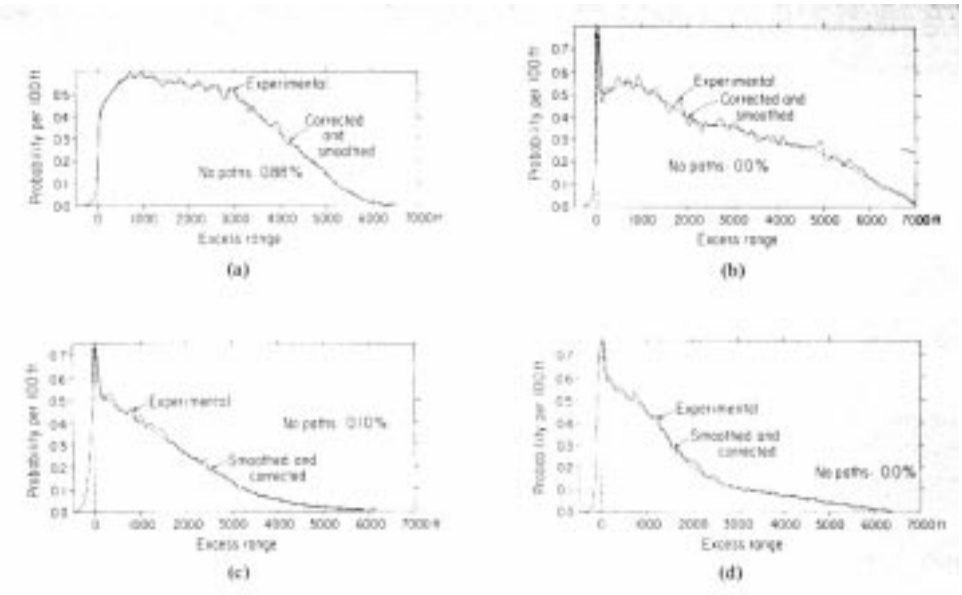

Figure 3.6: Probability of occupancy of time bins vs. time delay in four different measurement sites, taken from [1] Fig. (4).

2. Multipath components with long time delays tend to be more accurately modeled as Poisson sequences.

Other researchers have also modeled the multipath channel using this idea of the *clustering* of multipath [27, 28]. Clustering of multipath arrival times results in higher $n(\tau)$ compared to a Poisson sequence of arrival times. That is, when receiving a 'clustering' of multipath at a low time delay, the number of multipath arriving within the time resolution of the measurement system is likely to be higher than if the multipath had been independently distributed along the time delay axis.

Measurement of the number and power of multipath as a function of time delay is possible with systems that simultaneously measure the AOA and TDOA of multipath components [14, 15, 2]. While these systems may still have difficulty resolving two distinct multipath rays that arrive very close in angle, for the purpose of measurement of angular spread, these may as well be one ray. The measurement of four links in [2] led to the tabulation of number of multipath vs. time delay reprinted in Fig. (3.6).

Thus various measurements indicate that $n(\tau)$ will be high at low time delays and gradually decrease at higher time delays.

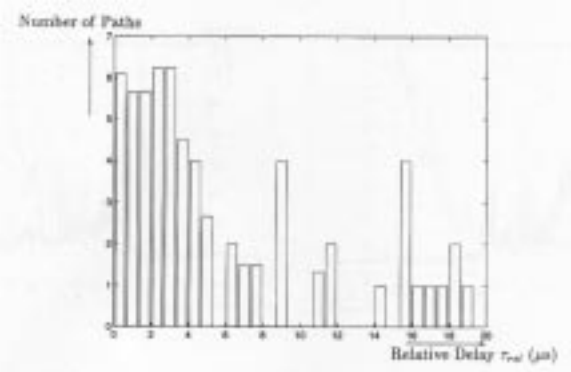

Figure 3.7: Number of paths and their relative delay for four links. Taken from [2].

If we had a function, $n(r)$, we could plug it into the GBSBEM formula in Eq. (3.26) or into the uniform model formula in Eq. (3.27). We could use the estimate of $n(r)$ to plot the expected value of the angular spread. This would give us a rule of thumb to help evaluate our measurement results. In Fig. (3.6), the uniform model mean angular spread is plotted as a function of τ. The 'x' marks represent an estimate of $n(\tau)$. If multipath power is received at time delay τ, the 'x' marks show how many multipath components should be expected to arrive at the same time within the resolution of the measurement system.

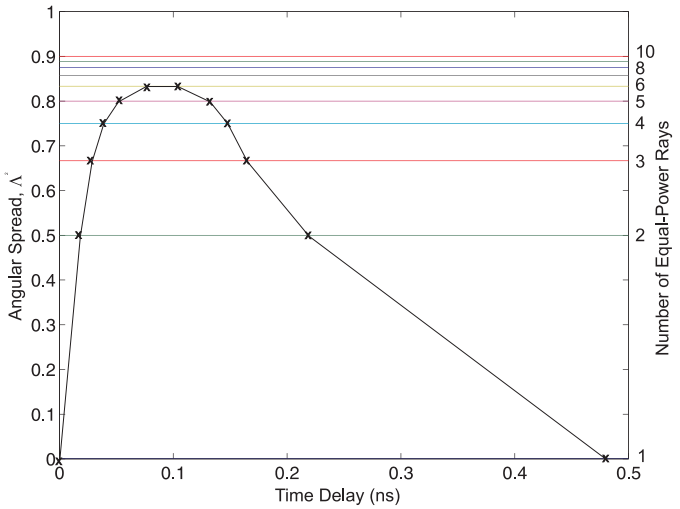

Figure 3.8: A model for $n(\tau)$ is overlaid onto the mean angular spread, $E[\Lambda^2 \mid n]$ for the Uniform AOA model. This model for $n(\tau)$ is just an example, but this figure shows how to apply an arbitrary model to show the expected relationship of Λ^2 with τ that will be seen in the measurement results.

Note that the number of multipath that arrive at time delay τ within the resolution of the measure-

ment system is clearly a function of the bandwidth of the measurement system. As the bandwidth increases, the time resolution capability decreases, and less multipath would appear to arrive at the same time.

3.7 Conclusion

In this chapter we have applied Durgin's definition of angular spread to two AOA models, the GBSBEM model and the Uniform AOA model. This chapter then showed some novel analysis dealing with the expected value of Λ^2. Section 3.4 derived the expected value of Λ^2 in the limiting case in which the number of multipath arriving at τ becomes very high. Section 3.5 then provided analysis which allows the calculation of the mean angular spread given the number of multipath components that arrive at the receiver at time delay τ (within the resolution of the measurement system). Combined with a model for the number of rays which arrive at the receiver, this analysis allows us to predict the angular spread as a function of time delay. An example application of a model for $n(\tau)$ is shown in Section 3.6.

The analysis in this chapter helps explain the angular spread measurement results. We will compare our measurement results to the analysis of this chapter for the purposes of validation of the measurements and for a comparison of the two models discussed here. This comparison will be presented in Section 6.3.

Chapter 4

The Measurement of Angular Spread

This chapter will show how the angular spread is calculated from measured PDPs. The angular spread is based on the fading rate variance, which itself depends on the change in power of a PDP power peak from one position to the next. The calculation of the the slope is not a trivial task.

Furthermore, transient measurement error is a major difficulty in the estimation of angular spread. In fact, this thesis will show that the calculated angular spread from measurements is not an *unbiased estimator*. However, if knowledge of the statistics of the error are known, an unbiased estimation of the angular spread can be made.

4.1 Review of Angular Spread Theory

The results of Durgin [5] are fundamental to this chapter and are repeated here for convenience. The remarkable result is that the angular spread defined in Eq. (3.1) can be determined from track power measurements.

In a small local area, we assume that the amplitudes of the multipath waves are approximately constant while the phases vary as a function of receiver position and AOA of the incoming waves. This is called the *local area assumption* and is discussed in Section 4.4. If a peak on the PDP is a result of more than one multipath arriving within $2 * T_c$ of each other, then the peak undergoes small-scale fading as the receiver antenna moves along the track. The variance of the fading rate is related to the angular spread of the multipath contributing to the power peak.

The fading rate variance of the power peak as it moves along a linear track, σ_x^2, is calculated from

measurements with

$$\sigma_x^2 = E\left\{\left[\frac{dP(x)}{dx}\right]^2\right\} = \frac{1}{N}\sum_{j=1}^{N} E\left\{\left[\frac{dP(x)}{dx}\Big|_{x=x_j}\right]^2\right\}. \tag{4.1}$$

The calculation of the slope at each point x_j is discussed in Section 4.2.

The fading rate variance for a measured power peak along a track is a function of the direction of orientation of the track. If the fading rate variance along two orthogonal tracks is measured, then the mean fading rate variance for an arbitrary direction of orientation σ_S^2 is given by the average of the two track fading rate variances:

$$\sigma_S^2 = \frac{\sigma_x^2 + \sigma_y^2}{2} \tag{4.2}$$

where σ_x^2 and σ_y^2 are the two fading rate variances.

In [5], the mean fading rate variance is shown to be directly proportional to the angular spread. An additional assumption made is that the multipath power arrives in the azimuthal plane (without a significant elevation angle). This assumption is acceptable for the peer-to-peer channel since both antennas have the same height. The relationship is

$$\sigma_S^2 = k^2 P_T^2 \Lambda^2 \tag{4.3}$$

where $k = \frac{2\pi}{\lambda}$ is the wave number and P_T is the mean local area received power. The angular spread, the same as in Eq. (3.1), is given as Λ^2.

4.2 Finding the Slope of a Sampled Waveform

One of the difficulties in the measurement of the fading waveform is that we measure only a *sampled* waveform. This is a complication when we try to calculate the slope of the measured waveform. The slope of the measured power waveform is the fading rate, a very important characteristic in these measurement results. It is essential that its calculation is done accurately.

We cannot find the slope simply by calculating the difference between two samples and dividing by the sampling distance. To see why this is the case, the mathematical analysis in Sections 4.2.1 and 4.2.2 is necessary. These two sections show mathematically how to calculate the slope of the sampled waveform. This formula will be important for later stochastic analysis of the effects of errors on the angular spread. In Section 4.2.3, a simplified and efficient computer calculation method for slope calculation is presented.

4.2.1 Representation of the Sampled Waveform

We call the measured power (fading) waveform $P(x)$. This waveform is sampled at positions x_i where i is an integer. Samples are evenly spaced, each $\Delta x = \lambda/4$ from the next.

The sampling rate, $R_s = 1/\Delta x = 4/\lambda$ is equal to the Nyquist rate (twice the frequency of the highest possible frequency component in the waveform). Note that the frequency units are $1/m$. The original signal can be recreated from the samples as a sum of sinc functions:

$$P(x) = \sum_{i=-\infty}^{\infty} P(x_i) \frac{sin\left(\frac{\pi}{\Delta x}(x - x_i)\right)}{\frac{\pi}{\Delta x}(x - x_i)} \tag{4.4}$$

In practice, we do not take an infinite number of samples of the signal. Eighty samples are taken along each measurement track. In this case, Eq. (4.4) is an approximation.

In Eq. (4.4), the value of the function $P(x)$ is determined solely from the sample taken at x_i. Only one *sinc* function is non-zero at that point. However, the slope of the function $P(x)$ at point x_i is determined by all of the samples of the signal except for the one at x_i. This point is shown by derivation in the following section.

4.2.2 The First Derivative of the Sampled Signal

We're interested in the derivative of $P(x)$ taken at the point x_j.

$$\left.\frac{dP(x)}{dx}\right|_{x_j} = \sum_{i=-\infty}^{\infty} P(x_i) \left.\frac{\left(\frac{\pi}{\Delta x}\right)^2 (x - x_i) cos\left[\frac{\pi}{\Delta x}(x - x_i)\right] - \frac{\pi}{\Delta x} sin\left[\frac{\pi}{\Delta x}(x - x_i)\right]}{\left(\frac{\pi}{\Delta x}\right)^2 (x - x_i)^2}\right|_{x_j} \tag{4.5}$$

Note that $x_j - x_i = (j - i)\Delta x$. Also note that the contribution to the sum is zero when $j = i$ (The slope is zero at the peak of a sinc function). When we let $x = x_j$ the equation reduces to

$$\left.\frac{dP(x)}{dx}\right|_{x_j} = \sum_{i=-\infty, i\neq j}^{\infty} P(x_i) \frac{\frac{\pi^2}{\Delta x}(j - i) cos(\pi(j - i)) - \frac{\pi}{\Delta x} sin(\pi(j - i))}{\pi^2 (j - i)^2} \tag{4.6}$$

The $sin(\pi(j - i))$ term will always be zero. The $cos(\pi(j - i))$ term is 1 for even $j - i$ and -1 for odd $j - i$. The result is that

$$\left.\frac{dP(x)}{dx}\right|_{x_j} = \sum_{i=-\infty, i\neq j}^{\infty} P(x_i) \frac{(-1)^{j-i}}{\Delta x (j - i)} \tag{4.7}$$

For computational efficiency, we can move the Δx and the $(-1)^j$ outside of the summation:

$$\left.\frac{dP(x)}{dx}\right|_{x_j} = \frac{(-1)^j}{\Delta x} \sum_{i=-\infty, i\neq j}^{\infty} P(x_i) \frac{((-1)^i}{j - i} \tag{4.8}$$

This form shows that the slope at the point x_j depends on all samples $P(x_i)$ except for $i = j$. However, the contribution of each sample decreases with increasing $|j - i|$. Nevertheless, the calculation of the slope will require a good deal of computational complexity, especially if the slope needs to be calculated for all j.

For example, if we take 7 samples of a signal and calculate the slope at x_4, we find it using the formula:

$$\left.\frac{dP(x)}{dx}\right|_{x_4} = \frac{1}{\Delta x}\left[\frac{P(x_1)}{-3} + \frac{P(x_2)}{2} + \frac{P(x_3)}{-1} + \frac{P(x_5)}{1} + \frac{P(x_6)}{-2} + \frac{P(x_7)}{3}\right] \tag{4.9}$$

It is apparent that the sum is centered on sample x_4. We can rewrite the signal derivative as:

$$\left.\frac{dP(x)}{dx}\right|_{x_j} = \frac{1}{\Delta x}\sum_{i=1}^{\infty}\frac{\left[P(x_{j+i}) - P(x_{j-i})\right](-1)^{i+1}}{i} \tag{4.10}$$

Using Eq. (4.10) requires the summation of $N/2$ terms. Calculating the derivative at every point on the waveform is an $O(N^2)$ calculation.

4.2.3 Calculating the Slope by the FFT

The process of calculating the slope along the entire waveform would be a computationally intensive task using Eq. (4.10). An alternative method is presented in this section. The slope is calculated at each point using the following steps:

1. Zero-pad the signal. The original signal has 80 samples. This algorithm will be most efficient using a number of samples that is a power of two. Thus pad the signal to a length 128.
2. FFT the signal and insert zeros at high frequencies to pad the frequency-domain signal to a length of $N = 128R$ where $R = 2^x$ and x is an integer.
3. IFFT the result. The resulting signal is sub-sampled at rate R. Save only the first $80R$ samples.
4. Calculate the slope at each point simply by taking the difference of neighboring samples.

Fig. (4.1) shows the results of the super-sampling for $R = 8$. The measured linear power is power is divided by the mean of the power waveform to show clearly how high and low the signal goes compared to its mean. The measurement track in this figure happens to be one of two tracks for which the last few measurement points were lost due to computer error. Although the length of the track is 63, and not 80, the process is the same.

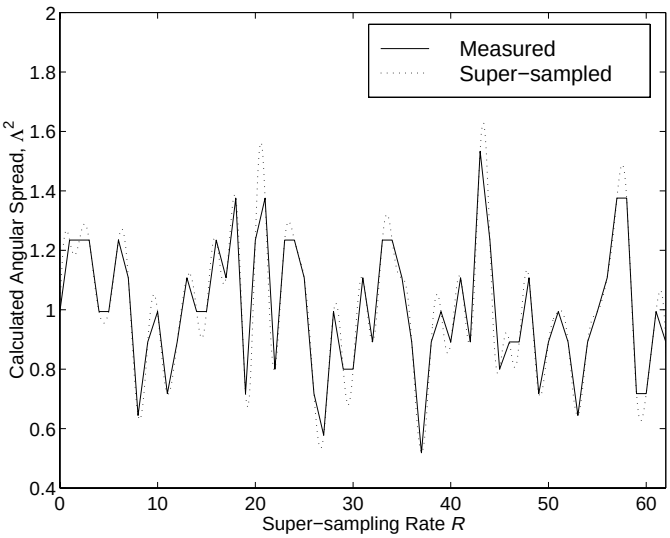

Figure 4.1: The measured power along the track is super-sampled before calculating the slope at the sampling points.

Note that the slope at the sampling points is usually higher in the super-sampled waveform than in the original measured waveform in Fig. (4.1). If the slope had been calculated from the measured waveform without super-sampling, in general, the result would be too low. Since

$$\Lambda^2 \propto \left[\frac{dP}{dx}\right]^2 \tag{4.11}$$

super-sampling increases the angular spread to its correct value. This increase is shown by calculating the angular spread for the waveform in Fig. (4.1) across a range of R. The results in Fig. (4.2.3) show that the angular spread reaches its asymptotic value quickly. As R becomes high ($R \geq 8$) the error becomes very low.

Because of its simplicity and accuracy, this super-sampling method is used for the calculation of the slope of the measured waveforms for the remainder of this thesis. A value of $R = 8$ is used.

4.3 Effect of Transient Error in Measurements

One of the major difficulties in the measurement of small-scale fading is the effect of the errors caused by transient objects in the channel. Transient error, as discussed in Section 2.6, is caused by moving objects in the channel such as cars, tree branches and leaves, and pedestrians. These transients can either block a multipath component or cause an additional multipath for a short

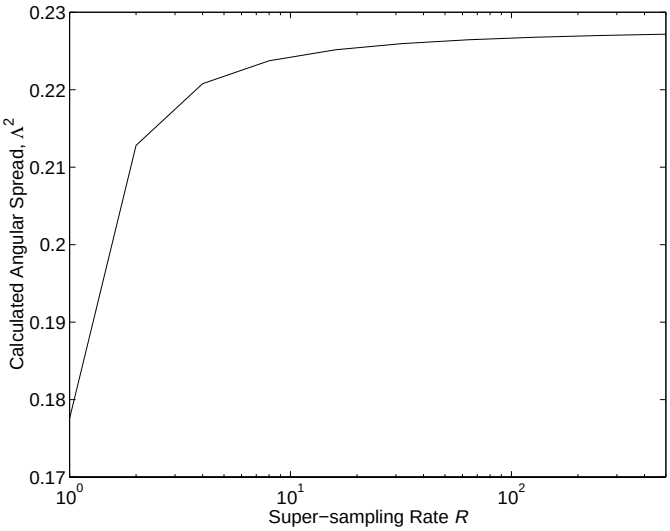

Figure 4.2: The calculated angular spread for the power waveform of Fig. (4.1) as a function of the super-sampling rate R. The asymptotic value is reached for $R \geq 8$.

period of time. Although we attempt to reduce the effect of transient error by averaging 10 PDP waveforms at each position along the track, the error still has an effect.

The transient error in the PDP measurements causes angular spread error. This section will show the following significant results:

- Calculated angular spread from measurements is a biased estimate of the actual angular spread.
- The measured angular spread is the sum of the actual angular spread and an additive term due to the random error.
- The expected value of the additive noise term can be calculated using only the variance of the transient error and the mean measured power. The error variance could be determined from measurement experiment.
- An unbiased estimate of the angular spread can be made by subtracting out the additive error term.

A measurement experiment to determine the error variance was unfortunately not conducted for this thesis since this analysis was not completed at the time of the measurement campaign. However, this analysis will be very useful for similar measurement campaigns in the future.

4.3.1 Assumption of i.i.d. Random Transient Error

If the measured power at time delay τ at track position x_i is called $P(\tau, x_i)$, then

$$P(\tau, x_i) = P_{des}(\tau, x_i) + n(\tau, x_i) \tag{4.12}$$

where the desired fading waveform power is $P_{des}(\tau, x_i)$ and the error in the power measurement is $n(\tau, x_i)$.

In this thesis the assumption is made that $n(\tau, x_i)$ is a random variable independent and identically distributed (i.i.d.) with respect to the samples x_i. This assumption is due to the fast motion of the scatterers and the slow speed of the measurements. Each measurement along the track takes about 7-10 seconds total for antenna positioning, PDP measurement, and computer recording. Moving automobiles, pedestrians, leaves and branches that cause or obstruct multipath in one measurement are likely to be in a different position by the time of the next measurement. This is not always the case – cars that drive past the receiver, park for a minute on the side of the street, then continue, may cause a reappearing multipath during the time they are parked. However, for most of the noise, a good engineering model for the error is as an i.i.d. random variable.

4.3.2 Expected Value and Variance of the First Derivative

If the error samples, $n(x_i)$, are i.i.d. with mean μ_n and variance σ_n^2 then we can calculate the expected value and variance of the first derivative of $n(x)$. The expected value is

$$E\left[\left.\frac{dn}{dx}\right|_{x_j}\right] = \frac{1}{\Delta x}\sum_{i=1}^{\infty}\left(E\left[n(x_{j+i})\right] - E\left[n(x_{j-i})\right]\right)\frac{(-1)^{i+1}}{i}. \tag{4.13}$$

Since the expected value of each sample is identical, the difference term equals zero. Thus the expected value of the first derivative is zero.

The variance of the first derivative is more complicated:

$$\begin{aligned} E\left[\left.\frac{dn(x)}{dx}\right|_{x_j}^2\right] &= \frac{1}{\Delta x^2}E\left\{\sum_{i=1}^{\infty}\left[n(x_{j+i}) - n(x_{j-i})\right]\frac{(-1)^{i+1}}{i}\sum_{k=1}^{\infty}\left[n(x_{j+k}) - n(x_{j-k})\right]\frac{(-1)^{k+1}}{k}\right\} \\ E\left[\left.\frac{dn(x)}{dx}\right|_{x_j}^2\right] &= \frac{1}{\Delta x^2}\sum_{i=1}^{\infty}\sum_{k=1}^{\infty}\frac{(-1)^{i+k}}{ik}E\left\{\left[n(x_{j+i}) - n(x_{j-i})\right]\left[n(x_{j+k}) - n(x_{j-k})\right]\right\} \end{aligned} \tag{4.14}$$

For $i \neq j$ the expected value term will be zero. Thus

$$E\left[\left.\frac{dn(x)}{dx}\right|_{x_j}^2\right] = \frac{1}{\Delta x^2}\sum_{i=1}^{\infty}\frac{1}{i^2}E\left\{\left[n(x_{j+i}) - n(x_{j-i})\right]^2\right\}$$

$$E\left[\left.\frac{dn(x)}{dx}\right|_{x_j}^2\right] = \frac{1}{\Delta x^2}\sum_{i=1}^{\infty}\frac{1}{i^2}\left\{E\left[n^2(x_{j+i})\right] - 2\mu_n(\tau)^2 + E\left[n^2(x_{j-i})\right]\right\}$$
$$E\left[\left.\frac{dn(x)}{dx}\right|_{x_j}^2\right] = \frac{1}{\Delta x^2}2\sigma_n^2\sum_{i=1}^{\infty}\frac{1}{i^2} \tag{4.15}$$

The infinite sum term is given in [26] to be

$$\sum_{i=1}^{\infty}\frac{1}{i^2} = \frac{\pi^2}{6}. \tag{4.16}$$

Thus the variance formula is

$$E\left[\left.\frac{dn(x)}{dx}\right|_{x_j}^2\right] = \frac{\pi^2}{3}\frac{\sigma_n^2}{\Delta x^2}. \tag{4.17}$$

4.3.3 The Angular Spread of Measured Signals

Consider the case where a desired signal and transient error both contribute to the measured power, as described in Eq. (4.12). Assume τ is a constant and calculate the mean and variance of the first derivative of $P(x)$.

The mean is given by

$$E\left[\left.\frac{dP(x)}{dx}\right|_{x_j}\right] = \frac{1}{\Delta x}\sum_{i=1}^{\infty}E\left[P_{des}(x_{j+i}) + n(x_{j+i}) - P_{des}(x_{j-i}) - n(x_{j-i})\right]\frac{(-1)^{i+1}}{i} \tag{4.18}$$

The expected values of the like terms cancel and the mean slope is zero.

The variance is given by

$$\begin{aligned}
E\left[\left.\frac{dP(x)}{dx}\right|_{x_j}^2\right] &= \frac{1}{\Delta x^2}E\left\{\sum_{i=1}^{\infty}\left[P_{des}(x_{j+i}) + n(x_{j+i}) - P_{des}(x_{j-i}) - n(x_{j-i})\right]\frac{(-1)^{i+1}}{i}\right. \\
&\quad \left.\sum_{k=1}^{\infty}\left[P_{des}(x_{j+k}) + n(x_{j+k}) - P_{des}(x_{j-k}) - n(x_{j-k})\right]\frac{(-1)^{k+1}}{k}\right\} \\
&= \frac{1}{\Delta x^2}\sum_{i=1}^{\infty}\sum_{k=1}^{\infty}\frac{(-1)^{i+k}}{ik}E\left[\left\{\left[P_{des}(x_{j+i}) - P_{des}(x_{j-i})\right] + \left[n(x_{j+i}) - n(x_{j-i})\right]\right\}\right. \\
&\quad \left.\left\{\left[P_{des}(x_{j+k}) - P_{des}(x_{j-k})\right] + \left[n(x_{j+k}) - n(x_{j-k})\right]\right\}\right] \\
&= E_1 + E_2 + E_3
\end{aligned} \tag{4.19}$$

where the cross-multiplication has been split into three terms. The first term includes the products of the $P_{des}(x)$ and is given by

$$E_1 = \frac{1}{\Delta x^2}\sum_{i=1}^{\infty}\sum_{k=1}^{\infty}\frac{(-1)^{i+k}}{ik}E\left\{\left[P_{des}(x_{j+i}) - P_{des}(x_{j-i})\right]\left[P_{des}(x_{j+k}) - P_{des}(x_{j-k})\right]\right\} \tag{4.20}$$

which is the definition of the fading rate variance of the desired signal in the x-direction, $\sigma^2_{des,x}$. The second term includes all the products $P_{des}(x)n(x)$ and is given by

$$\begin{aligned} E_2 &= \frac{1}{\Delta x^2}\sum_{i=1}^{\infty}\sum_{k=1}^{\infty}\frac{(-1)^{i+k}}{ik}E\left\{P_{des}(x_{j+i})n(x_{j+k}) - P_{des}(x_{j+i})n(x_{j-k})\right. \\ &\quad -P_{des}(x_{j-i})n(x_{j+k}) + P_{des}(x_{j-i})n(x_{j-k}) + P_{des}(x_{j+k})n(x_{j+i}) \\ &\quad \left. -P_{des}(x_{j+k})n(x_{j-i}) - P_{des}(x_{j-k})n(x_{j+i}) + P_{des}(x_{j-k})n(x_{j-i})\right\}. \end{aligned} \tag{4.21}$$

Since $P_{des}(x)$ and $n(x)$ are independent, the expected value of each product is equal to the product of the expected values. Since they are from identical distributions, the means of all P_{des} are identical, and the means of all $n(x)$ are identical. The terms will cancel and $E_2 = 0$.

The final term, E_3, is given by

$$E_3 = \frac{1}{\Delta x^2}\sum_{i=1}^{\infty}\sum_{k=1}^{\infty}\frac{(-1)^{i+k}}{ik}E\left\{\left[n(x_{j+i}) - n(x_{j-i})\right]\left[n(x_{j+k}) - n(x_{j-k})\right]\right\} \tag{4.22}$$

For $i \neq j$ the expected value term will be zero. Thus

$$\begin{aligned} E_3 &= \frac{1}{\Delta x^2}\sum_{i=1}^{\infty}\frac{1}{i^2}E\left\{\left[n(x_{j+i}) - n(x_{j-i})\right]^2\right\} \\ E_3 &= \frac{1}{\Delta x^2}\sum_{i=1}^{\infty}\frac{1}{i^2}\left\{E\left[n^2(x_{j+i})\right] - 2\mu_n(\tau)^2 + E\left[n^2(x_{j-i})\right]\right\} \\ E_3 &= \frac{1}{\Delta x^2}2\sigma_n^2\sum_{i=1}^{\infty}\frac{1}{i^2} \end{aligned} \tag{4.23}$$

The infinite sum term is the same as in Eq. (4.16). Thus the variance formula is

$$E_3 = \frac{\pi^2}{3}\frac{\sigma_n^2}{\Delta x^2}. \tag{4.24}$$

The fading rate variance in the presence of transient error is the sum of E_1, E_2, and E_3, so

$$E\left[\left.\frac{dP(x)}{dx}\right|_{x_j}^2\right] = \sigma^2_{des,x} + \frac{\pi^2}{3}\frac{\sigma_n^2}{\Delta x^2}. \tag{4.25}$$

This analysis is for the track measurements along the x-direction. It is clear that this is also the expected value of the fading rate variance of the orthogonal track, also. Thus the expected value of the measured spatial average fading rate variance, σ_S^2, by Eq. (4.2), is

$$E\left[\sigma_S^2\right] = \sigma^2_{des,S} + \frac{\pi^2}{3}\frac{\sigma_n^2}{\Delta x^2}. \tag{4.26}$$

Using this value in Eq. (4.3) the measured angular spread in the local area is

$$\Lambda^2 = \frac{1}{k^2 P_T^2}\left[\sigma_{des,S}^2 + \frac{\pi^2}{3}\frac{\sigma_n^2}{\Delta x^2}\right] \tag{4.27}$$

where in these measurements samples are taken each $\Delta x = \lambda/4$ and $k = 2\pi/\lambda$. The term P_T is mean of the measured waveform, $P_T = \mu_n + \overline{P_{des}}$. Thus Eq. (4.27) reduces and the measured angular spread is

$$\Lambda^2 = \Lambda_{des}^2\left[\frac{P_T - \mu_n}{P_T}\right]^2 + \frac{4}{3}\frac{\sigma_n^2}{P_T^2}. \tag{4.28}$$

Notice that the transient error can be both negative and positive. Negative transient error power means can mean that the transient object caused a multipath that destructively interfered with a desired multipath thereby causing a lower measured power than if the transient object had not been there. Or, it could mean that the transient blocked the path of a desired multipath component. Positive transient error power occurs when a transient object causes a multipath that adds constructively to the desired multipath and causes the measured power to be higher than it would have been if the transient object had not been there.

There is no reason to believe that the transient error is more likely to be positive than negative. In fact, a good engineering assumption would be to consider the error to be a zero-mean random variable. This assumption should be verified by measurements. The additional assumption about the transient error simplifies Eq. (4.28) to

$$\Lambda^2 = \Lambda_{des}^2 + \frac{4}{3}\frac{\sigma_n^2}{P_T^2}. \tag{4.29}$$

This result shows that the calculated angular spread from the measurements, Λ^2, is a biased estimate of the actual angular spread, Λ_{des}^2. An unbiased estimate of the actual angular spread of the channel can be calculated by subtracting out the error term:

$$\Lambda_{des}^2 = \Lambda^2 - \frac{4}{3}\frac{\sigma_n^2}{P_T^2}. \tag{4.30}$$

where Λ^2 and P_T are both determined from the track measurements.

The variance of the transient error can be found in the same manner as PDP track measurements but by leaving the antenna stationary. The important part would be to keep the timing the same - PDP measurements spaced 7-10 seconds apart in time just as during the track measurements. These stationary PDP measurements could be used to calculate the variance of the error signal, σ_n^2, for all time delays. However, σ_n^2 is likely to be different for each different link, and this measurement must be repeated at each receiver location. The measurement campaign reported in this thesis unfortunately did not conduct these stationary PDP measurements.

4.3.4 Example of Log-Normal Transient Error

As an example, consider a single multipath component received in the PDP at time delay τ. Assume that no other multipath arrive at this time delay, and the measurement system resolves the single path. Thus the actual angular spread, $\Lambda^2_{des} = 0$. In this example, the measured power of the multipath component, due to errors, is a log-normally i.i.d. random variable. Assume that the mean of this random variable is the desired signal power.

It is necessary to use the linearized PDF of the log-normal variable to calculate the mean and variance. If μ_{dB} and σ_{dB} are the mean and standard deviation of the normally-distributed dB power variable P_{dB}, then the mean and variance of the linearized measured power P are given by

$$\mu_P = \mu_{dB} C \tag{4.31}$$

$$\sigma_P^2 = \mu_{dB}^2 \left(C^4 - C^2 \right) \tag{4.32}$$

where C is given by

$$C = \exp\left[\frac{1}{2} \left(\frac{\ln 10}{10} \sigma_{dB} \right)^2 \right]. \tag{4.33}$$

The error in the measured signal at sample i is

$$n(x_i) = P(x_i) - \mu_P \tag{4.34}$$

The variance of n is then just σ_P^2. Thus the measured angular spread is given by

$$\Lambda^2 = \frac{4}{3} \left[\exp\left(\sigma_{dB}^2 \frac{\ln^2 10}{100} \right) - 1 \right] \tag{4.35}$$

which is shown graphically in Fig. (4.3). It shows that temporal variances in the power level of multipath components can lead to significant angular spread errors.

4.4 Local Area Assumption

An assumption that is difficult to verify is the local area assumption. That is, we assumed that the signal strengths of the multipath components received at the receiver were approximately constant within a 20λ local area. As discussed earlier, measurement error can occur due to channel transients that change the characteristics of the arriving multipath over time. But, ignoring the transient errors, what if the signal levels of the multipath components change over position within the local area? There are two important questions raised:

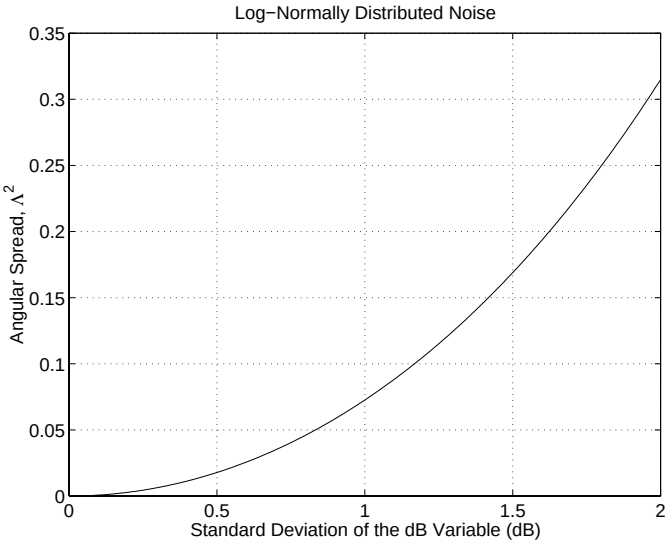

Figure 4.3: The Λ^2 that would be calculated on a single multipath component if its measured power is an i.i.d. log-normal random variable. The x-axis shows the standard deviation of the dB random variable.

1. What effect does the change in signal levels within the local area have on the calculated angular spread?

2. How can the local area assumption be verified or contradicted?

As the following sections will discuss, the second question remains mostly unanswered.

4.4.1 Effects of Change in Multipath Signal Levels

Recall that the angular spread is proportional to the mean-square slope of the received power as a function of distance. Thus, rapidly varying multipath signal levels within the local area will strongly affect the calculated angular spread, while slow changes will have a small effect.

If the changing multipath signal level from sample to sample is described well as a random i.i.d. variable, then their effect on the angular spread will be the same as the effect of transient error as described in Section 4.3. If multipath signal levels are random variables but positively correlated with their neighboring samples, then the fading rate will be lower, on average. The effect on the angular spread will be smaller than predicted in Section 4.3. In the limiting case, if the correlation between samples is very high, the measured angular spread will not be affected by the change in multipath signal levels.

For example, consider a single strong multipath component that is received in only half of the linear track. Let's say that the other half of the local area is completely shadowed by the edge of a building. What is the calculated angular spread? The fading rate between the samples straddling the shadow boundary is likely to be very high. The fading rates measured on the 'lit' side of the track would have led to an accurate calculation of the fading rate variance if only that half of the track data had been used, σ^2_{lit}. In the same manner, the fading rates measured on the 'shadowed' side of the track would have led to an accurate calculation of the fading rate variance if only *that* half of the track data had been used, $\sigma^2_{shadowed}$. If calculate the mean squared fading rate for the whole track, it will be

$$\sigma_x^2 \approx \frac{\sigma^2_{lit} + \sigma^2_{shadowed}}{2} + \epsilon \tag{4.36}$$

where ϵ is the error due to the shadow boundary, approximately the squared fading at the shadow boundary divided by N, the number of samples. The equation is approximate since it does not account for the effect of calculating the slope using the supersampling method (Section 4.2.3). Nevertheless, it is apparent that the calculated fading rate variance is only slightly higher than the average of the two fading rates.

Although the local area assumption does not hold in this example, the difference is not important to the communication system engineer. Such a person requires a sample of the angle dispersion characteristics of the channel in a given environment, and in this example he would have one.

4.4.2 Assumption Validation

In cases like the example just provided, a test could be designed to validate (or invalidate) the local area assumption. A simple statistical test would compare the mean power of the first several samples of the fading waveform with the mean power of the last several samples. If they are too far apart, the test would say with a certain confidence level that multipath components had changed signal strengths between the beginning and the end of the track.

Although this test would identify cases where the local area assumption had been violated, they would tend to be cases in which the multipath signal levels were strongly positively correlated with receiver position. And these are the cases when the engineer does not mind the violation of the assumption! This test would not be likely to identify the case in which the variations had low or no correlation, where the errors in the calculated angular spread would be high.

If the calculated Λ^2 is greater than 1.0, we might suspect that the multipath signal levels are varying strongly over position. However, high Λ^2 may also be due to high transient errors. We

cannot isolate the two different causes.

Several fading waveforms are shown with the measurement results in Section 6.3.1.

4.5 Conclusion

This chapter details how the measured PDPs are used to determine the fading rate variance and the angular spread. However, the measurements are often affected by random errors caused by transients in the channel. This error can cause significant error in the calculated angular spread. The useful result of the analysis in this chapter is that the mean angular spread error can be determined by measurement experiment and then subtracted out. This experiment determines the error variance by taking stationary PDP measurements at each receiver location. Unfortunately, these stationary PDP measurements were not conducted during this measurement campaign. The benefit of this analysis will be for future measurement campaigns.

This chapter also considers the effects and the detection of violations in the local area assumption. The effects are not severe unless the multipath signal levels change rapidly throughout the local area. In this case, the measured angular spread would be very high, but it would be difficult to say with any certainty that the cause was the violation of the local area assumption rather than high transient error or truly high angular spread.

Chapter 5

Site Descriptions

The measurements were conducted at eight different measurement sites in and around the Virginia Tech campus. Several transmitter - receiver links were measured at each site. Each site was chosen to represent a type of environment. Four of the sites were rural environments, where few buildings affected the channel. These rural environments typically involved open fields with hilly terrains spotted with trees and vegetation. One of these rural locations was a forest area with dense trees and vegetation. The other rural sites were more sparsely populated by vegetation and mostly open.

Four of the sites were semi-urban. Virginia Tech's campus is not in a city – however, the campus has areas of tall and densely arranged buildings. The most dense areas were selected for measurements. The first four measurement site descriptions that follow in Sections 5.1 to 5.4 are the semi-urban sites. The four site descriptions given in Sections 5.5 through 5.8 are rural areas.

Color pictures of the transmitter and receiver locations, their surrounding environments, and maps of each measurement site are provided in Appendix A. Keeping these photos and maps at hand while reading this section will help bring the measurement campaign to life and give the reader a sense of the environments in which the measurements were conducted.

5.1 Semi-Urban Area: Old Turner Street

Old Turner St. is a narrow street lined with buildings on both sides. The buildings vary in height from one story to 5 stories. Also, the width of the street varies from end to end, because some buildings, such as the Virginia Tech power plant, are set very close to the street, and others are set further back. Full-grown deciduous trees line both sides of the street. The canopies of these trees

begin above 3 meters in height and are as tall as 10 m. Cars are parked on both sides of the street in front of Randolph Hall, near the transmitter. The parked cars and trucks sometimes obstructed the line-of-sight path at receiver location 1. However, the line-of-sights at the other locations were not obstructed by parked cars. Most measurements at this site were taken as moving vehicles drove past at about 40 km/hr. Thus there were periodic obstructions and scattering from moving cars.

Measurements were carried out at four receiver locations in order to provide a decade of transmitter-receiver separation distances, from 40 m to 400 m, as illustrated in the site map in Fig. (A.1.1). The first receiver was placed 39.5 m from the transmitter on a sidewalk. The antennas were higher than the majority of cars. Thus the parked cars did not usually obstruct the LOS. However, their close proximity surely played an important part in the behavior of the communications channel. The terrain was mostly flat and the receiver was 60 cm higher than the transmitter at this location.

Receiver location 2 had the same height difference. The path length was 76 m. This location was close to the center of the street, and as a result, parked cars did not obstruct the LOS. However, this was a busy area with cars pulling in and out of the parking lot thereby resulting in a variable channel.

Receiver location 3 was very similar to the second but further away. It was an LOS link with a path length of 175 m. It is located at an intersection with tall buildings (3-5 stories) close to the street.

Turner St is predominantly flat. The end of the street, near receiver location 4, does experience some elevation change, but not enough to block the line-of-sight path.

The path length to receiver location 4 was 396 m, the largest of the four at this site. The hilly terrain caused partial blocking of the line-of-sight path. The receiver was located near both tall campus buildings and smaller houses.

5.2 Semi-Urban Area: Hutcheson Hall

The Hutcheson Hall site has a street that cuts behind several academic buildings, as shown in the site map in Fig. (A.2.1). On the north side of the street, there is a parking lot and several buildings with widely varying height. Slusher Hall, the tallest of the buildings, is an 12-story tower. Hutcheson Hall is a 5-story building, and Agnew Hall and Seitz Hall both have varying heights, ranging between 1 and 3 stories. Receiver locations 13, 14, and 15 were all located here.

On the south side of the street there is a steep, grassy hill which rises 10m within a horizontal

distance of 30m. On top of this hill are several more buildings, including Fralin Hall, a three-story building. A elevated walkway bridges the road and connects the ground level near Fralin and the rooftop of Seitz. This walkway obstructed the link at receiver location 15. Measurements were conducted at this site on a Sunday, so traffic was very light. Also, the parking lot was nearly empty on this day. As shown in Fig. (A.2.1), the transmitter was placed on the side of the street at the edge of the parking lot.

The link at receiver location 13 is obstructed by the terrain. At this location, the receiver is placed on top of the hill on the south side of the street and the antenna is 9 m higher than the transmitter antenna. The crest of the hill obstructs the line-of-sight. The separation distance was 127 m.

Receiver location 14 is just 4 m lower than the transmitter, on the north side of the street 10 m away from the street. It is 5 m in front of a one-story section of Agnew Hall. The tx-rx separation is short, only 50 m. We expect to see reflections from surrounding buildings and scattering from the hill on the south side of the street.

Receiver location 15 is on another hill at the far end of the street, 145 m away. The elevation at receiver location 15 is only 1m higher than the transmitter elevation, however, the road crests down and then back up in between the transmitter and receiver. The hill does not obstruct the LOS, but the pedestrian bridge mentioned earlier does obstruct the line-of-sight.

This is an important site for the ray-tracing verification effort at MPRG. This is a site where 3-D ray-tracing will prove useful. 2-D ray-tracing would not account for the obstruction by the bridge or the reflections and diffractions of the terrain. The MPRG ray-tracer should predict the channel characteristics of sites such as this one better than currently possible with any other technique. The results from this site will help verify this claim.

5.3 Semi-Urban Area: Derring Hall

At the Derring Hall site, the transmitter was placed on one side of Derring Hall and the receivers were placed on the other. The receiver locations measured (receiver locations 18 and 19) were chosen as examples of links where the main propagation mechanism is diffraction over and around buildings. Fig. (A.3.1) illustrates the map for this site.

The transmitter was located in the parking lot on the north side of Derring Hall. Derring Hall is a four-story brick and cement building. On the south side of the building there is another parking lot and a grassy courtyard area. Receiver location 18 was in the courtyard on the south side of Derring

Hall. The elevation of the south side of the building is higher, and thus the receiver was 3 m higher than the transmitter. The straight-line distance between the transmitter and receiver was 195 m. This location was only about 5 m from another building further south, Robeson Hall. We expect that Robeson Hall will serve as a strong reflector. Robeson Hall is a cement and limestone building three stories in height, but due to its higher base than Derring, the rooftop is approximately at the same height.

Receiver location 19 was on the south side of Robeson Hall. At this location, the signal should undergo double rooftop diffraction between the transmitter and receiver. The receiver was surrounded by tall deciduous trees at this location.

A third site was planned for the south side of the next building, Williams Hall. This site would have required a diffraction over three buildings to propagate from transmitter to receiver, however, and the received signal was not strong enough to measure.

The measurements at this site should help characterize urban non-LOS environments for the HMT project. Mobile terminals may be separated by several streets where the signal must undergo multiple diffractions and reflections to travel from the transmitter to the receiver. These two links are examples of that situation.

5.4 Semi-Urban Area: Drillfield

The drillfield is like an open park in the center of an urban area. The area is open with trees and grass and some paved walkways. However, the drillfield is surrounded by buildings, as seen in Fig. (A.4.1). We expect to see a large number of reflections from all directions to the receiver due to the surrounding buildings. The drillfield is oval-shaped. A road, Drillfield Drive, circles around the perimeter. Cars are parked on both sides of the road, and the buildings lie on the outside of the road.

The transmitter was located at one end of the oval. Receiver location 20 was located at the opposite end of the oval, 308 m in distance and 6 m lower in elevation than the transmitter. The transmitter and receiver locations are shown in Fig. (A.4.1). The link had an unobstructed line-of-sight.

Receiver location 21 was not located on the drillfield. The receiver was moved to the far side of West Campus Drive in another park. This park, unlike the drillfield, was less open due to many large, deciduous trees. Nevertheless, the receiver location was chosen to provide an LOS link. The tx-rx separation was 557 m, and the receiver was 9 m lower in elevation compared to the transmitter.

Receiver location 22 was located near the center of the Drillfield. The path length here was 103 m, the shortest of the three links, with a change of elevation between transmitter and receiver of 3 m.

This location provides a juxtaposition of urban and rural elements in the same site. The oval placement of the surrounding reflectors provides an environment in which the arriving multipath should arrive from all angles, causing a high angular spread.

5.5 Rural Area: Southgate Drive

The transmitter was placed on the south side of Southgate Drive near the Dairy Farm Barn. The map in Fig. (A.5.1) and the pictures in Section (A.5) show the extremely rural nature of this area. Two cow fields and several corn fields are located nearby. The area where the transmitter antenna is placed is elevated by about 3m relative to Southgate Drive. This varying terrain in the vicinity of the transmitter is shown by the contour lines in the map in Fig. (A.5.1).

Three receiver locations (5, 6, and 7) were chosen along the south side of Southgate Drive. Receiver location 5 was LOS and just inside the driveway of the Dairy Farm, at a separation distance of 101 m. The driveway entrance is east of the transmitter location on Southgate Drive. The elevation of the receiver was 6 m lower than that of the transmitter.

Receiver location 6 was further east on Southgate Drive, in the parking lot of the Visitor Information Center. This receiver location was 211 m away from the transmitter, and 9 m lower. The line-of-sight at this link was blocked by the leaves of three small deciduous trees.

Receiver location 7 was 157 m west of the transmitter on Southgate Drive. There is a paved pull-off on the side of the road at this location which allowed us to keep the measurement equipment on a flat surface. The receiver antenna is 6 m lower in elevation than the transmitter antenna.

The Southgate Drive area was chosen specifically to allow a drive test of the HMT receiver at a speed of 65 km/hr. Southgate Drive has the highest speed limit on campus and does not have pedestrian traffic or stoplights. The driver would start at the Visitor Information Center parking lot, turn left onto Southgate drive, drive up Southgate while testing the HMT, make a U-turn at the stoplight and return. The three receiver locations measured on Southgate Drive would be in this path.

5.6 Rural Area: The Beef Cattle Farm

This site is an agricultural area, with horse fields, cow fields, and several hay fields. The area is hilly, and a stream runs through the valley. A residential area is beyond the edge of the fields. Several barns are in the area, providing some reflectors in the radio channel.

As shown in Fig. (A.5.1), the transmitter was placed on a path between two hay fields 35 m from the stream. The transmitter is relatively low in the hilly environment. The fields are separated either by barbed-wire fencing or wooden fencing about 1 m high.

Receiver location 8 is across the hay field, 332 m away. The elevation of the receiver antenna is only 1 m higher than the transmitter antenna. However, the small elevation difference is misleading due to the presence of a hill in between the transmitter and receiver. The line-of-sight of this link is obstructed by this hill.

Receiver location 9 is diagonally across part of the same hay field, across a stream and part of a neighboring cow field. This LOS link has a separation distance of 394 m. The receiver antenna height is 6 m higher than the transmitter antenna height. There is a valley in between the transmitter and receiver.

Receiver location 10 is the furthest from the transmitter. The link at this link is obstructed by several trees in between the transmitter and receiver. The path length is 454 m, and the elevation at the receiver antenna is 2 m higher than at the transmitter antenna.

These three locations study line-of-sight and obstructed environments in which the HMT would be expected to operate in rural conditions.

5.7 Rural Area: Forest

Measurements were made in an undeveloped forested area at the edge of campus behind the soccer field and Lane Stadium, as seen in Fig. (A.7.1). *This location was studied to see what channel characteristics should be expected in a forested battlefield in both flat and hilly areas.* The area is isolated from buildings, except for the stadium, which is about 50 m from the location of the closest measurement. In such a densely forested area the stadium should not affect the propagation channel.

The location we chose to conduct measurements is a good example of dense forest. There are tall deciduous trees as well as a tangled underbrush. The ground is not clear as fallen branches

and trees litter parts and leaves cover the remainder. The photos in Figs. (A.7.2) through (A.7.6) provide a good idea of the type and density of vegetation.

Receiver location 11 is chosen at almost the same elevation as the transmitter to study the effects of dense vegetation in a flat environment. Many branches and leaves obstruct the LOS. The first link is at a tx-rx separation distance of 49 m.

As shown in Fig. (A.7.1), receiver location 12 is at a much lower elevation than the transmitter. This link was severely attenuated due both to the dense vegetation and the shadowing from the crest of the hill. The path length of this link is 151 m.

It was windy during these measurements. The wind resulted a rapidly changing channel. As trees swayed and leaves moved in the breeze, the scatterers and obstructions led to dramatically varying channel impulse responses.

5.8 Rural Area: Golf Course and Cage

The *Cage* is a vast blacktop parking lot in the agricultural side of campus. It is nicknamed the Cage because of the tall barbed-wire fencing that surrounds it. Receiver locations 16 and 17 are in the Cage. The Virginia Tech Golf Course, where the transmitter was located, is a hilly, open, and lightly wooded environment. It is a good approximation of a rural area. In addition there are no buildings around the golf course or in between it and the Cage. Further, it is surrounded by farms. The golf course and the Cage are on opposite banks of a creek, and both slope downward to the creek. By choosing transmitter and receiver locations far removed from the creek, we have achieved two very long distance links without obstructions from buildings or terrain. Only a few trees obstruct these two links. The map in Fig. (A.8.1) shows the terrain, transmitter and receiver locations.

Receiver location 16 was the furthest from the transmitter, 1294 m away. It is located in the back, highest end of the Cage. The link's line-of-sight was obstructed by trees near to the transmitter, but there were virtually no scatterers near the receiver - the parking lot was almost completely empty.

Receiver location 17 was closer to the transmitter with a path length of 1136 m. The elevation at the receiver antenna was 16 m lower than the transmitter antenna. The line-of-sight path at this location was obstructed by more trees than the link to receiver location 17. Intuitively we might have expected that the shorter link would receive more power. But because the link at the smaller

transmitter-receiver separation experienced more severe tree attenuation, the measured path loss was almost the same as the longer link.

Chapter 6

Measurement Results and Discussion

This chapter presents the results of the measurement campaign conducted at Virginia Tech. The quantity of data - over 3500 measured PDPs - makes it impossible to show all measured data in this report. In this chapter, the processed results are presented. These results include: spatial average PDPs, fading rate and angular spread, narrowband path loss, path loss exponent, mean delay, RMS delay spread, and timing jitter. The numerical values of the results for each of the 22 links are presented in tabular form for quick reference. The calculation details and a discussion of results is contained in the following sections.

6.1 Summary Results Table

Several parameters are given in the Table 6.1. The table is ordered by link number. The site name and environment type is also listed for convenience. Each link is classified as line-of-sight (LOS) or obstructed (OBS). In addition, if the link is obstructed, a description of the obstruction is given in the column labeled *OBS. Type*. The transmitter-receiver separation distance is listed as d.

The first three measurement results describe the spatial average PDP. The mean delays of the spatial average PDPs, denoted $\bar{\tau}$ in this table, is described in Section 6.5. The RMS delay spread of the spatial average PDPs, $\bar{\sigma_\tau}$, also listed here, is discussed in Section 6.6. The narrowband path loss is calculated from the spatial average PDP in Section 6.4 and listed in the table as PL.

The remaining measurement results are calculated directly using all 160 PDPs measured at each local area receiver location. The timing jitter, detailed in Section 6.5.1, is listed as J_p. The maximum and minimum RMS delay spread among the 160 PDPs measured at a location are listed

under min/max[σ_τ]. Finally, the calculated angular spread for the first arriving peak in the PDP is given as Λ^2 and discussed in Section 6.3. Asterisks ($*$) indicate where low dynamic range of individual PDPs precluded accurate calculation of mean delay and RMS delay spread. Although some statistics for these could not be calculated, others could still accurately determined and are provided.

6.2 Spatial Average Power Delay Profiles

At each receiver location we measured two orthogonal tracks of 80 PDPs each. We average all of these together by summing the linear powers of all of the PDPs and dividing by 160. By taking the spatial average of all 160 PDPs taken at each receiver location, we can accomplish two things. First, similar to the discussion in Section 2.6, we can strongly reduce the channel transient effects due to moving objects in the channel by spatial averaging. With 160 PDPs averaged at each location, we expect the transient effects to be virtually eliminated.

Second, and more importantly, spatial averaging will remove the effects of the fading that occurs because of small-scale fading. This fading, sometimes called wideband fading, occurs in PDPs because the power at a specific delay, τ_k, is a phasor sum of the power of several multipath components not resolvable by the measurement system. This was shown in Section 2.1.3. As the antenna is moved within the local area of the location, the power at τ_k fades. But the spatial average of the power at τ_k is the sum of the powers of the individual multipath components. Thus even from finite bandwidth sliding correlator measurements we can derive the sum of the powers of the individual multipath components by averaging many measurements in a local area. These are called the "Measured PDP" in Figs. (6.5) through (6.12).

6.3 Measured Fading Rate and Angular Spread

Also shown in Figs. (6.5) through (6.12) are the measured angular spread values. The angular spread is calculated for each peak in the measured PDP. The calculation of angular spread is described in Chapter 4. An example is given in Section 6.3.2 to help give the reader an intuitive feel for the calculation. Following this the plots of angular spread vs. time delay for each of the 22 measured links is displayed and described in Section 6.3.3. The discussion of the validity of the local-area assumption is discussed in Section 4.4. Finally, the discussion of the relationships of angular spread with time delay and with environment are discussed in Section 6.3.4.

Table 6.1: Table of Summary Measurement Results by Location

Link Descriptive Information					Spatial Avg PDP Data			Track PDP Data		
Link. #	Site Name	Env. Type	OBS. Type	d (m)	$\bar{\tau}$ (ns)	σ_τ (ns)	PL (dB)	min/max[σ_τ] (ns)	J_p (ns)	$\Lambda^2(\tau_0)$
(1)	Old Turner St.	Urban OBS	Automobiles	39.5	33.5	53.2	77.7	17.9 / 84.1	49	0.166
(2)	Old Turner St.	Urban LOS	-	175.3	16.7	50.7	75.2	3.8 / 82.6	19	0.135
(3)	Old Turner St.	Urban LOS	-	248.5	15.6	33.7	88.8	3.6 / 95.4	25	0.193
(4)	Old Turner St.	Urban OBS	Terrain	396.1	93.5	181.8	110.8	76.1 / 333.1	254	0.789
(5)	Southgate Dr.	Rural LOS	-	100.6	15.4	25.3	84.9	3.1 / 79.0	102	0.256
(6)	Southgate Dr.	Rural LOS	-	211.0	36.9	83.2	97.4	14.3 / 145.3	47	0.199
(7)	Southgate Dr.	Rural OBS	Trees	157.0	29.8	29.8	91.8	10.0 / 47.8	24	0.132
(8)	Beef Cattle Farm	Rural OBS	Terrain	332.3	209.4	333.2	106.2	201.8 / 396.1	259	0.143
(9)	Beef Cattle Farm	Rural LOS	-	393.7	14.2	40.8	95.9	4.2 / 95.8	13	0.131
(10)	Beef Cattle Farm	Rural OBS	Trees	453.6	140.4	289.1	110.9	23.3 / 398.4	251	0.131
(11)	Forest	Rural OBS	Trees	48.8	46.6	66.3	87.5	21.1 / 91.6	47	0.076
(12)	Forest	Rural OBS	Trees, Terrain	151.1	113.0	92.7	114.9	*	*	0.153
(13)	Hutcheson Hall	Urban OBS	Terrain	127.3	106.5	181.0	97.4	99.0 / 239.9	116	0.199
(14)	Hutcheson Hall	Urban LOS	-	50.0	26.5	39.7	75.5	13.7 / 57.6	29	0.103
(15)	Hutcheson Hall	Urban OBS	Bridge	145.5	15.9	34.6	94.2	5.6 / 101.5	60	0.166
(16)	Golf Course, Cage	Rural OBS	Trees	1293.9	98.2	156.7	121.8	22.9 / 362.8	260	0.144
(17)	Golf Course, Cage	Rural OBS	Trees	1135.8	92.3	213.0	122.2	*	213	0.169
(18)	Derring Hall	Urban OBS	Buildings	194.6	77.5	143.3	106.0	27.3 / 181.2	111	0.168
(19)	Derring Hall	Urban OBS	Buildings	254.8	36.1	79.1	115.0	15.4 / 102.4	84	0.318
(20)	Drillfield	Urban LOS	-	307.8	32.3	102.2	90.5	5.2 / 195.9	88	0.167
(21)	Drillfield	Urban LOS	-	556.7	53.5	106.1	106.1	2.1 / 172.3	263	0.198
(22)	Drillfield	Urban LOS	-	103.4	15.4	40.0	77.4	6.5 / 109.9	24	0.109

6.3.1 Measured Fading Waveforms

The measured power of a PDP peak as a function of position along a 20λ track is called the *fading waveform*. There were 752 fading waveforms measured in this campaign. Since only a few can be shown, several are selected randomly from the 22 different links. The random selection assures an unbiased collection of typical fading waveforms.

Three parameters about the waveform are provided on top of each waveform's plot. The link number, the time delay of the PDP peak, and the fading rate variance at the location are given. The first two are useful for looking up the link information in Table 6.1 and the PDP in Figs. (6.5) through (6.12).

The final number gives an estimate of the angular spread. Angular spread is not defined for a single track – it requires the fading rate variances from two orthogonal tracks. But to give the reader a feel for what the angular spread would be for the given fading waveform, the fading rate variance is given normalized to mean power and wave number. Thus the fading rate variance could be calculated from the number on the graph by multiplying it by the mean power, P_T^2, and by the wave number, $k^2 = 4\pi^2/\lambda^2$. Or without any calculation, the given number can be considered to be the one-track estimate of the angular spread. The actual measured angular spread will be the average of this number and the number for the orthogonal track.

6.3.2 Example

Consider the spatial average PDP at receiver location 8. This is at the rural site referred to as the Beef Cattle Farm, described in Section 5.6. The spatial average PDP is shown in Fig. (6.7 (1)). Consider the received power peak that appears at $\tau = 28$ ns. Its value, -119 dB, represents the average power that appears in 160 PDPs at that time delay.

Now look at the power as a function of position, that is, the fading waveform. This is shown for one of the 20λ tracks in Fig. (6.4).

The fading rate for the power at time delay τ_k is calculated at each point on the fading waveform

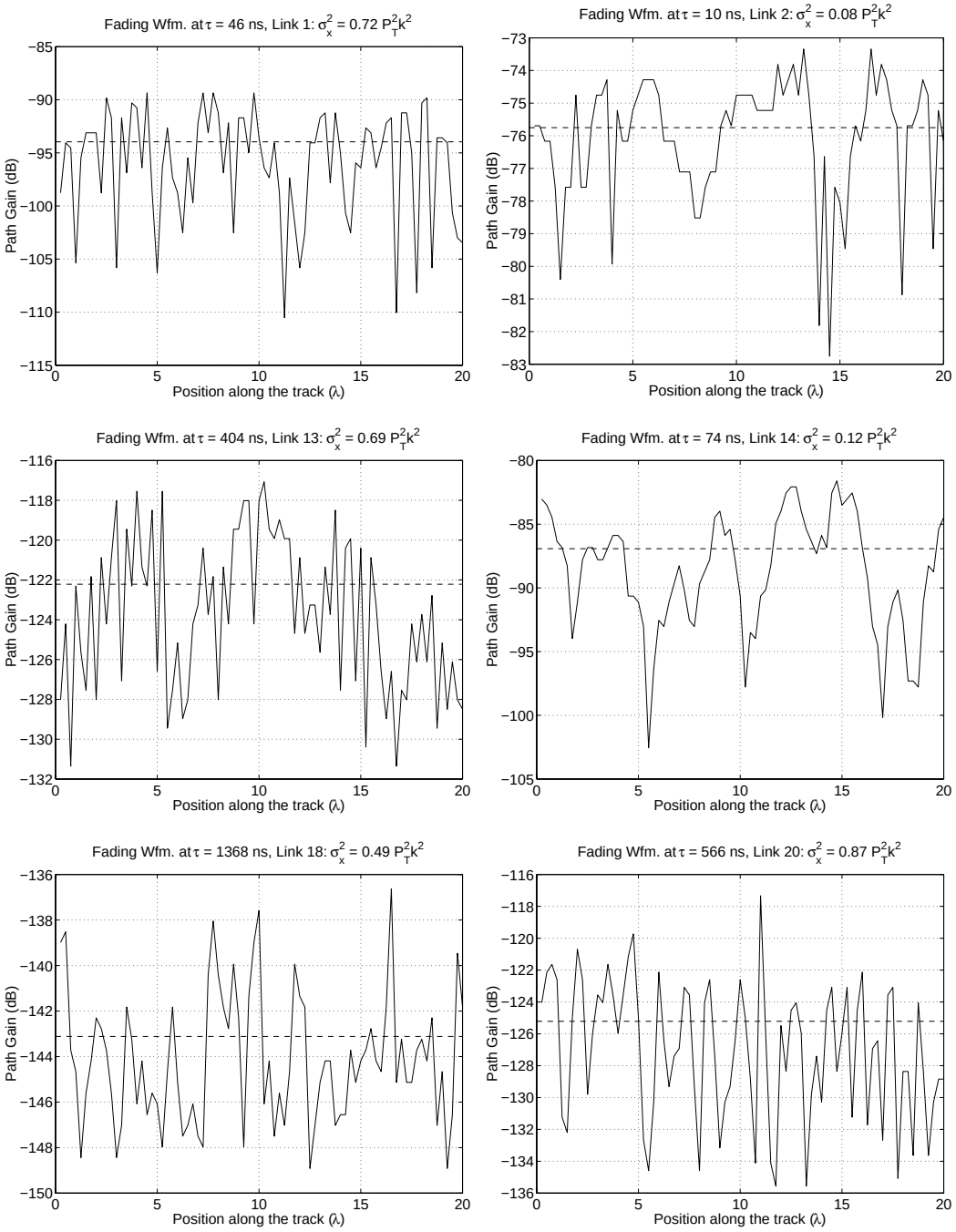

Figure 6.1: Measured fading waveforms in urban areas.

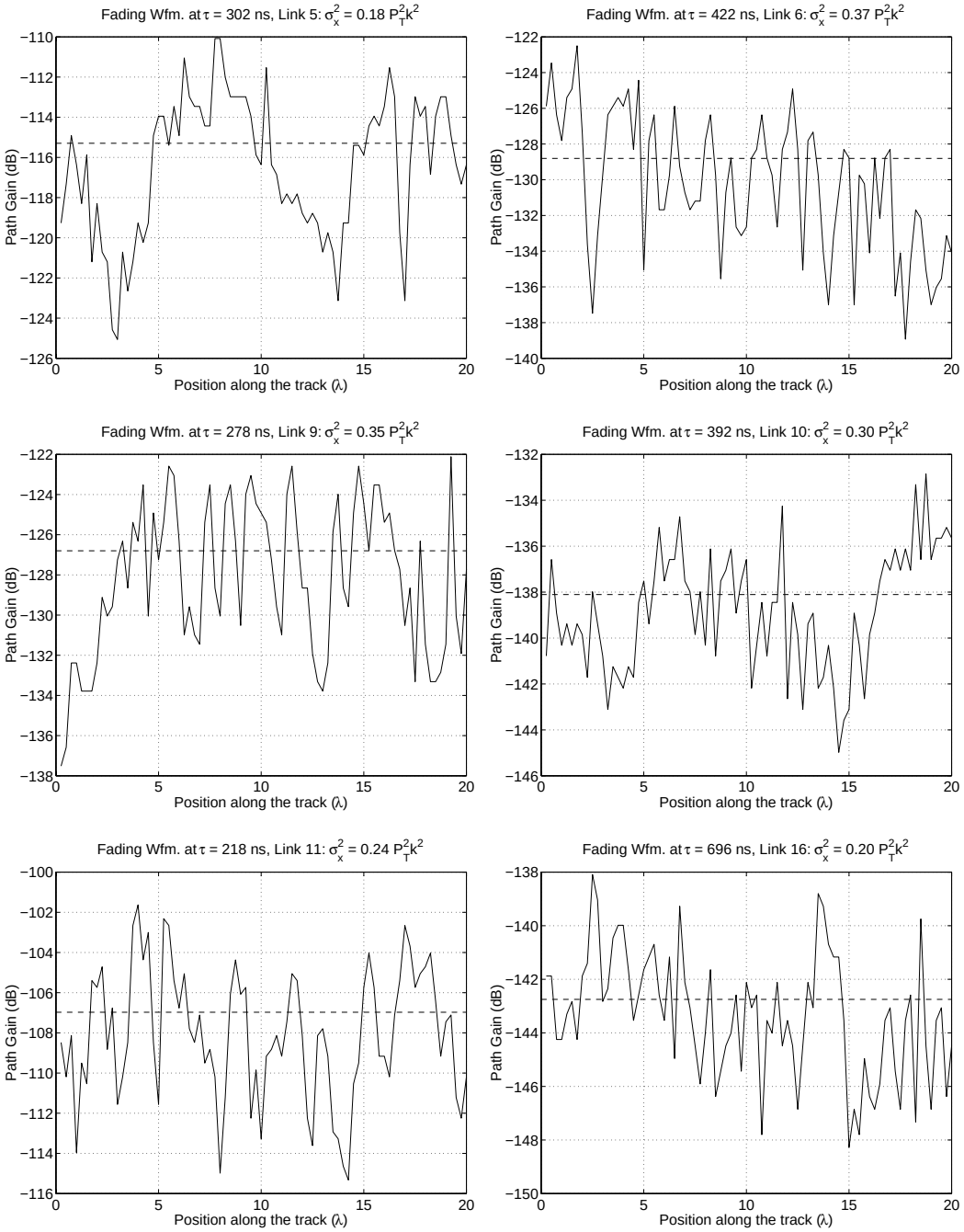

Figure 6.2: Measured fading waveforms in rural areas.

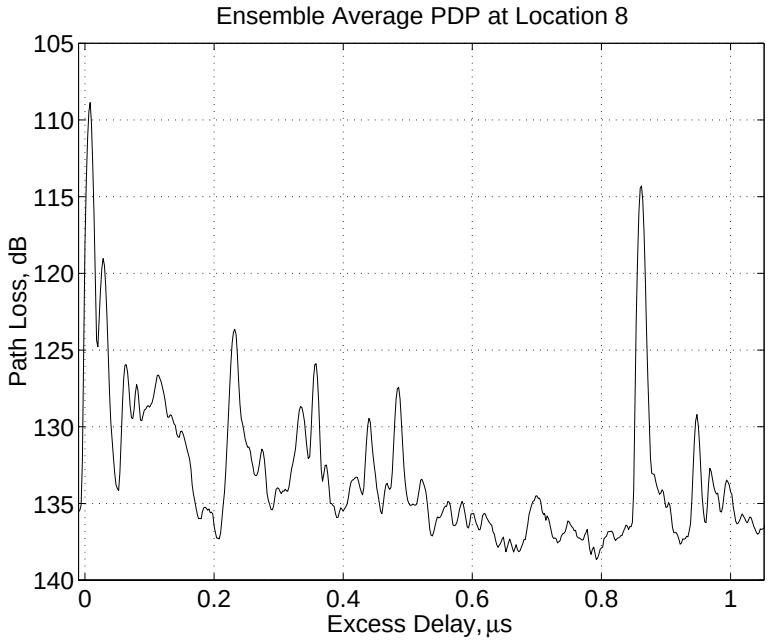

Figure 6.3: The spatial average PDP at receiver location 8.

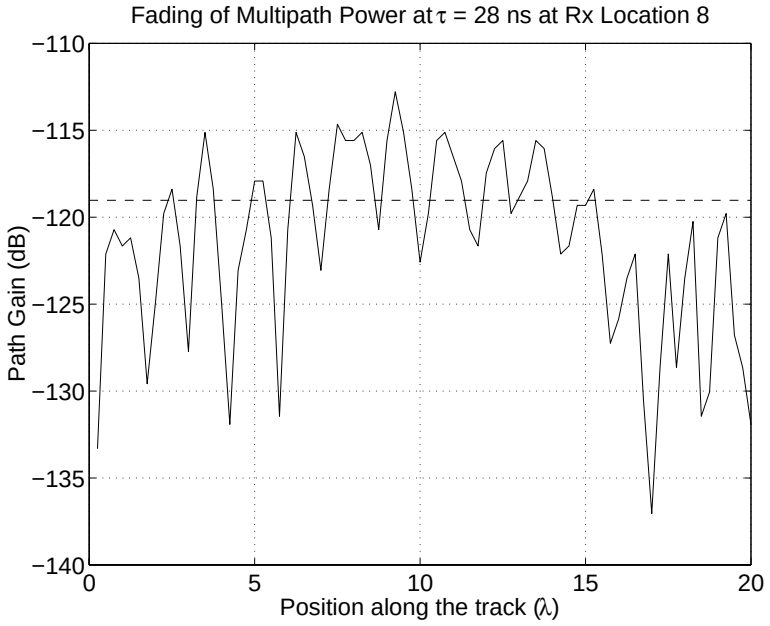

Figure 6.4: The fading waveform of a sample power peak from the power-delay profiles measured at receiver location 8.

using the FFT method described in Section 4.2.3. The variance of the fading rate is

$$\sigma_x^2 = 0.268 P_T^2 k^2 \tag{6.1}$$

where $P_T = -119dBm$ is the average local area power seen by the mobile and the k is the wave number, $2\pi/\lambda$. The result is left in this form since converting P_T to a linear power and then multiplying out would result in a very low number. In this form, the result makes more sense. Calculating the same fading rate for the orthogonal track, we find that

$$\sigma_y^2 = .431 P_T^2 k^2. \tag{6.2}$$

Note that the difference in the numbers is expected – the fading rates along each track should be show a dependence on the direction of travel relative to the AOA at the receiver. By Eq. (4.2) the local area fading rate variance is $\sigma_S^2 = 0.35 P_T^2 k^2$. As a result of Eq. (4.3), we know that the angular spread is calculated by:

$$\Lambda^2 = \frac{\lambda^2}{P_T^2} \sigma_S^2 \tag{6.3}$$

The λ^2 and the P_T^2 both cancel and the result is that the angular spread for the power peak at $tau = 28$ ns is $\Lambda^2 = 0.35$.

6.3.3 Plots of Angular Spread

Each plot that is presented in this section shows three important results:

- *Measured Spatial Average PDP*: The path gain in dB is plotted vs. time in (μs). The PDP curve is given by the blue solid line and the path gain values can be read on the right-hand side of the graph.
- *Measured Angular Spread*: The calculated angular spread is shown for each power peak in the PDP using black X's. Their values can be read from the left-hand axis of the graph. If a value for Λ^2 is above one, it is truncated to exactly one to fit on the graph.
- *Maximum Mean Angular Spread*: The dashed black line shows the maximum mean angular spread of the GBSBEM Model discussed in Section 3. The maximum mean angular spread of the Uniform AOA Model is equal to one, constant across time delay, and does not require an extra line on the graph.

The measurements from a site are grouped together and presented in a single figure. Thus Figs. (6.5) through (6.12) each present the measurement results (2-4 different links) at a single site. The

link numbers listed in the captions refer to the link numbers listed in Table 6.1. Using that table in combination with the figures, information such as the separation distance and obstruction type (if any) can be determined.

6.3.4 Discussion of Results

Local Area Assumption

By looking at the fading waveforms in Figs. (6.1) and (6.2), we can guess that in several cases, the local area assumption seems to have been violated. This is apparent when there is a significant and obvious change in mean power from one end of a track to another. But did this cause a significant increase in the fading rate? This is not clear.

Angular Spread Error

One indication of the effect of transient error on our measurements is the minimum measured angular spread? Ideally, this number should be very close to zero. In reality, the lowest measured angular spread is typically between 0.1 and 0.2.

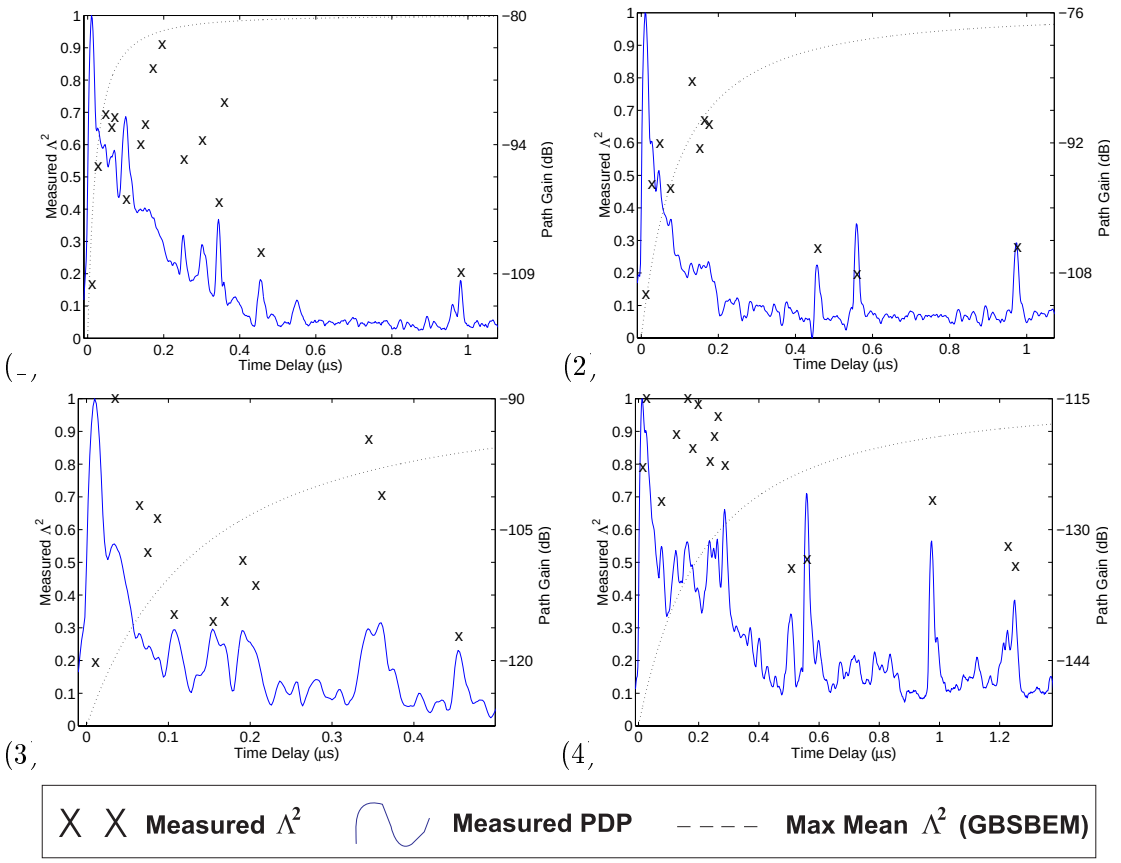

Figure 6.5: Measured PDPs and angular spread for links 1 through 4. These measurements are from the Old Turner Street site, an urban area.

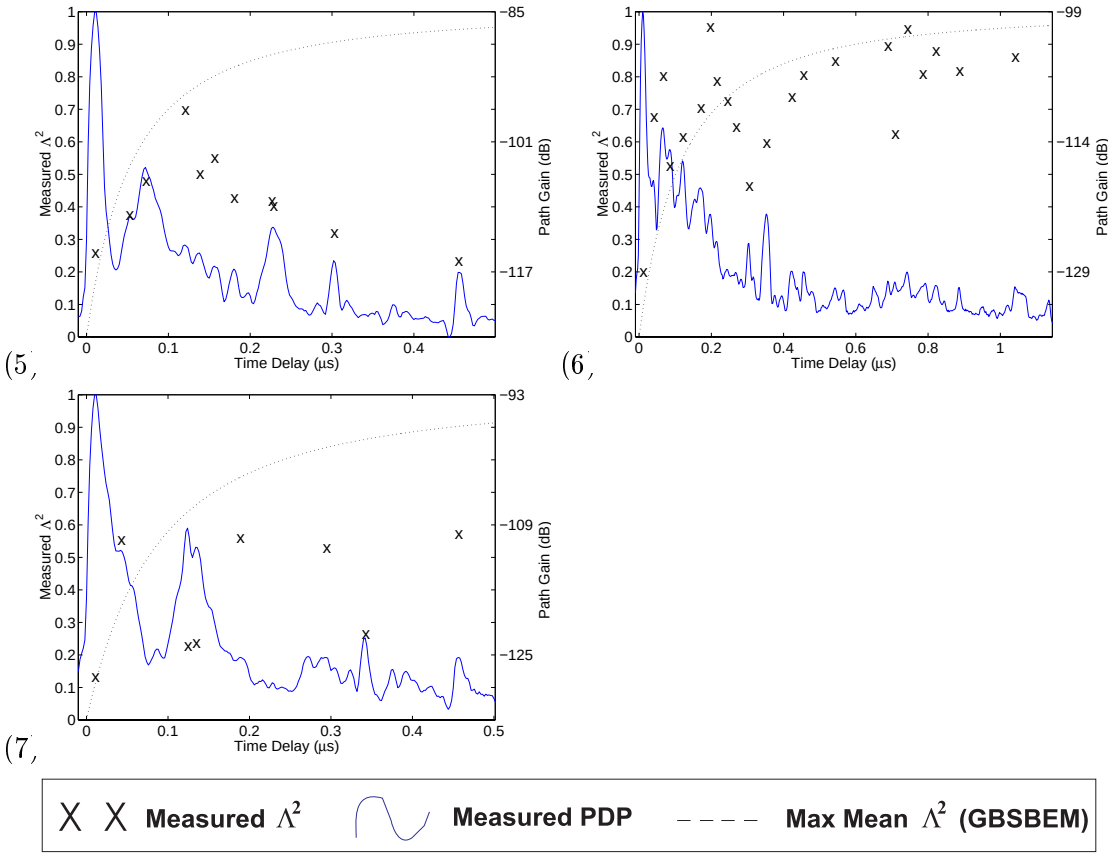

Figure 6.6: Measured PDPs and angular spread for links 5 through 7. These measurements are from the Southgate Drive site, a rural area.

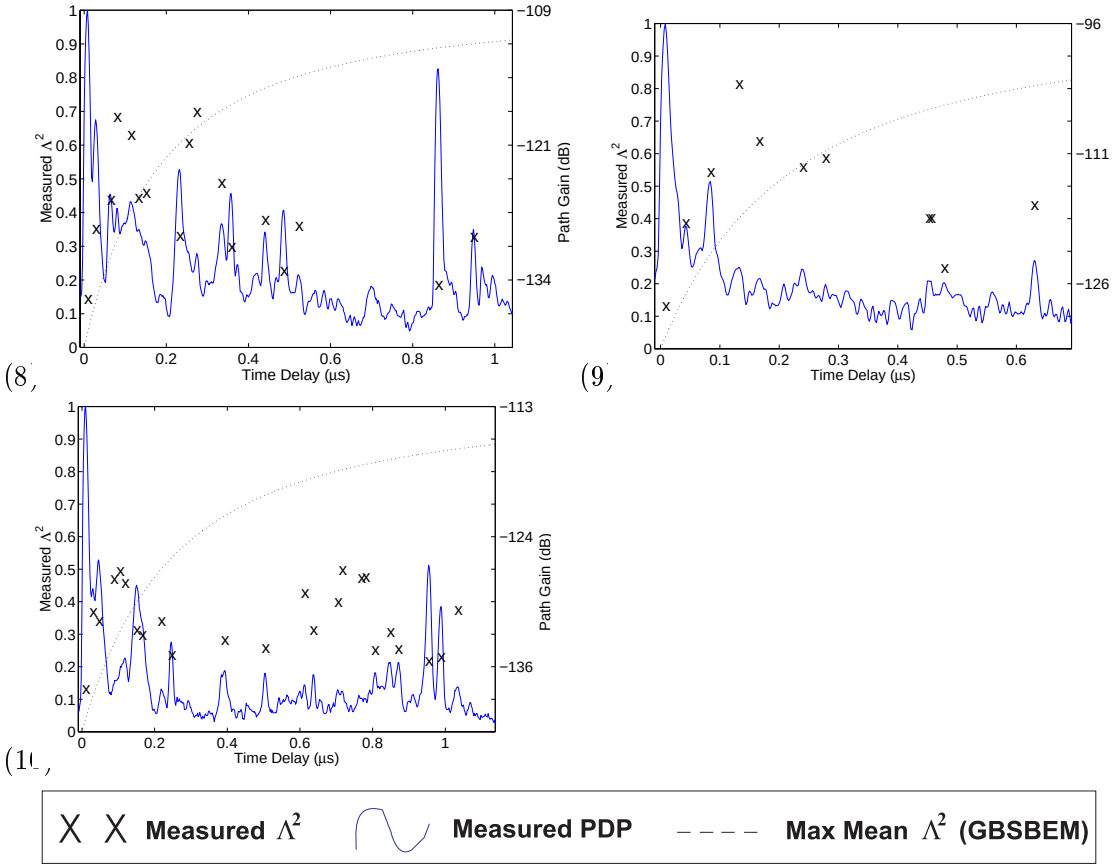

Figure 6.7: Measured PDPs and angular spread for links 8 through 10. These measurements are from the Beef Cattle Farm site, a rural area.

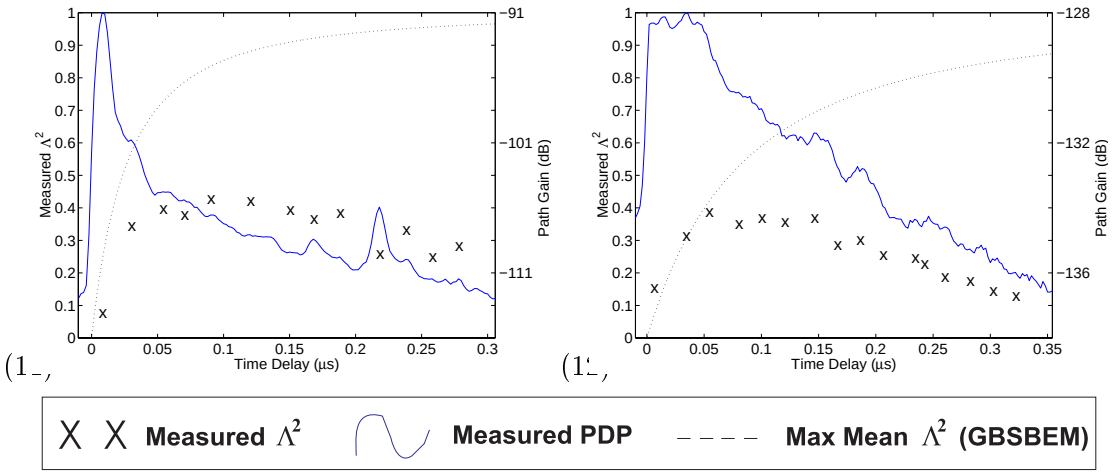

Figure 6.8: Measured PDPs and angular spread for links 11 and 12. These measurements are from the Beef Cattle Farm site, a rural area.

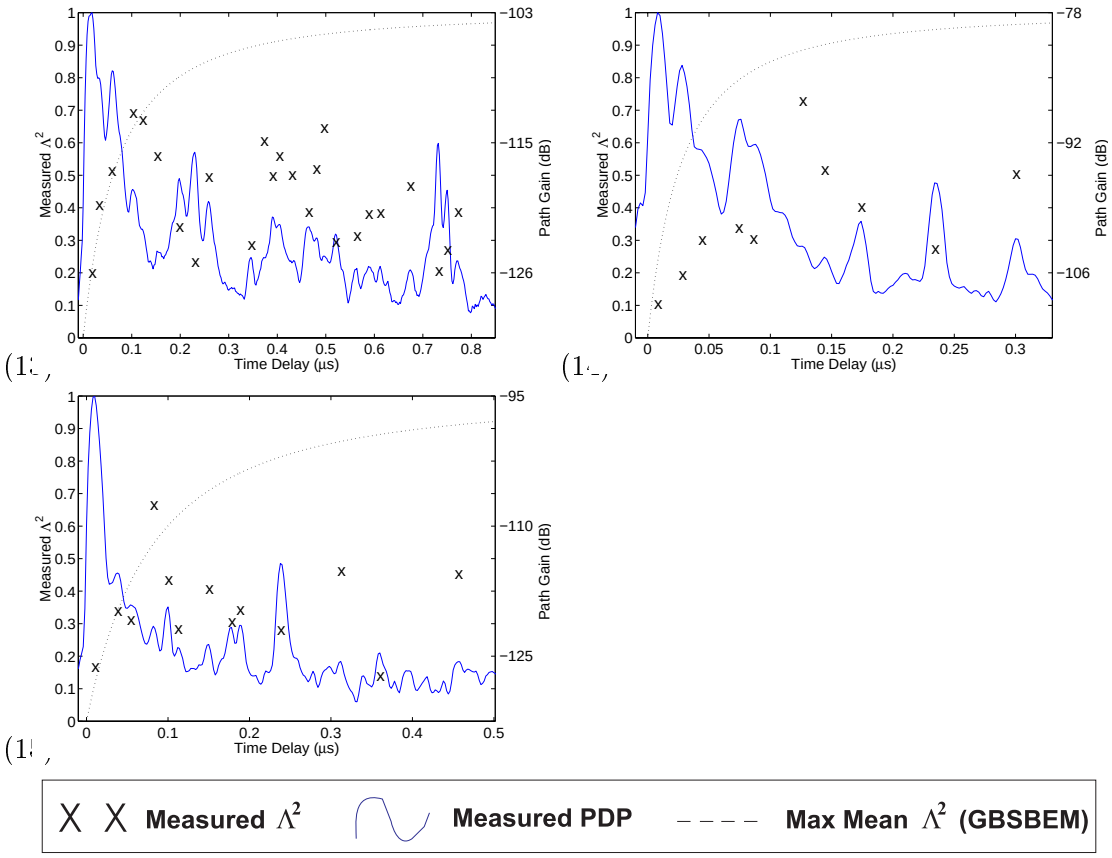

Figure 6.9: Measured PDPs and angular spread for links 13 through 15. These measurements are from the Hutcheson Hall site, an urban area.

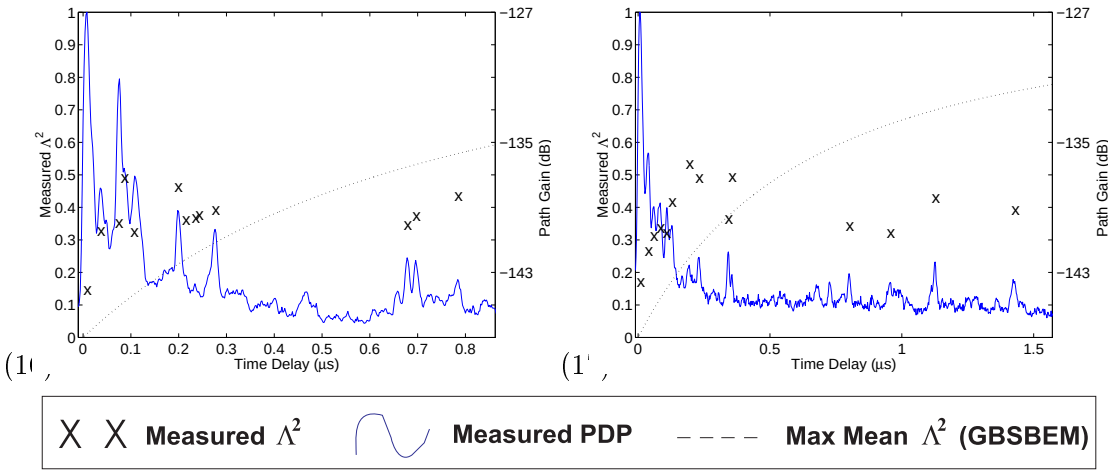

Figure 6.10: Measured PDPs and angular spread for links 16 and 17. These measurements are from the Golf Course / Cage site, a rural area.

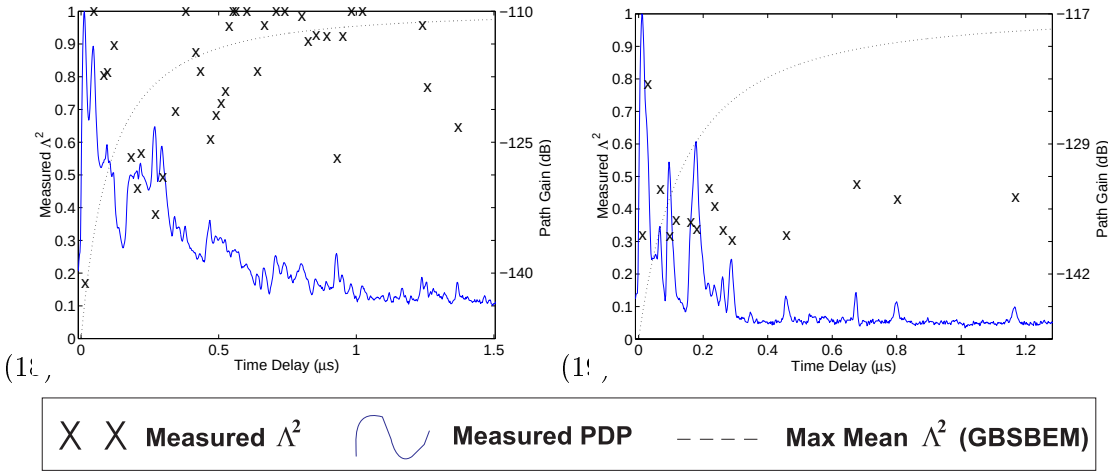

Figure 6.11: Measured PDPs and angular spread for links 18 and 19. These measurements are from the Derring Hall site, an urban area. Both links are OBS by buildings.

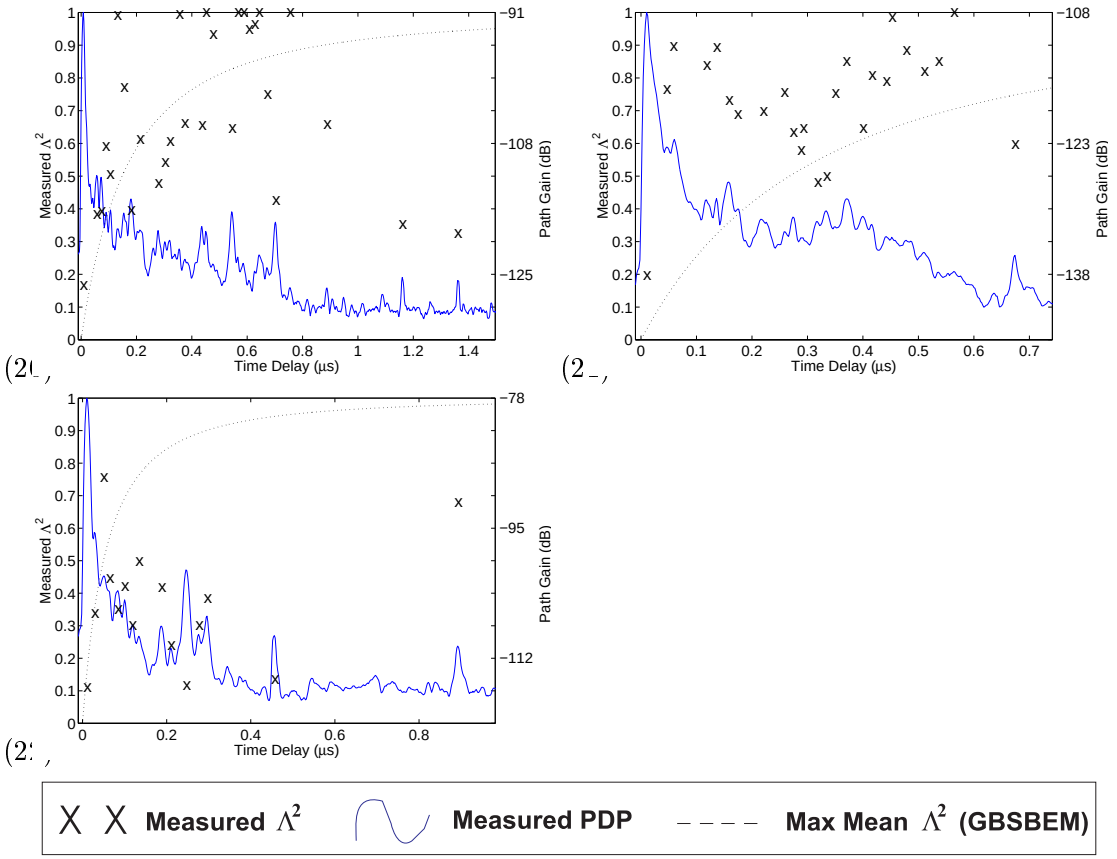

Figure 6.12: Measured PDPs and angular spread for links 20 through 22. These measurements are from the Drillfield site, an urban area.

This minimum is usually measured at the first PDP peak. This peak, in an LOS case, should have a very low angular spread. The only additional power that might contribute to this angular spread would be due to scattering off of the measurement equipment and its human operator. One example of the fading waveform for an LOS peak is shown in Fig. (6.1) for link 2. The power of the LOS peak varies by more than 8 dB! This measured fading, likely due to transient measurement error, results in an angular spread of $\Lambda^2 = 0.13$ (as shown in Fig. (6.5)).

Another hint to the effect of transient error is the measured angular spread of very late time delayed PDP peaks, where it seems unlikely that more than one component contributed to the peak. The minimum angular spread at late delays is usually between 0.2 and 0.3.

These minimum measured angular spread numbers apply to the analysis in Section 4.3. If the measured angular spread is a sum of the true angular spread and an error term, then a good rule of thumb is that this error term is between 0.1 and 0.2 for the first PDP peak and between 0.2 and 0.3 for the late-delayed peaks.

Also, we did calculate angular spreads above 1.0. On the graphs in Figs. (6.5)) to (6.12)), they are shown as X's at exactly 1.0 so that they fit on the graph. These values are clearly a result of significant measurement error, since an angular spread of more than one has no physical meaning. These meaningless calculated values are rare, however. In general, this rarity of calculated angular spreads above 1.0 gives us confidence in our ability to measure angular spread.

Angular Spread as a Function of Time Delay

We see very low values of angular spread for the LOS peaks where we expect that the first arriving power comes directly from the transmitter only. The angular spread quickly rises at low time delays when many multipath should arrive at the receiver. Finally, at long time delays, multipath arrive infrequently enough so that we expect the measurement system to resolve individual components, and we see lower angular spreads in the angular spread profiles. Most links show this behavior. This is the same as we described as expected behavior in Chapter 3.

Links 6, 18, and 21, in particular, do not show this behavior. The angular spread increases with increasing time delay even at very late time delays. In these cases, there are very low power peaks at the late time delays.

Angular Spread as a Function of Power Level

Note that most of the very high angular spreads are calculated for very low power PDP peaks. This may be an indication that there is no strong multipath component dominating the received power at that time delay. This observation is backed up by many very low angular spreads calculated for peaks with very high powers, even at very late delays. These high power peaks may be more likely to have a dominant contributing multipath component.

Also, at low mean power, P_T, the effect of the error contribution to the angular spread is higher. This is seen from Eq. (4.29). Thus a possible explanation for links 6, 18, and 21 is that they have high error variance in general for the link, and at the very low mean power levels, the error starts to have a very significant effect. As a rule of thumb, the peaks with higher powers tend to be more accurate.

Angular Spread in the Forest Environment

Links 11 and 12 are from the forest environment. Observation of the PDPs measured in these two links is that the transient errors in the measurements seemed to dominate the measurements. PDPs that were measured even while the receiver was at the same position saw very different multipath time delays and powers. This lead to a blurring of received power – the PDPs turned out to look much like an decaying exponential function than a series of PDP peaks. The calculated angular spread in these peaks was unusually constant across time delay. An analytical explanation for this observation has not been found. However, it is obvious that the actual angular spread of the environment was not accurately measured. A different method should be used in the future to determine the angular characteristics of the forest environment.

AOA Models and Angular Spread

The theoretical maximum mean angular spread for both the GBSBEM and the Uniform AOA Models can be seen on each graph in Figs. (6.5) through (6.12). The dotted line shows the maximum mean angular spread in the GBSBEM model, while the top line of the graph, $\Lambda^2 = 1$, represents that for the Uniform AOA Model. We don't know how many multipath arrived in each bin, and we don't know the noise contribution, so it's difficult to evaluate the AOA models. However, when the angular spreads are consistently above the model's maximum mean, we suspect the model. On average, many equal-power multipath in the same time-bin are needed to bring the

angular spread up to the maximum mean. Thus if the majority of calculated angular spreads hover around the maximum, we also suspect that the model is not accurately modeling the multipath. The number of angular spreads measured at or above the maximum mean of the GBSBEM gives the impression that the GBSBEM model does not always accurately model the peer-to-peer channel. To some degree, the angles-of-arrival of multipath at a given time delay seem more uniform in the peer-to-peer channel than the GBSBEM predicts.

6.3.5 Application to the Design of Rake Receivers

The typical behavior of angular spread has application to the design of rake receivers. Rake receivers usually use a pilot signal to sound the channel in real-time. It can then decide the time delays that each of the rake's fingers will downconvert. Since the measured angular spread of late-arriving PDP peaks usually has a low angular spread, a rake finger set to downconvert a late arriving peak will probably experience less fading and less Doppler spreading than a rake finger set to a lower time delay. Thus a good idea for the rake receiver would be to design it to prefer late time delays if the power peaks are high at those delays.

6.4 Narrowband Path Loss

Total narrowband received power can be inferred from wideband PDPs. This is because the spatial average received power at a location is simply the sum of the powers of the multipath components. This can be shown by analysis [20]. The measured PDP is recorded at discrete points $\Delta\tau$ apart and thus the spatial average received power is given by

$$P_{r,dB} = 10log_{10}\left[\sum_{k}^{N} P_{r,lin}(\tau_k)\ \Delta\tau\right] \tag{6.4}$$

where τ_N is the longest time delay in the power-delay profile, $P_{r,lin}(\tau_k)$ is the linear (W) received power at time delay τ_k and $P_{r,dB}$ is the dB spatial average received power.

The measured narrowband path loss is given by the formula

$$\bar{PL}_{dB} = P_{t,dB} + G_{t,dB} + G_{r,dB} - P_{r,dB} \tag{6.5}$$

where $P_{t,dB}$ is the transmitted power, $G_{t,dB}$ and $G_{r,dB}$ are the antenna gains at the transmitter and the receiver, respectively, and $P_{r,dB}$ is the narrowband received power, given above.

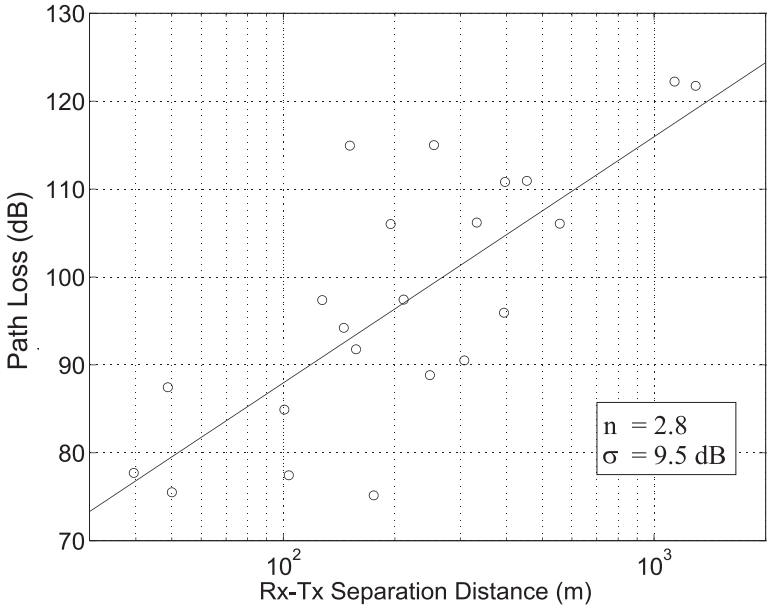

Figure 6.13: The path loss exponent model predicts narrowband path loss as a function of d_0, the transmitter-receiver separation distance. The path loss exponent $n = 2.8$ and the reference distance is 5 m. Also shown are the measurements used to derive the linear model.

The results of the calculation of Eq. (6.5) are given in Table 6.1. The path loss values are plotted as a function of transmitter-receiver separation distance in Fig. (6.13). This figure includes a linear model for the path loss as a function of path length, which is discussed in the following section.

6.4.1 Path Loss Exponent

A common model for radio wave propagation is the simple path loss exponent model. In this model, the mean total path loss at a distance d is given by

$$\bar{PL}_{dB} = PL_{ref}(d_0) + 10nlog_{10}\frac{d}{d_0} \tag{6.6}$$

where $PL_{ref}(d_0)$ is the reference path loss calculated by assuming free-space propagation until the reference distance d_0. This model is a measurement-based model, where d_0 is chosen and n is determined from least-squared error analysis. It is important to select a d_0 appropriate for the measurement environment. In cellular systems, a d_0 of 1 km are common, while in microcellular systems a d_0 smaller distances around 100 m to 1m are used [20]. The value found for n depends strongly on the choice of d_0 [12].

The effects of the choice of d_0 can be shown using these measurements. A range of d_0 was tested in

an attempt to minimize the least-squared error in our measurements. For each d_0, n was determined by linear regression. The sum of the squared error for a particular solution is given by

$$\epsilon^2 = \sum_i (PL_i - \hat{PL}_i)^2 \tag{6.7}$$

where PL_i is the total path loss measured at location i, and $\hat{PL}_i$ is the path loss predicted by Eq. (6.6) using d_0. The results are shown in Fig. (6.14). Note that n may range from 2.5 to 3.5 depending on the choice of d_0.

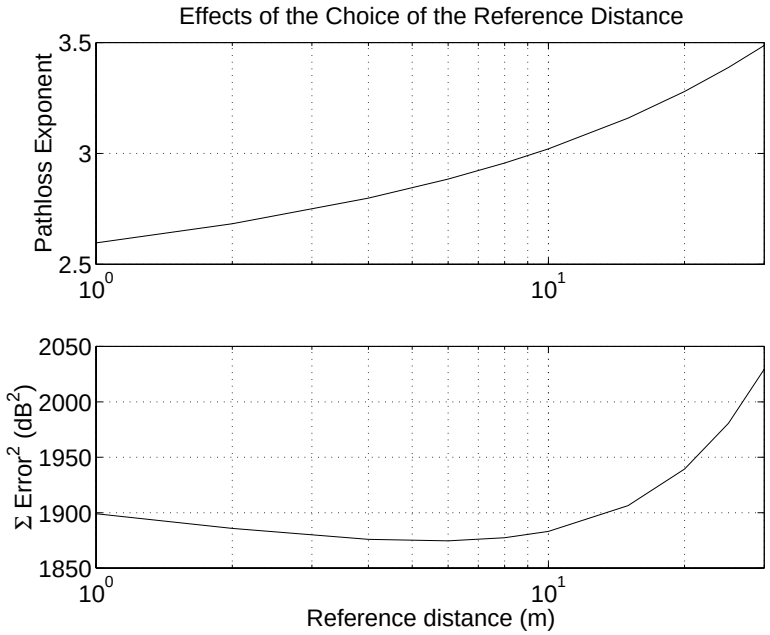

Figure 6.14: The path loss exponent and the sum of squared error is a function of the choice of the reference distance, d_0, for all 22 receiver locations.

The plot of sum of squared error shows that the minimum squared error is found using $d_0 = 5$ m. Using this reference distance, a path loss exponent of $n = 2.8$ is found. This is very close to the path loss exponent of $n = 2.7$ found from another measurement campaign on the Virginia Tech campus [29]. The standard deviation of the error of this model is $\sigma_{PL} = 9.5$ dB. The resulting equation for $\bar{PL}_{dB}$ is shown along with the measured data in Fig. (6.13).

6.5 Mean Delay

The mean delay of the channel is simply the first moment of the channel impulse response, given by

$$\bar{\tau} = \frac{\sum_{k=1}^{K} \tau_k P_k}{\sum_{k=1}^{K} P_k} \tag{6.8}$$

where τ_k and P_k are the time delay and received power of the kth multipath component, and K is number of multipath components.

In these measurements, the mean delay is calculated from PDPs rather than channel impulse responses. The calculation is done in the same manner; however, k now refers to an index on the time-delay axis. The values of τ_k and P_k are the time delay and received power at that index. The difference is subtle, but it leads to a small error in the calculated mean delay – a channel with no multipath at all will still result in a small calculated mean delay. This effect is due to the finite bandwidth of the measurements. The residual mean delay is approximately 10 ns.

It has been shown that in a multipath environment, the timing recovery circuits in a digital receiver track the mean delay of the impulse response of the channel [30]. When the fade frequency, given by the Doppler frequency, is much greater than the bandwidth of the timing recovery loop, the timing recovery circuit sees the spatial average PDPs as given in Section 6.2. This would likely be true for mobile radio, when the speed of the mobile is high. But when the Doppler frequency is lower than the bandwidth of the timing recovery loop, the recovery circuit is likely to track the mean delay of the individual channel impulse responses [31].

6.5.1 Timing Jitter

In portable radio channels, the change in the mean delay from position to position in a local area will play an important part in the operation of a digital receiver. A measurement campaign by Devasirvatham [31] measured eight power-delay profiles separated 1.7λ apart at each receiver location. From the results, he estimated the possible change in the mean delay a receiver experiences in a local area, which is referred to as the *timing jitter* or the *peak-to-peak jitter*. The timing jitter in a local area is defined as

$$J_p = \max[\bar{\tau}_i] - \min[\bar{\tau}_i] \tag{6.9}$$

In Devasirvatham's study, i was between 1 and 8. Devasirvatham noted that the limited number of measurements provided only approximate bounds on the jitter.

In this thesis there are 160 measurements at each local area and thus we expect the measured jitter to be a very good estimate. The measured jitter for each location is given in Table 6.1. At receiver location #12, because of the extremely rapidly varying channel and the very low dynamic range (see the PDPs in Fig. (6.8)), the timing jitter is not calculated. This is the Forest location shown in Appendix A.7. This remains an interesting research issue because the forest channel has not been characterized adequately. Future research could study the time-variation of this channel further.

The results indicate that timing jitter is well-correlated with mean delay and with RMS delay. This relationship is shown in Fig. (6.15). This is important because not only do these links suffer from high ISI, they are also likely to experience severe jitter. Since jitter is a measure of the difficulty of keeping accurate timing in a timing recovery circuit, these high-σ_τ channels are also more likely to experience timing difficulties.

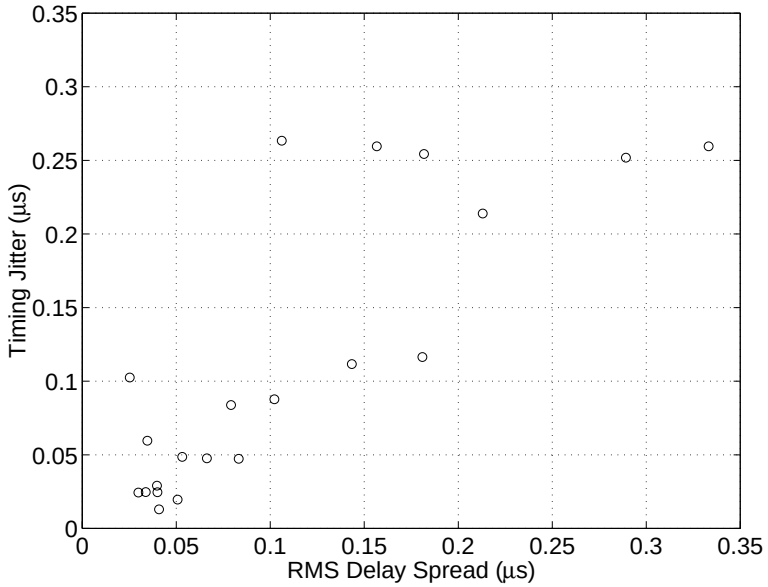

Figure 6.15: Measurements show that channels with high RMS delay spreads are also likely to experience severe timing jitter.

6.6 RMS Delay Spread

The RMS delay spread is one of the most important parameters of digital communications channels. It shows to what degree a digital communication system will experience inter-symbol interference

(ISI) in a given channel [30]. It is calculated as the second central moment of the PDP:

$$\sigma_\tau^2 = \bar{\tau^2} - (\bar{\tau})^2 \tag{6.10}$$

where

$$E[\tau^2] = \frac{\sum_{k=1}^{K} \tau_k^2 P_k}{\sum_{k=1}^{K} P_k} \tag{6.11}$$

The RMS delay spread is more sensitive to late-arriving power. This is similar to the sensitivity of a digital receiver – late arriving power is likely to cause more severe ISI than power with small time delays. This is an intuitive reason that explains why bit error rates in receivers without equalizers tend to be strongly correlated to the RMS delay spread. In addition, the inverse of the RMS delay spread is proportional to the coherence bandwidth, thus it has a direct implication to the frequency spectrum of the received signal [20]. Furthermore, the RMS delay spread gives insight into the shape of the PDP. In fact, an analysis of the RMS delay spread by environment, urban or rural, shows that the shape of the PDPs are different in the two different environments.

6.6.1 Coherence Bandwidth

The coherence bandwidth is a measure of the range of frequencies over which the channel can be considered to be flat fading. A common estimate of the coherence bandwidth is given by an inverse proportion to the RMS delay spread:

$$B_c \approx \frac{1}{5\sigma_\tau} \tag{6.12}$$

The bandwidth of the HMT, 10 MHz, can only be considered to be in a flat fading channel if $\sigma_\tau < 20$ ns. For low transmitter / receiver separation distances, this is often possible. However, in general, this is not the case, as seen in Fig. (6.1). At large separation distances, the coherence bandwidth can be as low as 500 kHz. Not surprisingly, this work demonstrates that an equalizer is a necessary part of the HMT communications system.

6.6.2 Relationship of σ_τ and path loss

One basic relationship in radio wave propagation channels is the behavior of RMS delay spread as a function of path loss. The measured path loss vs. RMS delay spread for these measurements is plotted in Fig. (6.16). It is also plotted in Fig. (6.17) showing the difference between the urban and rural measurements.

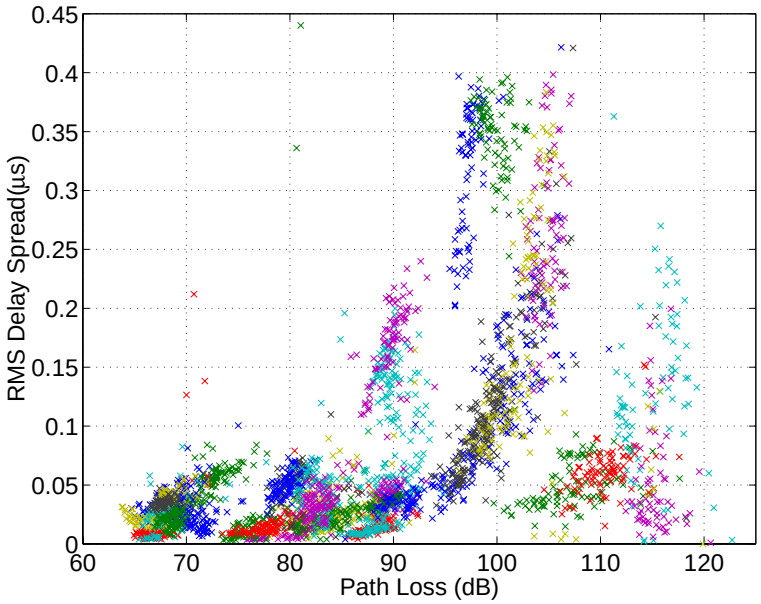

Figure 6.16: The narrowband path loss of all measured PDPs are plotted against RMS delay spread. Each color represents a single receiver location.

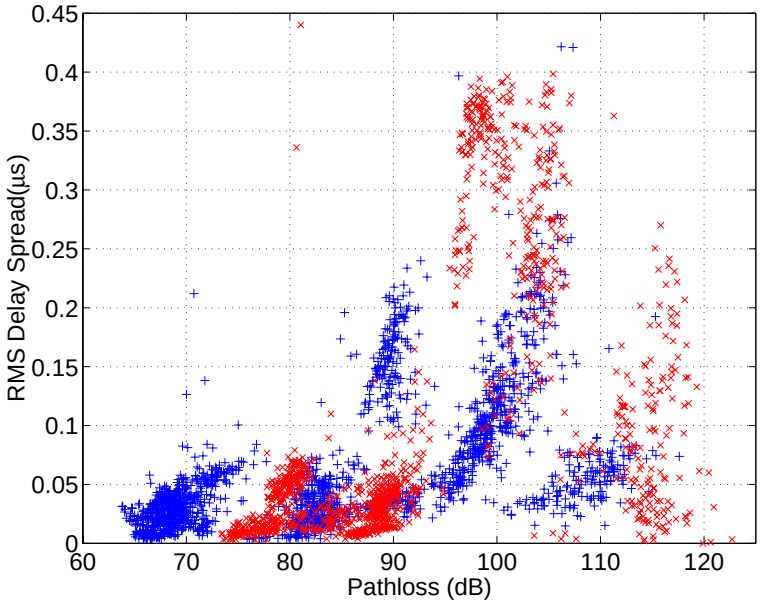

Figure 6.17: The narrowband path loss of measured PDPs are plotted as a function of environment, rural or urban.

At low path loss values the RMS delay spread is typically low. As path loss increases, the maximum RMS delay spread increases exponentially, however, the minimum stays constant. At high path loss the variance of the RMS delay spread increases. This same relationship has been shown by previous research. Feuerstein, et. al. recorded the measured data shown in Fig. (6.19) [4] from microcellular environments in the San Francisco Bay area at 1900 MHz.

Devasirvatham has shown similar results for in-building measurements, shown in Fig. (6.18) for his measurements at 850 MHz for both a small office building and a large office building [3].

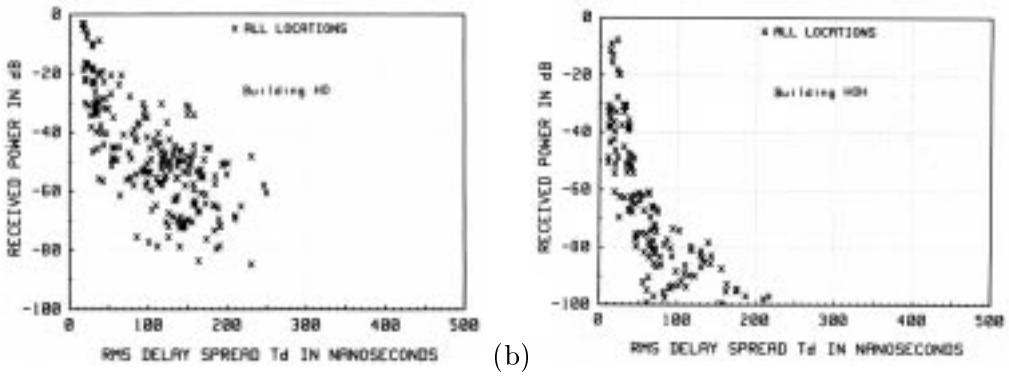

Figure 6.18: Received power in dB versus RMS delay spread for a (a) large and (b) small office building, from [3].

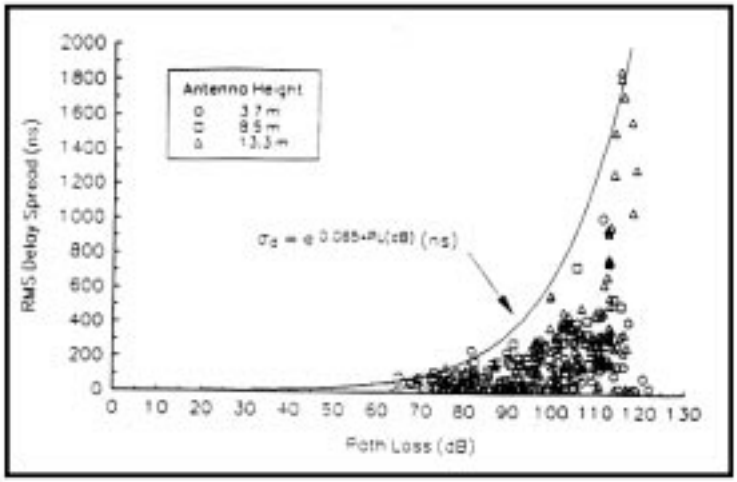

Figure 6.19: Path loss versus RMS delay spread for measurements reported in [4].

6.6.3 Relationship of σ_τ and $\bar{\tau}$

Previous measurement campaigns have shown a linear relationship between measured mean delay, $\bar{\tau}$ and RMS delay spread, σ_τ [31]. In these measurements, a strong linear relationship exists between $\bar{\tau}$ and σ_τ.

First, using the $\bar{\tau}$ and σ_τ of the spatial average PDPs, a linear relationship was found. As seen in Fig. (6.20), the RMS delay spread of a spatial average PDP is well correlated to its mean delay. By the method of least squares, we have the linear regression

$$E[\sigma_\tau] = 0.014 + 1.6\bar{\tau} \tag{6.13}$$

The correlation coefficient for the two sets of data is 0.94. The standard deviation of the error in the model is 30.5 ns.

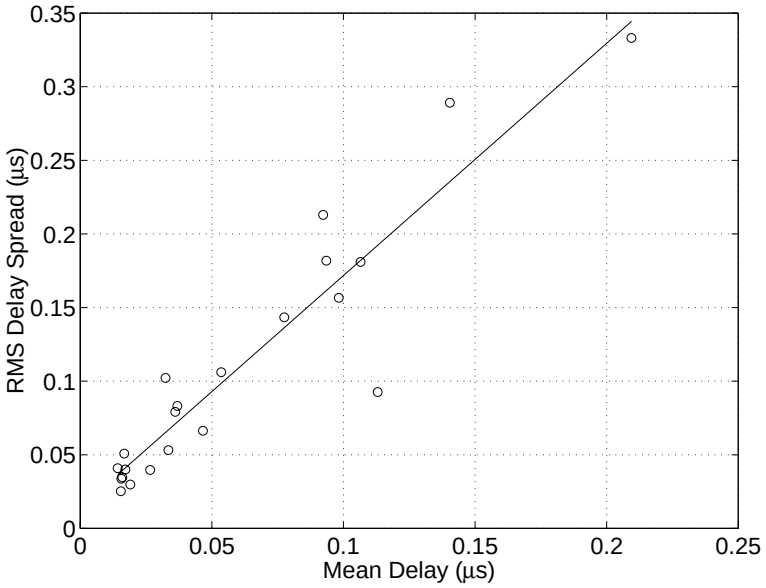

Figure 6.20: The RMS delay spread of a spatial average PDP appears to be linearly related to its mean delay by the formula, $E[\sigma_\tau] = 0.014 + 1.6\bar{\tau}$. The standard deviation of the error of the linear model is 30 ns.

However, this linear relationship covers up another interesting relationship which can be seen if we plot every measured PDP. The plot of all measured RMS delay spreads vs. their mean delay is given in Fig. (6.21). It is still apparent that there is a relationship between mean delay and RMS delay spread.

In fact, some of this underlying structure is revealed when we group together the data from urban

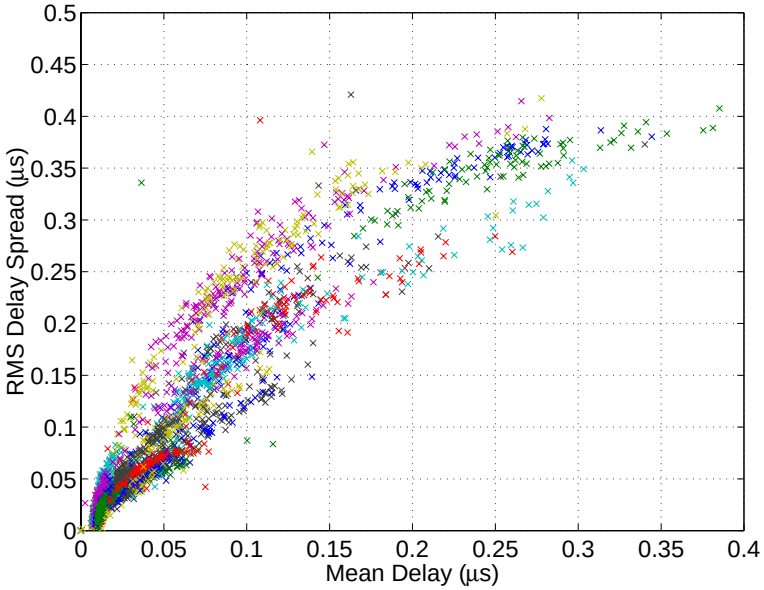

Figure 6.21: The RMS delay spreads and mean delays of all measured PDPs are plotted. Each color represents a single receiver location.

sites and the data from rural locations as is shown in Fig. (6.22). The measurement data from the rural locations are shown in this figure as the red x's and the rural as the blue +'s. The rural locations, in general, have a higher RMS delay spread given mean delay than the urban locations. The rural measurements rise more steeply than the urban locations and then taper off at high mean delays.

The relationship between mean delay and RMS delay spread is related to the shape of the PDPs. Devasirvatham has given several examples of PDP shapes and the resulting relationship between mean delay and RMS delay spread [31]. A bell-shaped PDP would result in an RMS delay spread smaller than the mean delay. Conversely, a PDP strongly peaked at the start but with a long finite tail would have an RMS delay spread smaller than the mean delay. The RMS delay spread should be equal when the PDP looks exponential or when it is the simple case of exactly two arriving equal-amplitude multipath. These scenarios are depicted in Fig. (6.23) to provide some physical insight into how PDPs correspond to particular σ_τ and $\bar{\tau}$ relationships. These are not the only PDP shapes possible, but they give an idea of what types of PDPs might be expected.

This is important because when applied to our measurement results from Fig. (6.22) it means

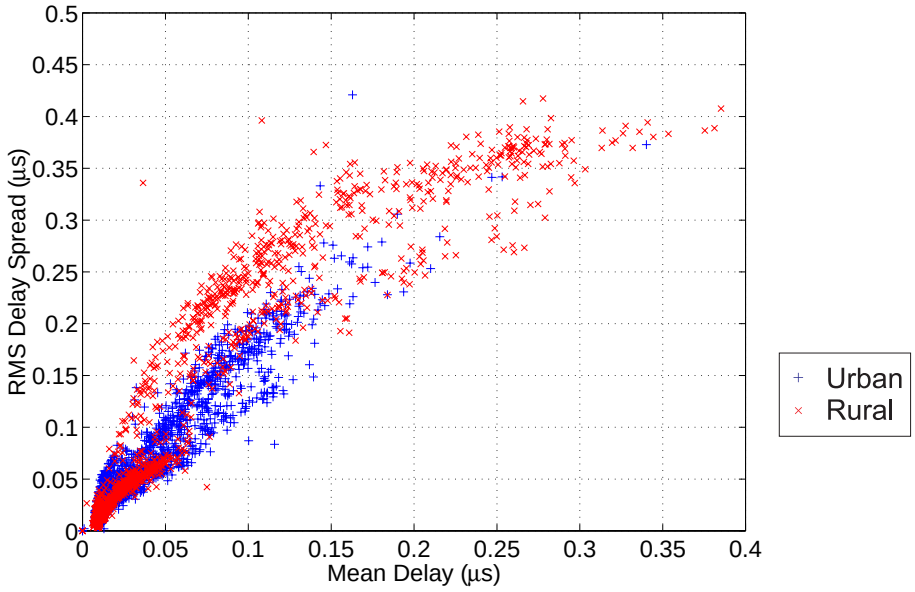

Figure 6.22: The RMS delay spreads and mean delays of measured PDPs are plotted by environment, urban and rural. The rural receiver locations have a higher RMS delay spread for a given mean delay compared to urban locations.

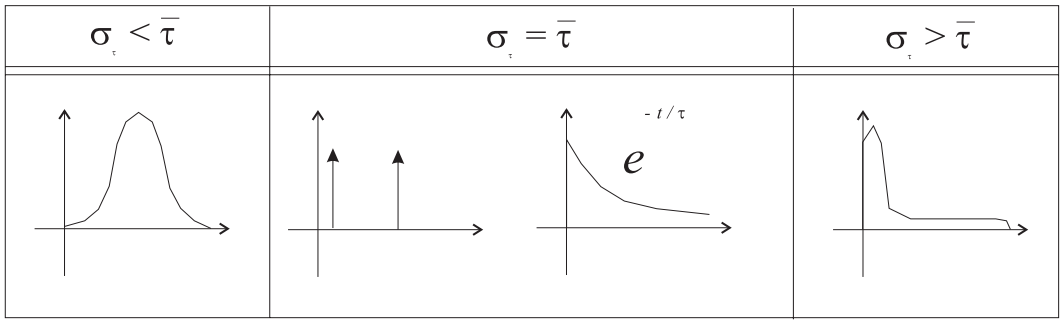

Figure 6.23: The RMS delay spreads and mean delays of measured PDPs are related by their distribution shape.

that the shape of urban PDPs are different from rural PDPs. Rural channels, with RMS delay spreads about two times their mean delays, are more likely to have a strong LOS peak and small late-arriving multipath power, especially at low mean delays. The urban channels were measured to have a lower slope in their mean delay to RMS delay spread relationship. We can conclude that they are more likely to see significant the late arriving power that makes the PDP look more like an exponential distribution or even like a two-ray profile. This is not an inflexible rule – there are exceptions. However, a glance through the PDPs shown in Appendix A shows that the shape of PDPs is generally different for urban and rural channels.

Chapter 7

A Measurement-Based Channel Model

Accurate channel models are necessary for both communication system verification and optimization. Their algorithms are implemented in computer simulations in the design stage and in hardware during the prototyping and testing stages. The operation of a system in real channels is assured by an accurate channel model.

The generation of complex channel impulse responses for use in a mobile radio simulation is not a trivial task. The model must accurately predict the amplitudes and phases of multipath signals as a function of time delay and position. But these amplitudes and phase angles are also a function of environmental variables that describe the transmitter-receiver link. Typical environmental variables are transmitter-receiver separation distance, the antenna heights, scatterer density, the type of environment, eg., urban, suburban or rural, and the obstructions (if any) in the LOS path.

It is a very difficult problem to correctly model the amplitude and phase variables as a function of all these simultaneous variables. Some ambitious statistical models such as SMRCIM [32] attempt to extrapolate their measurement results to predict PDPs at points which were not directly measured. Because of the difficulty of modeling simultaneous dependencies on environment variables and time delay, these extrapolating statistical models sometimes misrepresent some of the dependencies.

This model attempts to accomplish a limited but useful segment of this task. It uses only measured PDPs. This assures the model's correct modeling of the power of PDP peaks as a function of time delay and environment type. Another characteristic of this algorithm is that it models the relationship between angle-of-arrival and small-scale fading. The algorithm generates an AOA

distribution based on the measured angular spread for each PDP peak. This results in a simulated fading rate variance equal to the PDP peak's measured fading rate variance. In addition, this method results in an accurate simulation of the phase (Doppler) characteristics of the channel. The received phases of the peaks in the channel impulse response were not measured – the ability to produce valid phase progressions for these peaks is a significant achievement.

7.1 Algorithm

The inputs to this model are the measured spatial average PDP and the measured angular spread for the local area. The algorithm proceeds in the steps as follows.

1. Load the spatial average power delay profile. Specifically, load the list of time delays and amplitudes of the PDP's power peaks. Also load the angular spread value associated with each peak.

2. Use the one of the AOA models of Fig. (7.2)to generate an angle-of-arrival characteristic for each of the peaks. Any of the AOA models will produce a fading waveform with the measured fading rate variance.

3. The AOA characteristic determines a Doppler filter. Pass I and Q Gaussian noise through this filter to produce an complex envelope fading waveform.

4. Decimate the PDP to the necessary simulation bandwidth by convolving it with a low-pass filter that approximates the receiver IF filter. The resulting amplitudes and phases are the taps of the multipath channel FIR filters to be used in the system simulation.

5. When the mobile terminal is being simulated in motion, the particular multipath channel FIR filter must be changed with each change in position.

In this method, the power at a time delay is dependent on the power at the same time delay at other positions along the track. In addition, the phase changes at each time delay are due to a continuous angular distribution of arriving multipath power. Its behavior along a track is shown in Fig. (7.1).

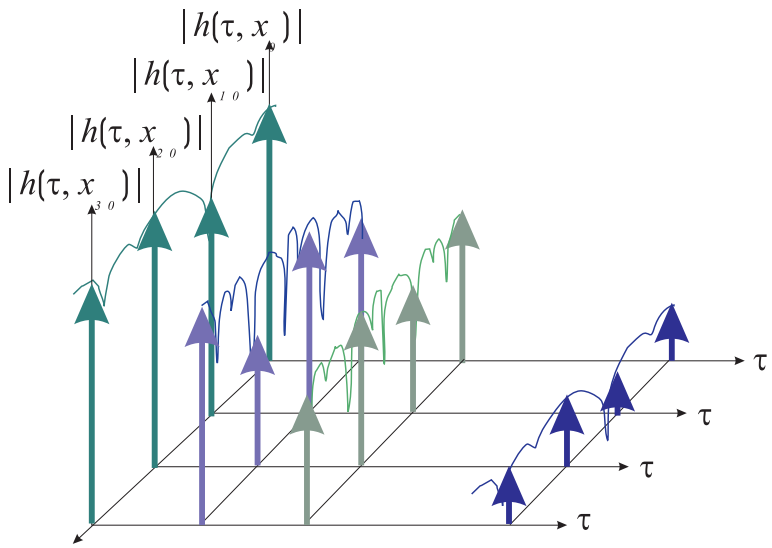

Figure 7.1: An example output of the measurement-based model. The algorithm reproduces channel impulse responses with the same multipath time delay, mean power, and fading rate variance measured during the measurement campaign. This figure shows the magnitude of the model's channel impulse responses along a track.

7.2 AOA Models and Generation Methods

Three families of angular distributions of arriving power are proposed in this thesis. Any of these three can be used to describe the multipath power that contributes to the arriving power at the receiver for a particular power peak. These three models are shown in Fig. (7.2). Each is simple enough to allow for easy simulation. Each one can be used to reproduce the correct (measured) fading rate variance. Also, each results in a different probability density function (PDF) of received signal envelope.

7.2.1 Two-Ray Model

This AOA model assumes that two equal-amplitude multipath components contributed power to this time-bin. This model seems intuitively valid in situations such as late arriving multipath when we believe that power arrives from just a couple of directions.

The angular spread of the model is calculated assuming two discrete multipath with power P arrive at a receiver separated by an azimuthal angle α, as seen in Fig. (7.2a), and defined mathematically

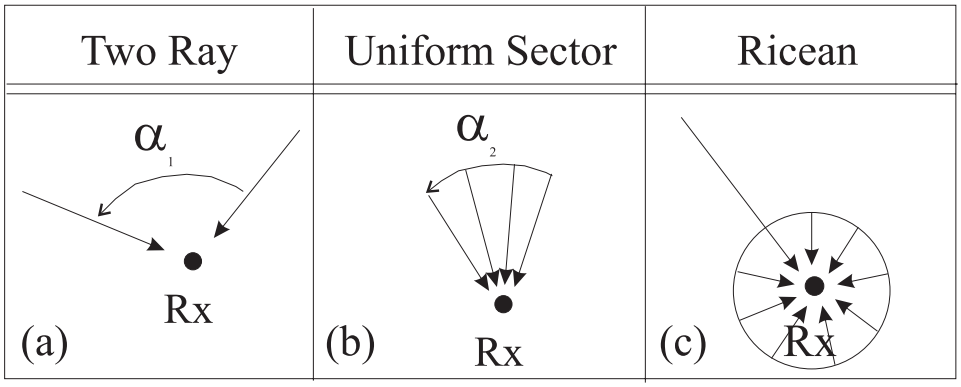

Figure 7.2: Possible AOA models used for generating fading waveforms: (a) two discrete rays arrive at a receiver, (b) multipath power arrives uniformly from a sector of angles, or (c) some multipath power arrives uniformly around the receiver but some more arrives in a ray from a single direction

as

$$p(\theta) = P\,\delta(\theta - \theta_o) + P\,\delta(\theta - \theta_o - \alpha) \tag{7.1}$$

where θ_o is any arbitrary azimuthal direction and $\delta(\theta)$ is an impulse function. The first step is to calculate the Fourier coefficients:

$$|F_0| = 2P \qquad\qquad |F_1| = P\sqrt{2(1+\cos(\alpha))} \tag{7.2}$$

The subsequent angular spread, after substituting with basic trigonometric identities, is given by the simple expression

$$\Lambda = \sin\left(\frac{\alpha}{2}\right) \tag{7.3}$$

Eq. (7.3) provides insight into the definition of angular spread. The limiting case of two multipath arriving from the same direction ($\alpha = 0$) results in zero angular spread. An angular spread of 1 results only when the two multipath are separated by $\alpha = \pi$ radians.

For any angular spread, we can calculate the angle of separation α by the formula

$$\alpha = 2\sin^{-1}\left(\frac{\Lambda}{2}\right) \tag{7.4}$$

We use this relation in simulation. The first arriving multipath is chosen with random direction θ_o and the second multipath as a result must arrive from $\theta_o + \alpha$.

Note that each multipath will have its own Doppler frequency. In the frequency domain, this means we will see two delta functions. In the time domain, the fading waveform will be the sum of two sinusoids.

7.2.2 Uniform Sector Model

This model assumes a uniform distribution of arriving multipath power from a sector of angles, as seen in Fig. (7.2b) and given mathematically by

$$p(\theta) = \begin{cases} \frac{P_T}{\alpha} & : \quad \theta_o \leq \theta \leq \theta_o + \alpha \\ 0 & : \quad \text{elsewhere} \end{cases} \tag{7.5}$$

The angle α indicates the width of the sector (in radians) of arriving multipath power and the angle θ_o is an arbitrary offset. Power arrives uniformly within the range of azimuthal angles; no multipath power arrives from outside this range.

This model represents a diffuse spread of angular power. It can be seen as a Rayleigh channel since many multipath contribute to the arriving power without a single dominant component.

The magnitude of the Fourier coefficients follow:

$$|F_0| = \left| \int_{\theta_o}^{\theta_o+\alpha} \frac{P_T}{\alpha} d\theta \right| = P_T \qquad |F_1| = \left| \int_{\theta_o}^{\theta_o+\alpha} \frac{P_T}{\alpha} \exp(j\theta) d\theta \right| = \frac{2P_T}{\alpha} \sin\left(\frac{\alpha}{2}\right) \tag{7.6}$$

Upon simplification, the subsequent angular spread becomes

$$\Lambda = \sqrt{1 - \mathrm{Sn}^2\left(\frac{\alpha}{2}\right)} \tag{7.7}$$

where the sinc function, $\mathrm{Sn}(x)$, is equal to $\sin(x)/x$.

The limiting cases of Eq. (7.7) provide deeper understanding of angular spread. The limiting case of a single multipath arriving from precisely one direction corresponds to $\alpha = 0$, which results in $\Lambda = 0$. The other limiting case of uniform illumination in all directions corresponds to $\alpha = 2\pi$, which results in the maximum angular spread of 1.

There is no analytical expression for the angle α, but it can be found from the expression

$$\alpha = 2\mathrm{Sn}\left(\sqrt{1 - \Lambda^2}\right) \tag{7.8}$$

using simple numerical methods. The answer for α is unique since it is limited to the range $[0, 2\pi)$.

We must also be able to describe the Doppler power spectrum of this model. This can be done using the classical Clarke & Gans fading model [33] [20]. Here, we assume a complex baseband simulation and thus take the center frequency to be zero.

$$S(f) = \begin{cases} \frac{p(\theta)G(\theta)-p(-\theta)G(-\theta)}{f_m\sqrt{1-\left(\frac{f}{f_m}\right)^2}} & : \quad |f| \leq f_m \\ 0 & : \quad \text{elsewhere} \end{cases} \tag{7.9}$$

where

$$\theta = \cos^{-1}\left(\frac{f}{f_m}\right) \tag{7.10}$$

and $f_m = \frac{v}{\lambda}$ is the maximum Doppler frequency.

Section 4.7.1 in the Rappaport book gives a thorough analysis of Clarke's model for flat fading and Gans' corresponding spectral analysis work. It also details the simulation method first presented by Smith [34], which can also be used here to generate a fading waveform valid in both the time and frequency domains. Basically, Smith's method inputs a randomly generated Gaussian noise source into the filter defined by $\sqrt{S(f)}$. The output of the filter in the time domain is a valid fading waveform. This process is illustrated in Fig. (7.3 [20].

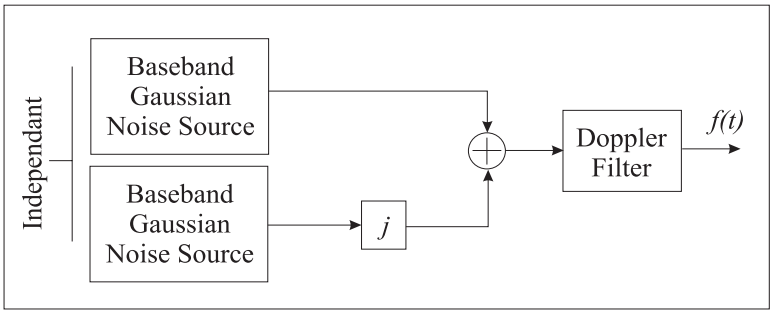

Figure 7.3: The block diagram of a fading waveform generator for computer simulation for the uniform sector model

7.2.3 Rician Model

In this model, multipath power arrives from all directions. In one direction, however, a strong multipath component exists. Thus this situation, mathematically, is the sum of the uniform sector model with $\alpha = 2\pi$ and total uniform power P_u with an additional multipath arriving from θ_o with power P, given by

$$p(\theta) = \frac{P_u}{2\pi} + P\delta(\theta - \theta_o) \tag{7.11}$$

The Fourier coefficients are

$$|F_0| = P + P_u \qquad\qquad |F_1| = P \tag{7.12}$$

Thus the angular spread simplifies to

$$\Lambda = \sqrt{1 - \frac{P^2}{(P + P_u)^2}} \tag{7.13}$$

Given the total arriving power, $P_T = P + P_u$ and the measured Λ, you can calculate P and P_u for this model by

$$P = P_T\sqrt{1 - \Lambda^2} \qquad\qquad P_u = P_T - P \tag{7.14}$$

To generate the fading waveform for this model, first generate a fading waveform for the uniform sector model with $\alpha = 2\pi$ and total uniform power P_u. Then add to it a fading waveform for the additional discrete multipath arriving from θ_o with power P. This additional multipath will result in a signal $\sqrt{P}e^{j\vec{k}\cdot\vec{x}(t)}$. The sum of these two signals is the Rician fading waveform. This process is shown in Fig. (7.4).

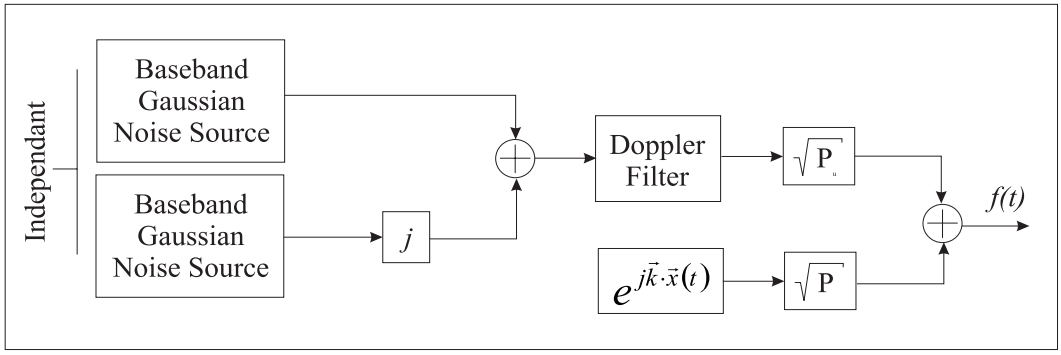

Figure 7.4: The block diagram of a fading waveform generator for computer simulation of the Rician model

7.3 Implementation Details

The simulation of the channel model is implemented in Matlab in a preprocessor, a simulator, and a postprocessor. The simulator and the postprocessor call additional functions in a three-level functional organization. This is shown in the flow diagram in Fig. (7.5).

The preprocessor simply sets the two variables of the simulation, the link number and the AOA model. These are both inputs into the simulator. It outputs the complex impulse response of the channel at each position along the track. The postprocessor calculates and plots the wideband power delay profile as a function of time delay and position along the track. This results in a 3D

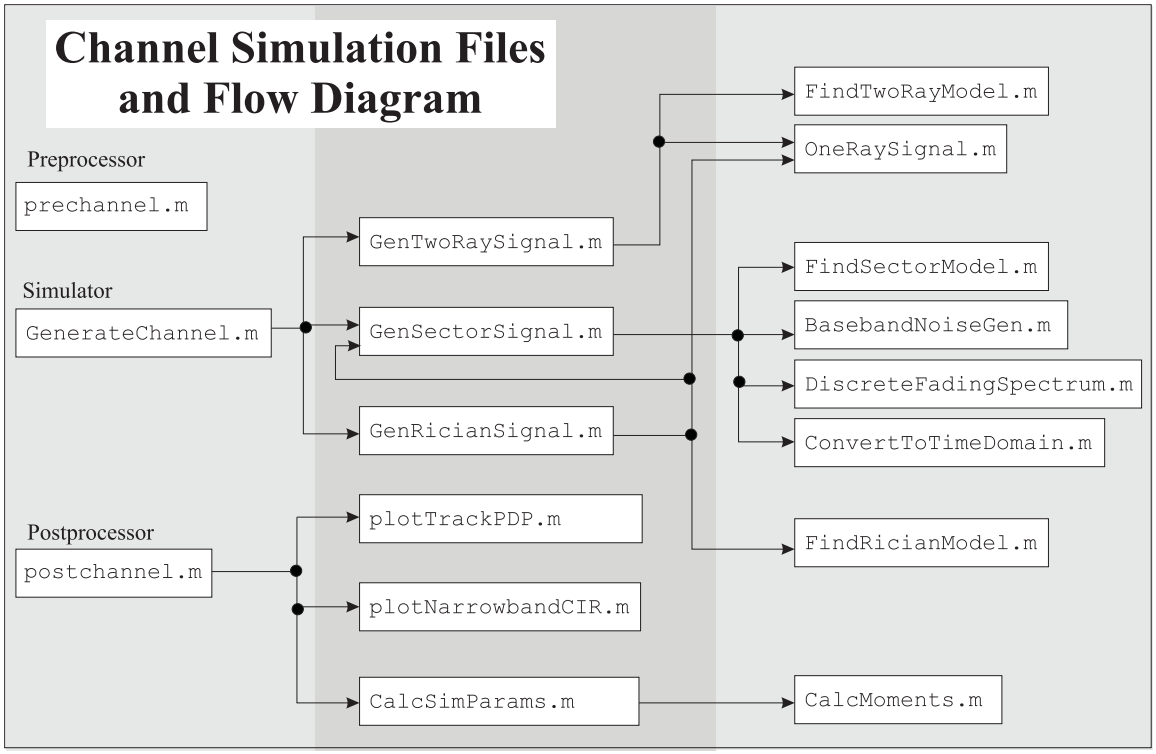

Figure 7.5: The Matlab files used in the channel model simulation and their dependencies.

plot as shown in Fig. (7.6). Note that only 5λ are plotted here so that the detail can be seen better.

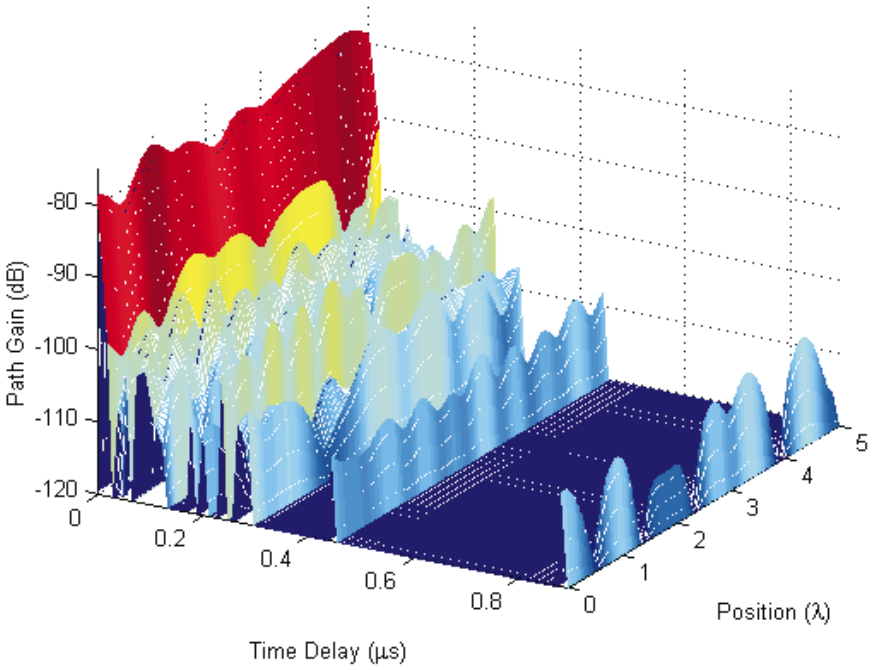

Figure 7.6: The simulated power delay profile as a function of position at link 22.

It also calculates the narrowband channel response along the track, calculated simply by summing all of the values in the complex channel impulse response at each individual position. The phase of this narrowband signal is also plotted. Example narrowband outputs from each AOA model are shown in Fig. (7.7). It is apparent that each AOA model results in a different narrowband fading waveform.

7.3.1 Use in a Communication System Simulation

The generated complex impulse response of the channel at any given position is an FIR filter with complex taps at the peak time delays of the link. This is very wideband, since the peak time delays are separated by a minimum of 4 ns. This is a result of the sampling rate of the oscilloscope on which the PDP was displayed, not a result of the bandwidth of the measurement system. As

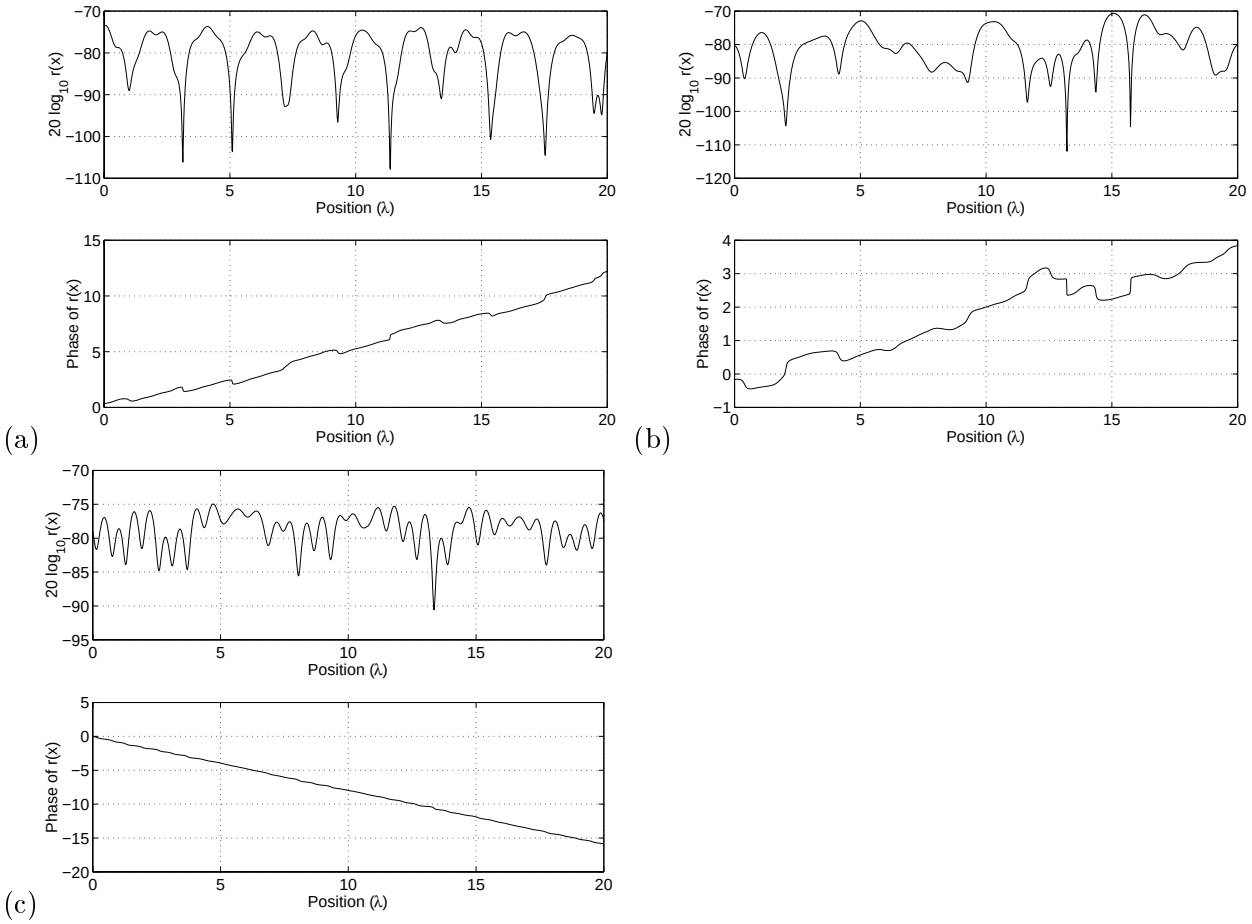

Figure 7.7: The simulated narrowband channel response as a function of position at link 22 for the (a) Two Ray, (b) Uniform Sector, and (c) Rician AOA Models.

discussed in Section 2.1.2, the RF bandwidth of the measurements was 200 MHz, which led to an unambiguous multipath component resolution of 20 ns. For use in the design of a particular communications system, the generated channel impulse response should be bandlimited by passing it through a low-pass filter with the characteristic of the receiver IF filter.

7.4 Verification of the Simulation

7.4.1 Signal Verification

One of the claims that this report has made is that the signals generated from any of the AOA models in Section 7.2 will produce the correct fading rate variance. This is proven be the following experiment. For each possible Λ, generate two signals along orthogonal tracks. Calculate the fading rate variance for this signal from Eq. (4.2). Determine the measured angular spread from Eq. (4.3) and compare it to the original Λ. They should be equal, regardless of the AOA model employed. This test has been run for all of the AOA models across a range of Λ. The test results are plotted in Fig. (7.8).

The Uniform Sector and Rician AOA models are less precise than the Two Ray model. However, from these plots and many repetitions of these tests, the implementation seems to be unbiased. You can also see that the histograms of each of the models resembles the expected histogram from the three plotted in Fig. (7.8). Although these PDFs are not derived in this report, they are shown well in the plotted histograms.

7.4.2 Channel Impulse Response Verification

Another claim that this report has made is that the wideband and large-scale path loss characteristics of the measured channels are preserved. Since the path loss of each multipath should be the same as the measurements and the time delays are constant, this measurement-based model should also accurately reproduce the mean delay and RMS delay spread of the measurements. To test this claim, a simulation test was run that created a 20λ track of complex channel impulse responses (CCIRs). The spatial average PDP is calculated from the mean square value of the CCIRs on the track. The path loss PL, mean delay $\bar{\tau}$, and RMS delay spread are calculated from the spatial

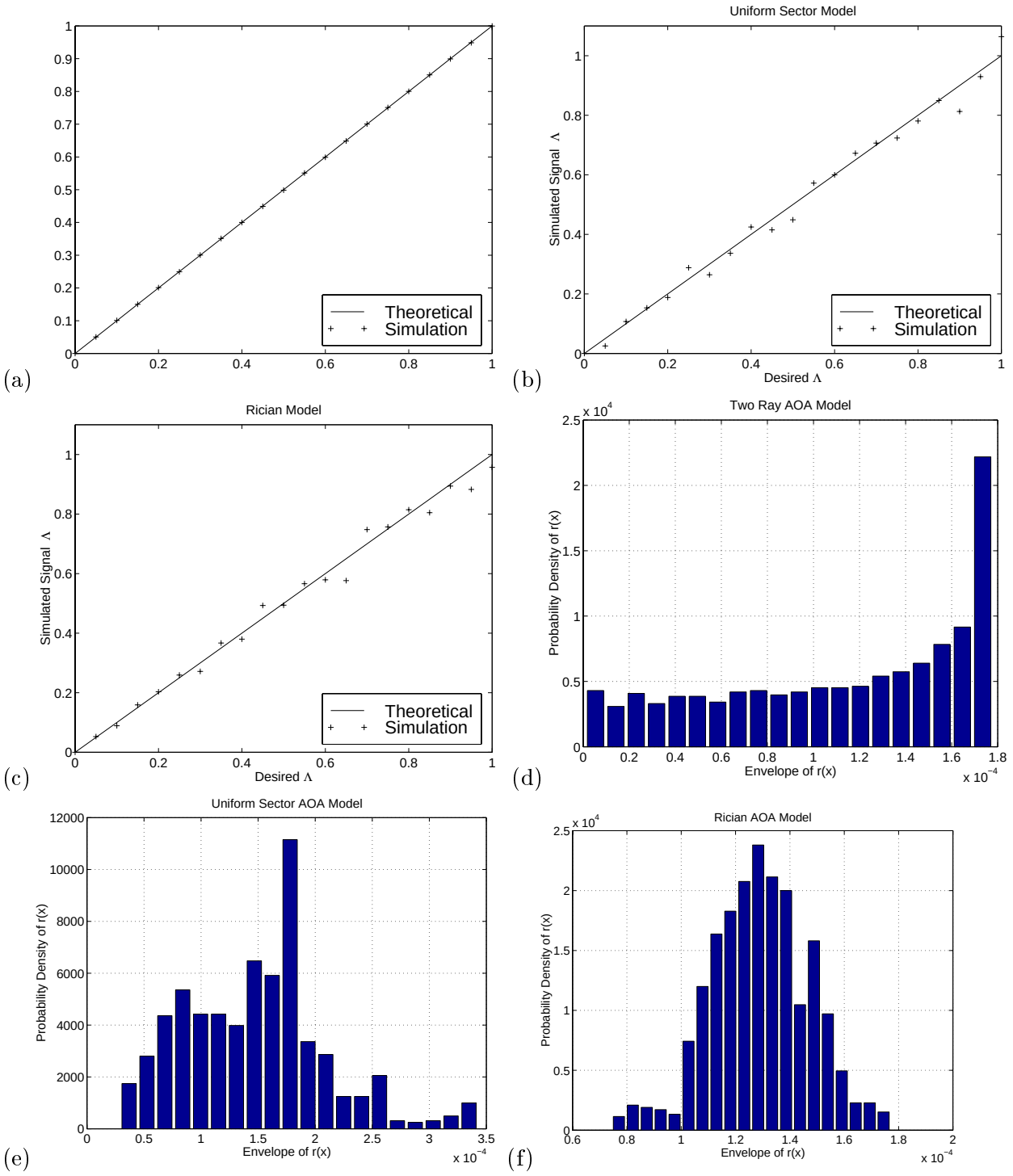

Figure 7.8: The measured Λ of a simulated signal vs. the intended Λ for the (a) Two Ray, (b) Uniform Sector, and (c) Rician models. The histogram of envelope of the fading waveform is shown for the (d) Two Ray, (e) Uniform Sector, and (f) Rician models.

average PDP. This test is done for each of the 22 different links, and the test results can be compared with the measurement results in Table 7.1. Just the results for channels generated with the Uniform Sector Model are shown, however, all three AOA models were tested and showed similar agreement with measured data.

7.5 Model Limitations and Assumptions

A major assumption of this model is that each multipath peak fades independently of the other peaks in the PDP. A corollary to this assumption is that the angular distribution of the multipath that contribute to one multipath peak in a PDP is independent from the angular distribution of multipath contributing to another. In general, this assumption is rather shaky unless it is shown by angle-of-arrival measurements. Since these measurements have not been done, this model can only claim to be a first-cut model or a proof-of-concept. Future measurements will either verify this model or lead to proper modeling of dependencies between the multipath peaks at different time delays.

Because this model is strictly measurement-based, further measurements are required to adapt the model for different carrier frequencies, antenna heights, or environment types. Since measured channel data is always important for the development of new types of communications systems, this requirement just states an already intuitive rule. Also, the measurement process will be simplified by the automated measurement track recently constructed at MPRG.

7.6 Conclusion

This report has introduced a new measurement-based channel model for wideband mobile radio channels. The simulation of the model has been implemented in Matlab and the claims of the model have been verified. The model is very good at accurately simulating the fading rate variance of a wideband channel. It produces an angle-of-arrival characteristic that is used to model the Doppler seen at the mobile receiver. Although the channel impulse response output from the model is wideband, it can be filtered to any bandwidth below 200 MHz.

Accurate wideband channel models are essential for a wide variety of mobile radio communication system design. This model is limited both by the extent of the measurements on which it is based and the fact that more measurements need to be done to verify some of its assumptions. However, this chapter has shown that accurate fading characteristics can be be recreated by a measurement-

Table 7.1: Tablular Comparison of Measurement Results with Simulation

Link Descriptive Information					Measured PDP Data			Uniform Sector AOA Model Results		
Loc. #	Site Name	Env. Type	Obs. Type	d (m)	$\bar{\tau}$ (ns)	σ_τ (ns)	PL (dB)	$\bar{\tau}$ (ns)	σ_τ (ns)	PL (dB)
(1)	Old Turner St.	Urban OBS	Automobiles	39.5	15.7	51.3	78.8	15.3	50.0	78.3
(2)	Old Turner St.	Urban LOS	-	175.3	4.5	47.9	75.7	5.6	48.4	77.0
(3)	Old Turner St.	Urban LOS	-	248.5	3.7	29.7	89.3	4.7	35.1	89.9
(4)	Old Turner St.	Urban OBS	Terrain	396.1	76.1	189.3	112.6	88.9	201.5	113.4
(5)	Southgate Dr.	Rural LOS	-	100.6	2.9	22.7	85.2	4.2	28.1	87.1
(6)	Southgate Dr.	Rural LOS	-	211.0	15.0	67.6	98.3	33.5	95.9	101.9
(7)	Southgate Dr.	Rural OBS	Trees	157.0	5.4	27.5	92.8	4.6	25.6	91.9
(8)	Beef Cattle Farm	Rural OBS	Terrain	332.3	188.3	333.7	106.9	215.3	348.5	107.5
(9)	Beef Cattle Farm	Rural LOS	-	393.7	5.0	41.1	96.3	3.6	32.8	95.4
(10)	Beef Cattle Farm	Rural OBS	Trees	453.6	87.2	247.2	112.3	88.3	254.8	111.2
(11)	Forest	Rural OBS	Trees	48.8	25.3	58.3	89.7	25.3	58.3	89.5
(12)	Forest	Rural OBS	Trees, Terrain	151.1	110.1	91.2	119.3	110.1	91.2	119.2
(13)	Hutcheson Hall	Urban OBS	Terrain	127.3	91.7	192.5	100.5	91.7	192.5	100.6
(14)	Hutcheson Hall	Urban LOS	-	50.0	13.7	33.9	76.1	13.7	33.9	78.9
(15)	Hutcheson Hall	Urban OBS	Bridge	145.5	5.5	33.8	95.0	5.5	33.8	93.7
(16)	Golf Course, Cage	Rural OBS	Trees	1293.9	73.9	150.9	124.2	73.9	150.9	125.7
(17)	Golf Course, Cage	Rural OBS	Trees	1135.8	102.8	267.4	125.1	102.8	267.4	124.9
(18)	Derring Hall	Urban OBS	Buildings	194.6	41.8	113.2	107.5	41.8	113.2	106.9
(19)	Derring Hall	Urban OBS	Buildings	254.8	20.2	74.8	115.8	20.2	74.8	115.5
(20)	Drillfield	Urban LOS	-	307.8	11.6	74.5	90.5	11.6	74.5	88.8
(21)	Drillfield	Urban LOS	-	556.7	26.8	88.2	106.1	26.8	88.2	107.3
(22)	Drillfield	Urban LOS	-	103.4	4.6	35.4	77.8	4.6	35.4	78.7

based wideband mobile radio channel model. Such a model will become more and more important as communications systems employ wider RF bandwidths, adaptive equalizers, rake receivers, and smart antennas.

Chapter 8

Contributions

Initially, this measurement campaign was laid out to serve two purposes. First, it was required to provide measured peer-to-peer channel data and simulation methods to ITT to serve in the development of the HMT. Second, the measurements were important to Virginia Tech as a first test of the ability to measure angular spread using track PDP measurements. Both have been accomplished and discussed in this thesis report.

The simulation of the HMT has proceeded in two ways using the measured data. The measurement of PDPs was described in detail in Chapter 2 and the results were reported in Chapter 6. Measured PDPs have been used by ITT to simulate the operation of the HMT in static channels. The measurement-based channel model presented in Chapter 7 is not yet in use by ITT, but it gives them the ability to simulate the HMT in a mobile environment.

Before these measurements of angular spread, only analytical means like those presented in Chapter 3 were available to predict the angular spread. In this thesis, measured profiles are reported. As discussed in Chapter 6, the data show that transient error has an effect on the measurements. However, the results are not dominated by error, and the behavior of angular spread can be seen.

The angular spread measurements extensively described in this thesis have more than an academic interest. The results show insight into the design of rake receivers. Use of the angular spread data also results in an accurate measurement-based channel model presented for use in the simulation of the peer-to-peer channel.

Future track PDP measurements will benefit from the analysis in Chapter 4. The analysis provides a method for calculating an unbiased estimate of the angular spread in a given local area. Future

work will also be able to use measured angle-of-arrival data taken with MPRG's new motorized antenna positioning system to independently and more completely verify the measured angular spread.

These measurements of AOA and angular spread will also benefit the verification of site-specific ray-tracing models that predict the spatial and temporal channel impulse response given a 3D environmental database [17].

If it is shown by future measurement campaigns that the track power measurement technique can accurately estimate the angular spread at the receiver, its advantage over other AOA measurement techniques is clear. Since measurement of phase is not necessary, the receiver design is simple. The technique applies to both wideband and narrowband measurements. In the simplest case, the narrowband angular spread can be measured with just a CW transmitter and an envelope detector receiver.

This thesis has extensively explored the track measurement technique for wideband (PDP) measurements. It has allowed low-complexity simultaneous evaluation of the time and the angle dispersion characteristics of the peer-to-peer channel. The measurement setup, data collection, analysis and modeling have all been reported in this thesis.

Bibliography

[1] G.L. Turin, F.D. Clapp, T.L. Johnston, S.B. Fine, and D. Lavry, "A Statistical Model of Urban Multipath Propagation," *IEEE Transactions on Vehicular Technology*, vol. VT-21, no. 1, pp. 1–9, Feb 1972.

[2] J. Fuhl, J.P. Rossi, and E. Bonek, "High-Resolution 3-D Direction-of-Arrival Determination for Urban Mobile Radio," *IEEE Transactions on Antennas and Propagation*, vol. 45, no. 4, pp. 672–682, April 1997.

[3] D.M.J. Devasirvatham, "A Comparison of Time Delay Spread and Signal Level Measurements Within Two Dissimilar Office Buildings," *IEEE Transactions on Antennas and Propagation*, vol. AP-35, no. 3, March 1987.

[4] M.J. Feuerstein, K.L. Blackard, T.S. Rappaport, S.Y. Seidel, and H.H. Xia, "Path Loss, Delay Spread, and Outage Models as Functions of Antenna Height for Microcellular System Design," *IEEE Transactions on Antennas and Propagation*, vol. 43, no. 3, pp. 487–498, Aug 1994.

[5] G.D. Durgin and T.S. Rappaport, "A Basic Relationship Between Multipath Angular Spread and Narrowband Fading in a Wireless Channel," *IEE Electronics Letters*, vol. 34, no. 25, pp. 2431–2432, 10 Dec 1998.

[6] G.D. Durgin and T.S. Rappaport, "A New Fundamental Relationship Between Small-Scale Fading and Multipath Angle-of-Arrival," *accepted for presentation in 49th IEEE Vehicular Technology Conference*, 1999.

[7] H.H. Xia, H.L. Bertoni, L.R. Maciel, A. Lindsay-Stewart, and R. Rowe, "Microcellular Propagation Characteristics for Personal Communications in Urban and Suburban Environments," *IEEE Transactions on Vehicular Technology*, vol. 43, no. 3, Aug 1994.

[8] N. Papadakis, A.G. Kanatas, and P. Constantinou, "Microcellular Propagation Measurements and Simulation at 1.8 GHz in Urban Radio Environment," *IEEE Transactions on Vehicular Technology*, vol. 47, no. 3, Aug 1998.

[9] L. Piazzi, G. Liang, H.L. Bertoni, and S. Kim, "Comparison of Measurement Based and Site Specific Ray Based Microcellular Path Loss Predictions," in *IEEE ICUPC '96, Boston, MA*, October 1996, vol. 2, pp. 656–660.

[10] P. Harley, "Short Distance Attenuation Measurements at 900 MHz and 1.8 GHz Using Low Antenna Heights for Microcells," *IEEE Journal on Selected Areas in Communications*, vol. SAC-7, no. 1, Jan 1989.

[11] A.M.D. Turkmani, J.D. Parsons, Feng Ju, and D.G. Lewis, "Microcellular Radio Measurements at 900, 1500, and 1800 MHz," in *IEE 5th International Conference on Mobile Radio and Personal Communications*, Warwick UK, Dec 1989, pp. 65–68.

[12] S.Y. Seidel, T.S. Rappaport, and R. Singh, "Path Loss, Scattering, and Multipath Delay Statistics in Four European Cities for Digital Cellular and Microcellular Radiotelephone," *IEEE Transactions on Vehicular Technology*, vol. 40, no. 4, pp. 721–730, Nov 1991.

[13] K. Siwiak, *Radio Wave Propagation and Antennas for Personal Communications*, Artech House Publishers, New York, 1995.

[14] J.B. Andersen O. Nørklit, "Diffuse Channel Model and Experimental Results for Array Antennas in Mobile Environments," *IEEE Transactions on Antennas and Propagation*, vol. 46, no. 6, pp. 834–840, June 1998.

[15] J.P. Rossi, J.P. Barbot, and A.J. Levy, "Theory and Measurement of the Angle of Arrival and Time Delay of UHF Radiowaves Using a Ring Array," *IEEE Transactions on Antennas and Propagation*, vol. 45, no. 5, pp. 876–884, May 1997.

[16] W.G. Newhall, T.S. Rappaport, and D.G. Sweeney, "A Spread Spectrum Sliding Correlator System for Propagation Measurements," *RF Design*, pp. 40–54, April 1996.

[17] G.D. Durgin, N. Patwari, and T.S. Rappaport, "An Advanced 3D Ray Launching Method for Wireless Propagation Prediction," in *IEEE 47th Vehicular Technology Conference*, Phoenix AZ, May 1997, vol. 2, pp. 785–789.

[18] S.Y. Seidel and T.S. Rappaport, "Site-Specific Propagation Prediction for Wireless In-Building Personal Communication System Design," *IEEE Transactions on Vehicular Technology*, vol. 43, no. 4, pp. 879–891, Nov 1994.

[19] D.C. Cox, "Delay Doppler Characteristics of Multipath Propagation at 910 MHz in a Suburban Mobile Radio Environment," *IEEE Transactions on Antennas and Propagation*, vol. AP-20, no. 5, pp. 625–635, Sep 1972.

[20] T.S. Rappaport, *Wireless Communications: Principles and Practice*, Prentice-Hall Inc., New Jersey, 1996.

[21] W.G. Newhall, K. Saldanha, and T.S. Rappaport, "Using RF Channel Sounding Measurements to Determine Delay Spread and Path Loss," *RF Design*, pp. 82–88, Jan 1996.

[22] H. Hashemi, "The Indoor Radio Propagation Channel," *Proceedings of the IEEE*, vol. 81, no. 7, pp. 943–968, July 1993.

[23] R.B. Ertel, P. Cardieri, K.W. Sowerby, T.S. Rappaport, and J.H. Reed, "Evolution and Applicability of Spatial Channel Models for Wireless Communications," *IEEE Personal Communcations Magazine*, vol. 5, no. 1, pp. 10–12, Feb 1998.

[24] J.C. Liberti and T.S. Rappaport, "A Geometrically Based Model for Line-of-sight Multipath Radio Channels," in *IEEE 46th Vehicular Technology Conference*, Atlanta GA, April 1996, pp. 844–848.

[25] R.H. Clarke, "A Statistical Theory of Mobile-Radio Reception," *Bell System Technical Journal*, vol. 47, pp. 957–1000, 1968.

[26] I.S. Gradshteyn and I.W. Ryzhik, *Table of Integrals, Series, and Products*, Academic, New York, 5th edition, 1994.

[27] H. Hashemi, "Simulation of the Urban Radio Propagation Channel," *IEEE Transactions on Vehicular Technology*, vol. VT-28, no. 3, Aug 1979.

[28] A.A.M. Saleh and R.A. Valenzuela, "A Statistical Model for Indoor Multipath Propagation," *IEEE Journal on Sel. Areas in Comm.*, vol. SAC-5, no. 2, Feb 1987.

[29] K. Saldanha and J.H. Reed, "Performance Evaluation of DECT in Different Radio Environments," Tech. Rep. MPRG-TR-96-28 (163 pages), Virginia Tech, http://scholar.lib.vt.edu/theses/index.html, Aug 1996.

[30] J. C-I Chuang, "The Effects of Multipath Delay Spread on Timing Recovery," in *Proceedings of IEEE ICC'86*, Toronto, Canada, June 1986, pp. 55–59.

[31] D.M.J. Devasirvatham, "Multipath Time Delay Jitter Measured at 850 MHz in the Portable Radio Environment," *IEEE Journal on Selected Areas in Communications*, vol. SAC-5, no. 5, June 1987.

[32] T.S. Rappaport, *Simulation of Indoor Radio Channel Impulse Response Models: SMRCIM*, Users Manual, April 1998.

[33] M.J. Gans, "A Power-Spectral Theory of Propagation in the Mobile Radio Environment," *IEEE Transactions on Vehicular Technology*, vol. VT-21, no. 1, pp. 27–38, Feb 1972.

[34] J.I. Smith, "A Computer Generated Multipath Fading Simulation for Mobile Radio," *IEEE Transactions on Vehicular Technology*, vol. VT-24, no. 3, pp. 39–40, Aug 1975.

Appendix A

Site Maps and Pictures

The electronic copy of this appendix is in the file, AppendixA.pdf.

Vita

Neal Patwari was born in Cleveland, Ohio on February 28, 1975 to Ken and Arti Patwari. Neal graduated from Mayfield Senior High School in Mayfield Village, Ohio. Since 1993, he has been a student at Virginia Polytechnic Institute and State University, in Blacksburg, Virginia, earning a B.S. degree in May 1997 and an M.S. degree in May 1999, both in Electrical Engineering. As an undergraduate, he was a Bradley Scholar in the Bradley Department of Electrical and Computer Engineering. Comsat Labs, in Clarksburg, Maryland was the site of a co-operative education experience for Neal. Later, he interned at the Oak Ridge National Labs in Oak Ridge, TN. Neal enjoys playing his baritone in the marching band, basketball pep band, and symphony band, and enjoys a variety of outdoor recreation, especially skiing, mountain biking, and hiking. Neal has one older brother, Parth Patwari, currently living in Boston. Neal will be joining Motorola in Plantation, Florida, after graduation.